

https://doi.org/10.1093/petrology/egac075
Original Manuscript

The Shallow Magmatic Plumbing System of the Deccan Traps, Evidence from Plagioclase Megacrysts and Their Host Lavas

Andrea Marzoli¹, Paul R. Renne^{2,3}, Rasmus Andreasen⁴, Richard Spiess⁵, Massimo Chiaradia⁶, Dawn C. S. Ruth⁷, Andrew J. Tholt^{2,3}, Kanchan Pande⁸ and Fidel Costa⁹

- ¹Dipartimento Territorio e Sistemi Agro-Forestali, Università di Padova, via dell'Università 16, 35020-Legnaro, Italy
- ² Berkeley Geochronology Center, 2455 Ridge Road Berkeley, CA 94709, USA
- ³Department of Earth and Planetary Science, University of California at Berkeley, Berkeley, CA 94720-476, USA
- ⁴ Geosciences Department, Høegh-Guldbergsgade 2, Aarhus, DK-8000, Denmark
- ⁵Geosciences Department, Università di Padova, via G. Gradenigo 6, 35100-Padova, Italy
- ⁶Department of Earth Sciences, Université de Gèneve, Rue des Maraîchers 13 CH-1205 Geneva, Switzerland
- ⁷ U.S. Geological Survey Volcano Science Center, 345 Middlefield Road, MS 910, Menlo Park, CA 94025, USA
- ⁸Department of Earth Sciences, Indian Institute of Technology, Bombay Powai, Mumbai 400076, India
- ⁹Institut de Physique du Globe de Paris, Universite de Paris Cité, 1 rue Jussieu, 75238 Paris, France

Abstract

We investigate the shallow plumbing system of the Deccan Traps Large Igneous Province using rock and mineral data from Giant Plagioclase Basalt (GPB) lava flows from around the entire province, but with a focus on the Saurashtra Peninsula, the Malwa Plateau, and the base and top of the Western Ghats (WG) lava pile. GPB lavas in the WG typically occur at the transition between chemically distinct basalt formations. Most GPB samples are evolved basalts, with high Fe and Ti contents, and show major and trace elements and Sr-Nd-Pb isotopic compositions generally similar to those of previously studied Deccan basalts. Major element modeling suggests that high-Fe, evolved melts typical of GPB basalts may derive from less evolved Deccan basalts by low-pressure fractional crystallization in a generally dry magmatic plumbing system. The basalts are strongly porphyritic, with 6-25% of mm- to cm-sized plagioclase megacrysts, frequently occurring as crystal clots, plus relatively rare olivine and clinopyroxene. The plagioclase crystals are mostly labradoritic, but some show bytownitic cores (general range of anorthite mol%: 78-55). A common feature is a strong Fe enrichment at the plagioclase rims, indicating interaction with an Fe-rich melt similar to that represented by the matrix compositions (FeOt up to 16-17 wt%). Plagioclase minor and trace elements and Sr isotopic compositions analyzed by laser ablation inductively coupled plasma mass spectrometry show evidence of a hybrid and magma mixing origin. In particular, several plagioclase crystals show variable 87Sr/86Sr₁, which only partially overlaps with the ${}^{87}Sr/{}^{86}Sr_1$ of the surrounding matrix. Diffusion modeling suggests residence times of decades to centuries for most plagioclase megacrysts. Notably, some plagioclase crystal clots show textural evidence of deformation as recorded by electron back-scatter diffraction analyses and chemical maps, which suggest that the plagioclase megacrysts were deformed in a crystal-rich environment in the presence of melt. We interpret the plagioclase megacrysts as remnants of a crystal mush originally formed in the shallow plumbing system of the Deccan basalts. In this environment, plagioclase acquired a zoned composition due to the arrival of chemically distinct basaltic magmas. Prior to eruption, a rapidly rising but dense Fe-rich magma was capable of disrupting the shallow level crystal mush, remobilizing part of it and carrying a cargo of buoyant plagioclase megacrysts. Our findings suggest that basaltic magmas from the Deccan Traps, and possibly from LIPs in general, are produced within complex transcrustal magmatic plumbing systems with widespread crystal mushes developed in the shallow crust.

Keywords: crystal mush, magma differentiation, plagioclase megacrysts, Deccan Traps, Large Igneous Province

INTRODUCTION

Studies of Large Igneous Provinces (LIPs) have historically focused on identifying mantle sources and melting mechanisms, on the role of assimilated crustal components involved in the genesis of the basaltic magmas and, recently, on the link of LIPs with global climate change events (e.g. Bond & Grasby, 2017; Ernst & Youbi, 2017; Clapham & Renne, 2019). In contrast, with some exceptions (e.g. Cox, 1980; Marsh, 2004; Karlstrom & Richards, 2011; Black & Manga, 2017; Krans et al., 2018; Moore et al., 2018; Ernst et al., 2019; Mittal et al., 2021; Black et al., 2021), relatively little attention has been given to the plumbing system of LIP magmas, i.e. the

architecture and evolution of the magmatic system from the MOHO (crust-mantle boundary) to the shallow crust. The relative scarcity of studies focusing on the transcrustal magma system of LIPs is partially due to the geochemical characteristics of LIP magmas. These are dominated by moderately evolved basalts typically having 8–4 wt% MgO, whereas primary or near-primary mantle melt compositions (MgO > 10 wt%) as well as strongly evolved andesitic to rhyolitic products are rare (Cox & Hawkesworth, 1985; Melluso et al., 2006; Sheth et al., 2013; Marzoli et al., 2019). Thus, the relatively uniform compositions of LIP magmas combined with their generally simple mineralogy dominated by plagioclase and

^{*}Corresponding author. E-mail: andrea.marzoli@unipd.it

augitic pyroxene hinder recognition of differentiation processes acting in the magma plumbing system of LIPs.

LIP magmas are relatively homogeneous in composition and were erupted at rates as high as 50-250 km³/year in pulses lasting years to centuries (Black et al., 2021; Self et al., 2022). This may suggest that LIP magmas differentiated in large reservoirs that controlled and buffered the composition of the erupted magmas (Ernst et al., 2019). In this sense, LIP magmas seem to be significantly different from those of ocean islands or arcs, where the eruption rates are usually relatively low, and the magmatic plumbing system is complex and frequently long-lived (Cashman et al., 2017; Sparks et al., 2019). Moreover, in subductionzone settings, magmas rise, stall, and differentiate across the entire crustal depth, from the MOHO to the shallow crust in a transcrustal magma plumbing system (Cashman et al., 2017). In magmatic plumbing systems, volatile species (CO2 in particular) possibly exsolve from the magma upon decompression and then rise into the shallow crust, where they flux and remobilize stagnant crystalline mushes triggering eruptions (Cashman et al., 2017; Caricchi et al., 2018; Giordano & Caricchi, 2022). Even though it is still unclear to what degree the plumbing system of LIP magmas resembles those of arc magmas, there is growing evidence that LIP basaltic magmas can be quite rich in volatiles (Self et al., 2008; Edmonds, 2008; Callegaro et al., 2014; Capriolo et al., 2020; Hernandez Nava et al., 2021; Boscaini et al., 2022), which may have triggered the eruptions of the basalts.

The goal of this study is to investigate the shallow plumbing system of the Deccan Traps LIP in India (Fig. 1a). The Deccan LIP was actively erupting across the Cretaceous-Paleogene boundary (Renne et al., 2015; Schoene et al., 2015, 2019; Sprain et al., 2019) and is presently represented by widespread and thick lava flow fields in central and western India and in the Seychelles (Cox & Hawkesworth, 1985; Beane et al., 1986; Mahoney, 1988; Melluso et al., 1995; Kale et al., 2020; Self et al., 2021), as well as a yet unknown extent of lavas in the Arabian Sea (Mittal et al., 2022, and references therein). Deccan lavas are mainly tholeiitic basalts with volumetrically minor alkaline or silicic lavas and were possibly produced by a mantle plume system during the northward migration of the Indian Plate (e.g. Glišović & Forte, 2017; but see also Sheth, 2005).

The Deccan LIP is characterized by plagioclase-megacrystic lavas, which have been noted in the Deccan Traps for decades (e.g. Karmarkar et al., 1971; Hooper et al., 1988) and are sufficiently abundant that the term Giant Plagioclase Basalts (GPBs; or Giant Phenocryst Basalts) has been coined and is in common usage today. The definition of a GPB varies between workers but generally centers on phenocryst size, which typically is 2 cm or greater. We find that size-based definitions are somewhat arbitrary, as many GPB flow fields or lobes have highly heterogeneous plagioclase megacryst dimensions and abundances that can vary on the scale of a few cm (Fig. 2a,b; e.g. Hooper et al., 1988; Higgins & Chandrasekharam, 2007; Shandilya et al., 2021). In fact, plagioclase megacrysts may be abundant (30-50% in volume) and very large (>2 cm) in only restricted flow lobes from pahoehoe lava flow fields. Other lobes from the same lava flow field may contain fewer (5-20 vol%) and smaller plagioclase crystals (0.5-2 cm). One of the puzzling aspects of the Deccan GPBs is that despite their megacryst load, they appear to be very widespread to the extent that they are used as stratigraphic markers delineating contacts between different geochemically defined formations (e.g. Beane et al., 1986; Hooper et al., 1988; Kale et al., 2020; Shandilya et al., 2021). An extreme case is the Rajgad GPB flow field, which is exposed over an area greater than 30000 km² (Shandilya et al., 2021), always at or near the base of the Mahabeleshwar Fm. Given that the concentration of megacrysts locally exceeds 50 vol% in many GPB flow lobes, their effective viscosity should have hindered eruptibility and apparent capacity to flow overland for large distances (e.g. Marsh, 1981).

Although their origin is still debated (Sen et al., 2006; Higgins & Chandrasekharam, 2007; Borges et al., 2014; Sheth, 2016; Krishnamurthy, 2020), there is general agreement that the plagioclase megacrysts recorded a relatively long period of evolution of the basaltic magma plumbing system. Despite their potential importance for the understanding of the differentiation processes of Deccan basalts, so far relatively few data have been published for the plagioclase megacrysts, i.e. their major element composition (e.g. Hooper et al., 1988) or Sr isotopic ratios (e.g. Borges et al., 2014). Moreover, with a few exceptions (Mahoney et al., 2000; Alexander & Purohit, 2019), studies have been limited to the Western Ghats (WG) section.

For this study, we analyzed the major and trace element concentrations of 23 megacrystic basaltic samples from GPB lavas that span a large geographic (i.e. the WG, Mandla Lobe, Malwa Plateau, and Saurashtra Peninsula; Fig. 1) portion of the Deccan Volcanic Province and cover most of its duration. On a subset of 11 samples, we analyzed the textures, the major and trace element contents and Sr isotopic compositions of plagioclase megacrysts from plagioclase-rich samples as well as major element concentrations in coexisting olivine and clinopyroxene. Combined with the geochemical analyses of their host lavas, our data elucidate the origin of these large plagioclase crystals, of the magma that carried them to the surface, and on the shallow crustal magmatic plumbing system from which they originated over a large area of the Deccan from north (Saurashtra and Malwa) to south (WG).

The Deccan Traps

Deccan volcanism straddled the K-Pg (Cretaceous-Paleogene) boundary, contributed to the forcing of the end-Cretaceous climate through emissions of volcanic gasses (e.g. SO₂ and CO₂), which are quite abundant in at least some Deccan basalts (Self et al., 2008; Callegaro et al., 2014; Hernandez Nava et al., 2021). This LIP was probably related to a mantle plume impinging under the northward moving Indian continental plate. Deccan magmatic rocks are mainly tholeiitic basalts and subordinate basaltic andesites. These rocks display a quite uniform mineralogy, which is similar to most other tholeiitic LIPs, e.g. dominated by moderately Mg-rich clinopyroxenes and moderately Carich plagioclase (Melluso & Sethna, 2011). Silicic and alkaline magmatic rocks are present in the Deccan, in particular in the north and west of the province (e.g. Basu et al., 2020b; Melluso et al., 2021).

Deccan volcanism has been most intensively studied in the WG, where hundreds of successive lava flows formed a lava pile, which is cumulatively more than 3 km thick, referred to as the Deccan Group (e.g. Beane et al., 1986; Kale et al., 2020). The stratigraphic sequence in the WG (Fig. 1b) has been divided into three main lava flow packages: the Kalsubai, Lonavala, and Wai subgroups, from bottom to top. These subgroups have been subdivided into 12 main lava flow formations, each characterized by distinctive geochemical features, as seen in discriminant function diagrams and in Sr-Nd-Pb isotopic space (see Kale et al., 2020, for discussion of the basis, history, and applicability of this nomenclature). The lower subgroups, Kalsubai and Lonavala in particular, show quite enriched incompatible trace element and isotopic compositions pointing to a significant involvement of enriched mantle and crustal components (e.g. Peng et al., 1994;

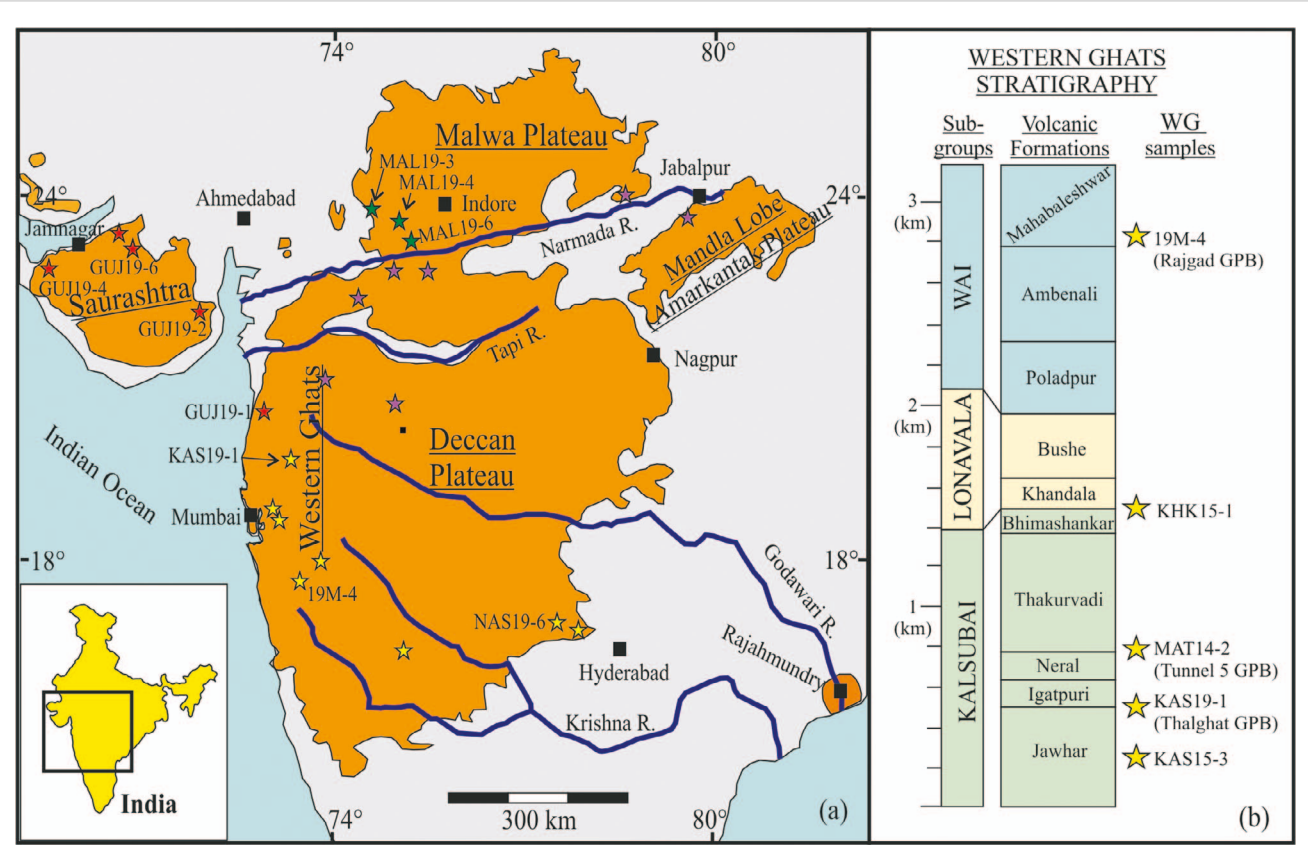


Fig. 1. (a) Schematic map of the Deccan Traps (in orange) Large Igneous Province in India (inset). Stars show sampling locations, the sites of some important samples are labeled. Sampling coordinates are reported in Table 1. (b) Composite stratigraphic section of the WG (modified after Beane et al., 1986; Sprain et al., 2019). Samples from that region are shown by yellow stars.

Basu et al., 2020a). In contrast, the earliest Paleogene Wai subgroup lavas have less enriched compositions and suggest involvement of the shallow upper mantle and possibly of Reunion-like mantleplume components in their genesis. The total duration of WG volcanism is about 0.8 Ma (Renne et al., 2015; Schoene et al., 2015, 2019; Sprain et al., 2019), but each of the volcanic formations was possibly formed by a few short-lived eruption pulses, each lasting a few centuries (Chenet et al., 2008; Self et al., 2022).

The oldest Northern Deccan lavas appear to be older than those from the WG (Basu et al., 1993; Schöbel et al., 2014; Parisio et al., 2016; Eddy et al., 2020; Basu et al., 2020b), as the Indian Plate rapidly migrated northward over the magma sources. The geochemical characteristics of basaltic lavas from the Malwa Plateau and from the Saurashtra Peninsula partially overlap with those from the Lonavala and Wai subgroups of the WG (Melluso et al., 1995; Peng & Mahoney, 1995; Cucciniello et al., 2015, 2019, 2020; Haase et al., 2019). However, in the Malwa Plateau, Wai-type lavas dominate in the lower part of the volcanic pile (Haase et al., 2019). Further details on the geochemical compositions of WG, Malwa Plateau and Saurashtra Peninsula rocks are reported in the Electronic Appendix 1.

METHODS

Mineral major and minor element compositions were analyzed at Milano University (Italy), with a JEOL JXA 8200 Superprobe, and at the U.S. Geological Survey (USGS) in Menlo Park with a JEOL JXA 8530 F+ Hyperprobe. Detailed core-rim traverses on plagioclase (33 crystals), clinopyroxene (17), and olivine (5) crystals were measured at Milano. Other analytical details on electron microprobe (EMP) analyses are reported in the Electronic Appendix 2,

Electron backscatter diffraction (EBSD) analysis was performed on two thin sections at the Department of Geosciences Padova University (Italy) with a CamScan tungsten filament MX2500 scanning electron microscope (SEM) equipped with an Oxford Instruments NordlysNano EBSD detector. The X-ray maps for sample KAS19-1 were collected on a Tescan Solaris Fib-Feg-SEM (Department of Geosciences, University of Padova) equipped with an Ultim® Max 65mm² Silicon Drift Detectors for Energy Dispersive X-Ray spectroscopy (EDS) analysis from Oxford Instruments.

Strontium isotopes and trace elements in plagioclase crystals were analyzed on five samples by laser ablation inductively coupled plasma mass spectrometry (LA-ICP-MS) at the Department of Geosciences at Aarhus University (Denmark). A Resolution Resonetics laser system coupled to first an Agilent 7900 quadropole ICP-MS and then Nu Instruments Plasma Multi-Collector ICP-MS were used to analyze the trace elemental and Sr isotopic composition, respectively, of the same points of the plagioclase crystals, following procedures outlined in Hagen-Peter et al. (2019). For the trace element and Sr isotopic analysis, we used a spot size of 60 and of 154 μ m, respectively.

A total of 23 whole-rock and 11 matrix samples were analyzed for major element and selected trace element concentrations by X-ray fluorescence (XRF) at Washington State University (USA) with a Philips PW2400 spectrometer, following methods described in Johnson et al. (1999). Analytical uncertainties range from 1% to 2% for major elements and from 10 to 15% for trace elements. Trace elements on the same samples were also analyzed by

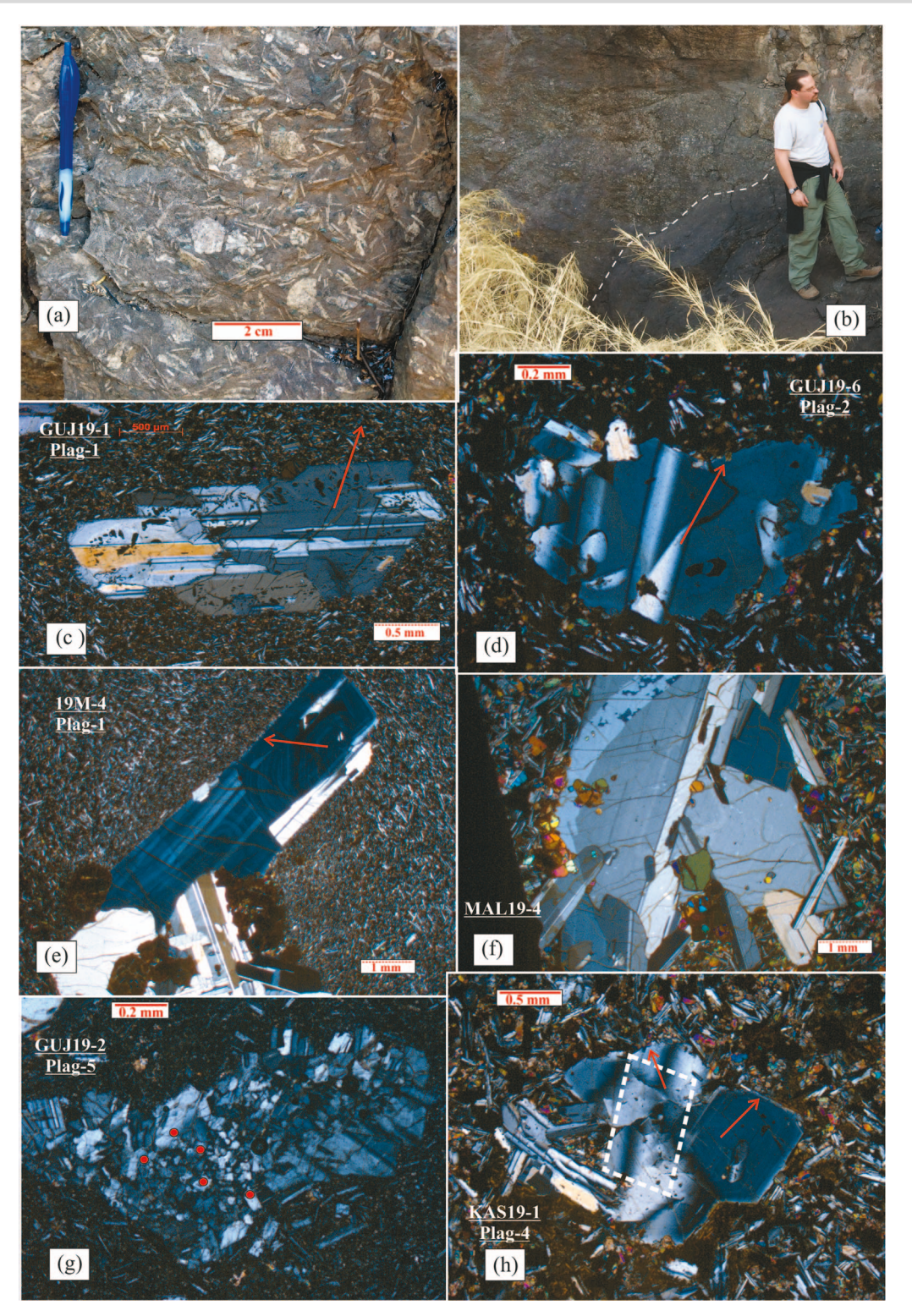


Fig. 2. (a, b) Field pictures of the Thalghat GPB flows, from which we collected KAS19-1; geologist is Loyc Vanderkluysen. (c-h) Thin section cross-polarized images of representative plagioclase crystals from the studied Deccan basalts. Red arrows and dots indicate traverses and spots analyzed by electron microprobe. (c) Partially sieved plagioclase from GUJ19-1 (Plag-1). (d) Possibly deformed small plagioclase aggregate from GUJ19-6 (Plag-2). (e) Large oscillatory zoned plagioclase from 19 M-4. (f) Large plagioclase aggregate from MAL19-4 with olivine inclusions. (g) Strongly fractured, possibly deformed and recrystallized plagioclase clot from GUJ19-2. (h) Deformed plagioclase aggregate from sample KAS19-1 (Plag-4, white rectangle marks area analyzed by EBSD).

ICP-MS at Washington State University (USA) following analytical methods described in Knaack et al. (1994). For ICP-MS analyses, analytical accuracy and precision are estimated at 2–9% and less than 2%, respectively (Knaack et al., 1994).

Sr-Nd-Pb radiogenic isotope ratios on seven matrix and one whole-rock samples (MAT14-2) were measured at the Department of Earth Sciences, University of Geneva (Switzerland) using a Thermo Neptune PLUS Multi-Collector ICP-MS with methods as described in detail in Chiaradia et al. (2011) and Béguelin et al. (2015). Further details for all analytical methods can be found in the Electronic Appendix 1.

RESULTS Sampling

We analyzed 23 samples from northern (Saurashtra Peninsula, Malwa Plateau, Mandla Lobe) to southern Deccan (WG). Details of the samples' contexts, and the role of some samples in previous studies, are discussed in the Electronic Appendix 1; sampling location coordinates are reported in Table 1. Some of the studied rocks were used in previous geochronological studies. The plagioclase megacrysts of GPBs have proven to be exceptionally useful for ⁴⁰Ar/³⁹Ar geochronology because they have generally low Ca/K (<50) and are relatively unzoned compared with phenocrysts in other Deccan lavas. For example, samples KHK15-1, KAS15-3, and MAT14-2 (equivalent to MG7, the Tunnel 5 GPB) are among the most precisely dated samples of Sprain et al. (2019).

GPB lava flow fields, including those studied here, are highly variable in their plagioclase content (c. 20-50% in volume). On the outcrop and in hand specimen, the analyzed rocks generally show a random distribution of plagioclase crystals, which lack a clear preferential orientation. Some workers define giant plagioclase crystals as being at least 2 cm in length (e.g. Seth, 2017) and these are abundant (30-50 vol%) in only restricted flow lobes from pahoehoe lava flow fields. Other lobes from the same lava flow field may contain fewer (5-20 vol%) and smaller plagioclase crystals (0.5–2 cm long). Thus, we consider the 2 cm threshold for definition of GPBs to be arbitrary. Portions of flows containing the largest plagioclase crystals are generally altered, so we focused our sampling and analyses on lobes with smaller, but fresher, plagioclase crystals.

In the comparatively well-studied WG, GPBs tend to occur at the transition between successive geochemically defined lava flow formations, e.g. the Thal Ghat and Tunnel 5 GPBs studied herein occur at the very top of the Jawhar and Neral formations, respectively (e.g. Beane et al., 1986; Hooper et al., 1988). In the WG, GPBs occur at the transition of all formations of the Kalsubai subgroup, but are absent in the Lonavala and rare in the Wai subgroups. In the northern Deccan sub-provinces of the Saurashtra Peninsula, Malwa Plateau, and Mandla Lobe, outcropping lava piles are absent or less well exposed, hindering a precise definition of the stratigraphic position of the studied samples. Sampling sites are shown in Fig. 1. Further details on sampling can be found in the Electronic Appendix 1.

Petrography

The studied rocks are characterized by a fine-grained matrix (except in the samples TM18-3, MAL19-3 and MAL19-4) and by large plagioclase crystals representing 5–20% of the thin section surface area (Figs 2 and 3). The size of the largest plagioclase exceeds 4 mm in all samples and exceeds 1 cm in several samples (e.ge.g., KAS19-1, KAS15-3, MAL19-4, 19M-4, TM18-3, 19P-5, MAT14-2; Figs 2a, b, e, f and 3 f, g). In most samples, small plagioclase crystals (<100 μ m) are rare, while large to very large crystals are dominant (see the thin section scans; Fig. 3 e, f, g). Such features are similar to those described by Higgins & Chandrasekharam (2007), who did a detailed analysis of crystal size distribution of GPBs. Among the samples studied herein, only MAL19-3, GUJ19-2 (Fig. 3h), and GUJ19-3 show a range of plagioclase crystal sizes from small (<100 μ m) to relatively large (c. 5 mm).

Most of the analyzed plagioclase crystals range in size from 0.5 to 10 mm, and in most cases occur in glomerophyric aggregates (crystal clots) of several plagioclase crystals. More generally, single isolated plagioclase crystals (monocrysts) are rare or even absent at the thin section scale of some samples (Fig. 3 e-h). Only a few analyzed plagioclase megacrysts occur as monocrysts and are euhedral, for example Plag-1 in GUJ19-1 (Fig. 2c) and Plag-1 in KAS19-1. In plagioclase clots, many crystal rims in contact with the matrix are euhedral, i.e. in apparent equilibrium with the groundmass. However, a few crystals show rounded shapes (e.g. GUJ19-6 Plag-2, KAS19-1 Plag-4; Fig. 2d, h), while others show embayed rim areas, possibly related to resorption or rapid growth. A frequent feature of the large plagioclase crystals is their oscillatory zoning, which is observed in plagioclase crystals from all samples, but is particularly striking in 19 M-4 (Fig. 2e). Partially resorbed cores are also relatively common, they occur for example in GUJ19-1 (Fig. 3d), GUJ19-2, GUJ19-6, MAL19-4, MAL19-6, and KAS19-1. Partial dissolution, i.e. sieve-textured zones occur in some plagioclase crystals from GUJ19-1 (Fig. 2c), GUJ19-2, and GUJ19-3.

Plagioclase aggregates occasionally show microstructures that may be indicative of deformation. These include high angle grain boundaries at points of impingement, accompanied by subgrain boundaries that propagate from here through the impinging plagioclase crystals, recrystallized growth twins, and deformation twins. Other typical microstructures are undulatory extinction, curved grain boundaries and twin lamellae with sharp triangular tips (e.g. Fig. 2d, h). A relatively large aggregate of plagioclase microcrysts is observed in GUJ19-2 (Fig. 2g). Such fabrics are observed in several samples (e.g. in GUJ19-1, GUJ19-2, GUJ19-6, MAL19-6, KAS-19-1), although only in a few crystals per sample, and are similar to those found in clearly deformed plagioclase crystals from LIPs (cf. Holness et al., 2017, 2022) and subductionrelated basalts (Spiess et al., 2017).

In addition to plagioclase, the only other large crystals (>100 μ m in maximum axis) are rare augitic clinopyroxene and olivine (Figs 2f and 3a, b). These minerals make up less than 4 vol% in all investigated thin sections, and less than 1 vol% in a few samples (e.g. 19 M-4). Olivine is very rare and small (<50 microns) in about half of the studied samples and absent in the other samples. Olivine occurs as phenocrysts surrounded by matrix only in KAS19-1 (Fig. 3b), while it is relatively abundant (1-3 vol%) as an inclusion in plagioclase megacrysts in about half of the samples (e.g. MAL19-3 and MAL19-4; Fig. 2f).

Clinopyroxene crystals are also rare and occur either as inclusions in plagioclase (e.g. in 19P5, MAL19-4, MAL19-6, GUJ19-1, GUJ19-5, KHK15-1, and 19M4), as single crystals (e.g. in 19P5, KAS15-3, GUJ19-6) or in crystal clots (in GUJ19-1, GUJ19-2, NAS19-6) in the matrix. The largest augite crystals reach about 200 μ m along the maximum axis; however, most do not exceed 100 μ m. Ca-poor pyroxene (pigeonite) was identified as small phenocrysts (KAS15-3, GUJ19-1, GUJ19-5), as inclusions in large plagioclase crystals (KAS15-3, GUJ19-1, GUJ19-5, KHK15-1, and 19M4), and in the groundmass (KAS15-3, GUJ19-5, KHK15-1, and 19M4). Oxides, mainly magnetite and rare ilmenite, are abundant as small crystals (<50 μ m) within the groundmass, of which they represent about 4-10 vol%.

Whole-rock and matrix compositions

Twenty-three whole-rock samples were analyzed for major and trace elements. We also analyzed the matrix for major and trace elements of ten samples. Matrix samples were obtained by crushing the rock to an approximate grain size of 100 μm and by

Table 1: Sampling coordinates and matrix and whole-rock compositions of the analyzed Deccan rocks

MATRIX								
Sample	MAL19-3	MAL19-4	MAL19-6	GUJ19-1	GUJ19-2	GUJ19-4	GUJ19-5	GUJ19-6
Latitude (N) Longitude (E)	23°06.370' 74°31.611'	22°34.098' 75°13.539'	22°18.697' 75°29.790'	20°13.746' 77°04.291'	21°43.863' 72°05.322'	22°12.421' 68°34.230'	22°30.530' 70°45.183'	22°38.145′ 70°53.108′
Area		Malwa Plateau				Saurashtra		
SiO ₂ wt%	50.08	47.53	48.28	49.07	54.12	48.22	48.72	47.08
TiO ₂	2.423	4.164	3.309	3.467	1.549	1.478	3.538	3.679
Al ₂ O ₃	13.23	11.89	12.49	12.37	14.70	13.85	12.50	12.55
FeO _t	14.04	17.62	15.87	16.36	10.85	13.61	15.81	15.98
MnO	0.232	0.292	0.244	0.237	0.158	0.225	0.223	0.265
MgO	5.25	4.83	5.01	5.30	4.35	6.40	5.09	5.26
CaO	10.44	8.68	9.87	9.56	7.92	11.69	9.24	10.28
Na ₂ O	2.53	2.30	2.62	2.56	2.84	2.43	2.40	2.39
K ₂ O	0.48	1.22	0.76	0.63	1.97	0.37	0.83	0.66
P_2O_5	0.239	0.272	0.354	0.361	0.251	0.203	0.304	0.371
Sum	98.93	98.79	98.82	99.58	98.70	98.47	98.66	98.51
LOI %	0.81	0.87	0.63	0.18	0.67	1.10	0.85	1.09
Ni ppm	43	43	55	41	15	64	65	52
Cr	34	51	42	25	11	119	105	50
Sc	38	36	37	35	31	48	33	37
La	16.27	22.59	30.26	26.47	35.12	11.81	25.34	28.05
Ce	37.05	49.48	66.35	54.28	70.91	23.12	57.02	62.59
Pr	5.06	6.63	8.63	6.91	8.50	2.86	7.73	8.32
Nd	22.83	28.60	36.92	28.58	33.75	12.14	33.64	35.91
Sm	6.02	7.42	8.69	7.05	7.14	3.20	8.60	8.85
Eu	2.12	2.29	2.80	2.22	1.96	1.28	2.69	2.91
Gd	6.73	7.81	8.97	7.66	6.99	4.05	9.20	9.15
Tb	1.19	1.31	1.47	1.31	1.13	0.75	1.50	1.48
Dy	7.06	7.70	8.60	7.84	6.90	4.99	8.68	8.79
Но	1.39	1.46	1.68	1.55	1.40	1.09	1.64	1.66
Er	3.59	3.80	4.27	3.94	3.63	2.92	4.12	4.18
Tm	0.49	0.51	0.59	0.54	0.53	0.44	0.57	0.56
Yb	2.90	2.99	3.42	3.28	3.13	2.66	3.29	3.23
Lu	0.44	0.44	0.52	0.51	0.50	0.43	0.49	0.49
Ba	132.37	227.55	243.28	267.55	400.63	138.14	199.78	220.81
Th	2.89	5.44	4.98	6.19	10.60	1.63	4.64	3.84
Nb	13.99	16.34	27.94	15.79	16.48	11.60	17.48	30.97
Y	34.55	36.41	40.27	37.84	34.92	26.97	40.59	40.34
Hf	4.24	6.03	6.35	5.30	5.86	1.98	6.49	6.38
Ta U	0.96 0.68	1.12	1.86 1.19	1.09	1.12 1.98	0.68 0.38	1.23 0.98	2.11 0.87
Pb	2.46	1.38 4.14	3.83	1.23 6.66	6.64	1.28	3.58	2.80
Rb	16.67	39.98	23.91	35.39	68.69	5.05	14.12	18.44
Sr	245.95	213.21	311.75	221.81	198.17	202.49	269.18	353.09
Zr	158.35	219.78	241.29	199.66	234.67	74.41	242.55	241.82
		213.70				, 1.11	212.33	
⁸⁷ Sr/ ⁸⁶ Sr	0.706309(5)		0.705995(5)	0.709675(6)	0.718463(6)			0.704984(4)
⁸⁷ Sr/ ⁸⁶ Sr _i ¹⁴³ Nd/ ¹⁴⁴ Nd	0.706125		0.705787	0.709242	0.717522			0.704842
143Nd/144Nd _i	0.512693(1)		0.512693(1)	0.512309(1)	0.511894(1)			0.512857(1)
_	0.512624		0.512631	0.512245	0.511839			0.512793
EpsilonNd _i ²⁰⁶ Pb/ ²⁰⁴ Pb	1.39 19.782(2)		1.53 19.634(1)	-6.02 19.120(1)	-13.93 21.735(1)			4.68 19.011(1)
²⁰⁷ Pb/ ²⁰⁴ Pb	19.782(2) 15.826(2)		19.634(1) 15.806(1)	19.120(1) 15.963(1)	16.101(1)			15.634(1)
²⁰⁸ Pb/ ²⁰⁴ Pb	40.494(4)		40.295(2)	40.846(1)	43.782(2)			39.623(2)
²⁰⁶ Pb/ ²⁰⁴ Pb _i	19.531		19.339	18.835	21.468			18.726
²⁰⁷ Pb/ ²⁰⁴ Pb _i	15.814		15.792	15.949	16.089			15.620
²⁰⁸ Pb/ ²⁰⁴ Pb _i	40.191		39.943	40.673	43.359			39.259
	MA	ΓRIX			WHOLE	ROCKS		
Sample	19M-4	KAS19-1	MAL19-3	MAL19-4	MAL19-5	MAL19-6	GUJ19-1	GUJ19-2
Latitude (N)	17°55.507'	19°41.046'	23°06.370'	22°34.098'	22°22718'	22°18.697'	20°13.746'	21°43.863'
Lautude (N) Longitude (E)	73°37.430'	73°30.793'	74°31.611'	75°13.539'	75°28.842	75°29.790'	77°04.291'	72°05.322'
					:			

(Continued)

Table 1: Continued.

Area	Wester	Western Ghats		Malwa Plateau				Saurashtra	
SiO ₂ wt%	49.07	46.94	49.89	49.91	49.06	48.36	48.03	53.89	
TiO ₂	3.467	3.113	2.173	2.212	2.842	3.005	2.538	1.406	
Al ₂ O ₃	12.37	12.82	14.49	15.34	13.16	13.86	15.78	16.06	
FeO _t	16.36	15.26	12.78	12.16	14.01	13.89	13.10	9.82	
MnO	0.237	0.197	0.206	0.171	0.227	0.215	0.164	0.141	
MgO	5.30	5.96	5.05	4.79	5.03	5.08	5.15	4.09	
CaO	9.56	10.23	10.73	9.51	10.37	10.09	9.76	8.51	
Na ₂ O	2.56	2.49	2.54	2.62	2.53	2.67	2.82	2.89	
K ₂ O	0.63	0.86	0.41	0.95	0.39	0.53	0.97	1.81	
P ₂ O ₅	0.361	0.259	0.203	0.215	0.268	0.308	0.264	0.219	
Sum	99.92	98.12	98.47	97.89	97.89	98.02	98.59	98.83	
LOI %	0.00	1.37	1.14	1.86	1.84	1.67	1.20	0.81	
Ni ppm	57	101	45	32	55	50	86	17	
Cr	77	244	41	53	39	34	146	13	
Sc	38	34	33	27	35	34	26	29	
<u></u>	30	34	33	21		34	20	23	
La	23.67	19.56	14.37	18.49	19.92	27.10	20.98	32.85	
Ce	53.98	43.38	32.45	40.12	45.43	59.34	45.38	65.62	
Pr	7.28	5.87	4.44	5.37	6.19	7.74	6.09	7.83	
Nd	32.40	26.66	19.82	23.25	26.95	32.75	26.65	30.55	
Sm	8.34	6.98	5.45	6.09	7.09	7.85	6.84	6.73	
Eu	2.66	2.28	1.90	1.96	2.35	2.53	2.29	1.79	
Gd	9.24	7.62	5.98	6.31	7.48	7.90	7.29	6.37	
Tb	1.51	1.27	1.03	1.06	1.26	1.29	1.20	1.06	
Dy	9.11	7.57	6.23	6.11	7.38	7.65	7.03	6.36	
Но	1.79	1.49	1.22	1.19	1.43	1.46	1.37	1.28	
Er	4.54	3.74	3.16	2.99	3.68	3.73	3.56	3.29	
Tm	0.63	0.51	0.43	0.41	0.50	0.51	0.48	0.46	
Yb	3.69	3.00	2.58	2.41	2.96	3.00	2.84	2.88	
Lu	0.57	0.46	0.39	0.36	0.45	0.44	0.43	0.44	
Ва	186.93	249.21	116.39	195.31	161.40	213.82	277.95	372.82	
Th	3.04	2.45	2.56	4.30	2.93	4.45	2.33	9.79	
Nb	21.78	11.92	12.25	10.91	18.18	24.98	11.95	15.07	
Y	43.41	35.91	30.05	29.15	35.47	35.65	33.80	31.74	
Hf	6.11	5.40	3.78	4.52	4.99	5.64	5.09	5.45	
Ta	1.46	0.78	0.86	0.79	1.25	1.72	0.81	1.04	
U	0.72	0.47	0.60	1.06	0.82	1.04	0.51	1.81	
Pb	3.21	3.26	2.13	5.16	2.33	3.17	3.37	6.25	
Rb	16.08	13.79	13.82	29.65	11.98	17.99	20.27	61.35	
Sr	247.88	232.82	256.70	262.84	275.64	333.31	286.18	218.15	
Zr	233.85	198.50	134.37	162.30	185.02	212.76	186.77	214.07	
87 Sr/86 Sr	0.705068(5)	0.709494(3)							
87 Sr/86 Sr _i	0.704893	0.709333							
¹⁴³ Nd/ ¹⁴⁴ Nd									
¹⁴³ Nd/ ¹⁴⁴ Nd _i	0.512685(1) 0.512618	0.512330(1) 0.512261							
*									
EpsilonNd _i ²⁰⁶ Pb/ ²⁰⁴ Pb	1.27	-5.69							
²⁰⁰ Pb/ ²⁰⁴ Pb	17.990(1)	18.460(1)							
²⁰⁸ Pb/ ²⁰⁴ Pb	15.490(1)	15.681(1)							
	38.329(2)	39.672(2)							
²⁰⁶ Pb/ ²⁰⁴ Pb _i	17.804	18.330							
²⁰⁷ Pb/ ²⁰⁴ Pb _i	15.481	15.675							
²⁰⁸ Pb/ ²⁰⁴ Pb _i	38.095	39.486							

				WHOLE ROCKS				
Sample	GUJ19-3	GUJ19-4	GUJ19-5	GUJ19-6	NAS19-6	GNG-498	KAS19-1	KAS15-3
Latitude (N) Longitude (E)	21°21.504' 71°53.958'	22°12.421' 68°34.230'	22°30.530' 70°45.183'	22°38.145' 70°53.108'	17°14.396' 77°53.648'	17°20.637' 77°35.30'	19°41.046' 73°30.793'	19°38.327' 73°28.991'
Area	Saurashtra				SE-D	eccan	Western Ghats	
SiO ₂ wt%	50.19	48.31	49.61	47.21	49.32	49.32	48.16	50.41
TiO ₂	1.312	1.167	3.121	3.358	3.322	2.94	2.253	3.02
Al_2O_3	15.80	15.68	13.71	13.80	13.84	13.28	15.37	13.44
FeOt	13.15	11.94	14.31	14.78	12.49	13.96	12.13	14.13

(Continued)

Table 1: Continued. MnO 0.205 0.199 0.222 0.170 0.20 0.143 0.21 MgO 4.97 5.91 4.85 5.06 4.80 4.59 5.50 4.51 9.26 9.01 CaO 8.97 11.84 9.38 10.32 9.62 10.42 Na₂O 2.97 2.44 2.57 2.41 2.53 2.50 2.68 2.70 K₂O 0.78 0.32 0.82 0.62 0.54 0.59 0.76 1.07 P2O5 0.190 0.181 0.288 0.328 0.342 0.31 0.219 0.28 Sum 98.51 98.00 98.86 98.10 96.98 96.96 97.63 98.79 0.90 0.63 LOI % 0.91 1.61 1.44 2.40 2.52 1.79 62 51 102 36 Ni ppm 12 61 52 64 99 28 Cr 4 81 53 84 62 202 29 41 30 34 31 32 29 30 Sc 24.29 10.36 24.22 25.57 22.77 23.66 17.18 24.80 La 55.03 Ce 48.23 20.18 53.92 56.89 50.91 52.68 37.77 7.09 7.40 Pr 5.84 2.46 7.22 7.55 6.86 5.05 32.50 23.07 31.51 32.47 30.27 22.17 Nd 10.47 31.10 5.58 2.74 8.18 8.16 7.75 8.28 6.04 8.26 Sm Eu 1.69 1.18 2.57 2.73 2.53 2.58 2.02 2.64 Gd 6.16 3.43 8.44 8.39 8.29 8.58 6.51 8.37 Tb 1.06 0.64 1.40 1.36 1.35 1.41 1.07 1.34 8.04 7.78 8.12 6.40 7.78 Dy 6.66 4.18 8.48 0.90 1.23 1.49 Но 1.37 1.54 1.47 1.57 1.62 Er 3.62 2.54 3.92 3.72 3.95 4.13 3.20 3.85 Tm 0.50 0.38 0.52 0.51 0.53 0.56 0.42 0.52 Yb 3.12 2.33 3.09 2.92 3.14 3.32 2.58 3.04 0.45 Lu 0.46 0.37 0.45 0.43 0.48 0.37 0.45 277.06 121.71 188.23 196.44 169.14 221.73 223.38 237.50 Ва Th 4.29 2.65 2.09 4.22 6.15 1.45 3.45 3.46 Nb 9.40 9.61 15.69 28.14 20.38 13.65 9.48 15.25 Υ 33.92 22.93 37.32 36.07 38.25 39.63 30.43 37.16 Ηf 4.16 1.63 5.97 5.74 5.44 5.90 4.45 5.95 1.09 Ta 0.65 0.59 1.13 1.92 1.37 0.93 0.68 0.98 U 1.16 0.34 0.94 0.79 0.60 0.75 0.40 Pb 6.71 1.06 3.12 2.33 3.20 3.82 2.74 3.81 Rb 4.10 13.15 19.85 13.73 16.97 11.79 28.98 65.42 Sr 178.97 212.05 270.27 370.20 324.48 265.50 262.27 282.14 155.92 62.56 218.01 223.23 163.54 220.73 Zr 216.18 206.62

WHOLE ROCKS							
Sample	MAT14-2	KHK15-1	19M-4	19P-5	JATH17-3	TM18-3	KH-275
Latitude (N)	19°00.436'	18°45.728'	17°55.507'	18°16.855'	17°00.970'	21°50.724'	22°19.347'
Longitude (E)	73°18.534'	73°21.13'	73°37.430'	73°58.843'	75°12.239'	74°27.354'	75°03.163'
Area		Wester	n Ghats			Northern Deccan	
SiO ₂ wt%	48.95	50.08	49.50	48.21	48.52	50.01	49.43
TiO ₂	3.26	3.18	3.329	2.650	2.73	3.01	3.20
Al_2O_3	12.96	13.77	13.22	17.57	14.15	13.57	13.52
FeO _t	15.32	13.42	15.09	11.36	12.26	12.68	14.18
MnO	0.22	0.20	0.226	0.147	0.18	0.19	0.22
MgO	4.24	4.82	5.20	3.36	5.54	5.26	4.41
CaO	9.11	8.94	9.67	10.48	10.14	9.69	9.38
Na ₂ O	2.76	2.51	2.68	2.79	2.37	2.52	2.74
K ₂ O	0.54	1.03	0.59	0.36	0.41	0.88	0.87
P_2O_5	0.36	0.35	0.337	0.272	0.26	0.38	0.35
Sum	97.73	98.28	99.84	97.21	96.57	98.19	98.29
LOI %	1.76	1.18	0.00	2.38	2.73	1.07	1.04
Ni ppm	64	61	55	78	89	67	45
Cr	127	101	76	119	156	127	56
Sc	39	32	36	22	31	31	33
La	27.62	22.07	22.46	22.07	21.70	29.42	34.21
Ce	61.02	47.16	50.84	47.16	48.07	65.04	72.88
Pr	8.11	6.26	6.87	6.26	6.32	8.63	9.29
Nd	35.62	26.69	30.59	26.69	27.24	36.98	38.85
Sm	8.83	6.54	7.93	6.54	6.78	8.72	9.18
Eu	2.80	2.28	2.63	2.28	2.31	2.72	2.84
Gd	9.20	6.67	8.61	6.67	7.01	8.71	9.08

TITLOT E DOCTO

Table 1: Co	Table 1: Continued.								
Tb	1.52	1.06	1.42	1.06	1.11	1.40	1.43		
Dy	8.72	6.20	8.42	6.20	6.54	8.12	8.57		
Но	1.67	1.18	1.66	1.18	1.24	1.51	1.65		
Er	4.20	2.98	4.23	2.98	3.22	3.92	4.28		
Tm	0.56	0.40	0.58	0.40	0.43	0.53	0.58		
Yb	3.37	2.32	3.52	2.32	2.52	3.11	3.47		
Lu	0.50	0.34	0.51	0.34	0.39	0.46	0.51		
Ва	250.97	146.93	176.49	146.93	189.07	239.97	288.69		
Th	4.62	2.71	2.84	2.71	3.21	3.49	6.31		
Nb	17.06	21.08	20.28	21.08	19.27	25.23	29.74		
Y	41.09	28.61	40.69	28.61	30.75	37.73	40.71		
Hf	6.32	4.63	5.68	4.63	4.65	6.42	6.66		
Ta	1.17	1.44	1.39	1.44	1.29	1.68	2.04		
U	1.05	0.56	0.67	0.56	0.65	0.77	1.45		
Pb	3.81	2.31	2.90	2.31	2.81	3.31	4.90		
Rb	28.63	12.04	14.84	12.04	5.62	22.88	31.38		
Sr	292.93	403.59	250.21	403.59	329.25	303.64	326.76		

177.84

179.02

252.59

252.92

WHOLE-ROCKS								
Sample	SSF20-2	SK20-1	JD20-1					
Latitude (N)	20°44.485'	23°25.481'	22°51.279'					
Longitude (E)	073°57.043'	78°37.358'	079°46.337'					
SiO ₂ wt%	47.52	49.34	48.35					
TiO ₂	4.12	2.94	3.32					
Al ₂ O ₃	13.14	14.06	13.69					
FeO _t	15.65	13.20	13.78					
MnO	0.22	0.20	0.221					
MgO	4.96	5.53	5.45					
CaO	9.94	9.73	10.43					
Na ₂ O	2.32	2.74	2.46					
K ₂ O	0.61	0.63	0.23					
P ₂ O ₅	0.42	0.34	0.359					
Sum	98.90	98.71	98.28					
LOI %	0.73	1.03	1.45					
Ni ppm	97	64	93					
Cr	168	84	173					
Sc	28	31	35					
La	22.34	25.16	19.48					
Ce	52.40	55.50	44.75					
Pr	7.45	7.38	6.16					
Nd	33.78	31.73	28.15					
Sm	9.24	7.38	7.38					
Eu	2.96	2.40	2.5					
Gd	10.07	7.51	8.28					
Tb	1.70	1.19	1.4					
Dy	9.95	7.02	8.35					
Но	2.02	1.38	1.67					
Er	4.99	3.46	4.18					
Tm	0.67	0.47	0.57					
Yb	4.08	2.72	3.4					
Lu	0.62	0.41	0.53					
Ва	137.88	220.88	111					
Th	2.59	2.99	2.33					
Nb	23.05	21.77	19.46					
Y	47.82	33.35	40.19					
Hf	6.72	5.42	5.47					
Ta	1.63	1.47	1.36					
U	0.63	0.67	0.55					
Pb	2.32	3.20	2.09					
Rb	15.55	17.41	4.1					
Sr	226.47	331.25	237.2					
Zr	253.45	210.70	210					

237.09

177.84

216.02

Major elements in wt%, trace elements in ppm. Ni, Cr, Sc, V XRF data, all other trace elements ICP-MS data. FeOt, total iron; LOI, loss on ignition. Initial isotopic data are recalculated to an age of 66 Ma. Number in brackets for the measured isotopic compositions refer to the 2-sigma analytical uncertainty.

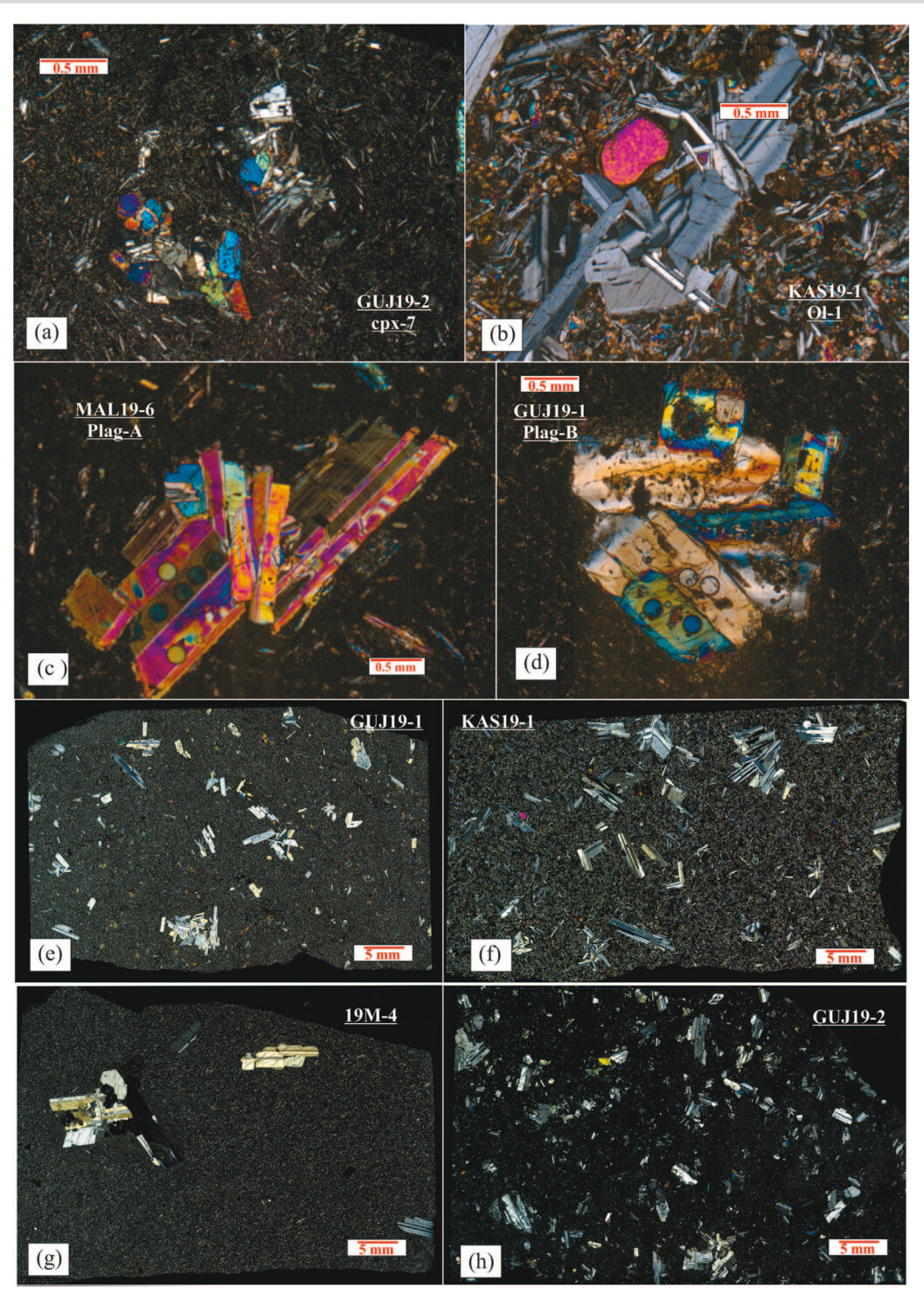


Fig. 3. Cross-polarized thin section images from the studied Deccan basalts. (a) Small clinopyroxene crystal aggregate from GUJ19-2. (b) A relatively large olivine crystal from sample KAS19-1. (c, d) Cross-polarized images of 100 micron thick sections of samples MAL19-6 (Plag-A) and GUJ19-1 (Plag-B); note that small and large circles are due to laser ablations for trace element and Sr-isotope analyses, respectively. (e-h) Cross-polarized scans of entire thin sections of samples GUJ19-1, KAS19-1, 19M-4, and GUJ19-2.

then picking out the plagioclase grains. On seven of the matrix samples and on one whole rock (MAT14-2) we obtained Sr-Nd-Pb isotopic compositions. The whole-rock and matrix compositions are reported in Table 1.

According to the total-alkali silica diagram (Le Bas et al., 1986; Electronic Appendix 1, Fig. S1) the whole rocks are basalts (SiO₂ 48.0-51.0 wt%), except GUJ19-2 (SiO₂ 54.5 wt%), which is a basaltic andesite. The MgO of all samples is relatively low (6.0-3.5 wt%),

while FeOt (total iron) and TiO2 are high (11.5-15.7 wt% and 2.3-4.2 wt%, respectively) except in GUJ19-2 and GUJ19-4 (TiO2 1.2-1.4 wt%) (Fig. 4). The FeOt/MgO ratio (>2.0) of all GPBs, including data from previous studies (e.g. Beane et al., 1986) are among the highest of all Deccan rocks (Fig. 4e). Most of the whole rocks have major element compositions, which overlap with evolved Deccan basalts from the Kalsubai or Wai subgroups, which are Fe and Ti-rich, whereas GUJ19-2 resembles the low-Ti composition of

Table 2: Considered plagioclase-melt partition coefficients (Ds) for An₇₀₋₆₅ plagioclase compositions

Ti ¹	Fe ²	K ³	Rb^3	Mg^3	Sr ³	Ba ³	La ³	Ce ³	Eu4
0.038	0.045	0.24	0.05	0.34	2.1	0.18	0.05	0.045	0.3

¹From Aigner-Torres et al. (2007). ²Calculated after Laubier et al. (2014). ³Calculated after Sun et al. (2017) for An₇₀. ⁴Calculated after Dygert et al. (2020). Plagioclase/melt Ds were experimentally obtained in several recent studies (Aigner-Torres et al., 2007; Tepley et al., 2010; Laubier et al., 2014; Sun et al., 201 Dygert et al., 2020). As the Ds may significantly depend on the plagioclase composition and on crystallization temperature and considering that the cited studies obtained significantly different results for Ds of some elements, we considered partition coefficients appropriate for the studied plagioclase crystals. Sr, Ba, Mg, and K partition coefficients vary with An. Although most experimental studies indicate that Sr and Ba partition coefficients increase at decreasing An, for Mg and K there are contradictory results. For example, Bindeman et al. (1998) measured a decreased incompatibility of Mg and K at decreasing An, Sun et al. (2017) obtained opposite trends. However, in general all studies agree that for these elements the change in Ds is 20–30% from An78 to An60, i.e. for the range of the plagioclase crystals analyzed here. The Eu and Fe Ds are strongly controlled by the fO2 and are here calculated according to Dygert et al. (2020) and Laubier et al., 2014) for fO_2 in the range QFM to QFM-1 at a temperature of 1150° C. Plagioclase/basalt partition coefficients.

evolved Lonavala subgroup basalts, from the Bushe formation in particular.

Compared with whole-rock samples, matrix samples are enriched in FeOt (by 1.0-5.4 wt%, mean 1.9 wt% enrichment) and TiO₂ (up to 2.0 wt%, mean 0.5 wt%) and depleted in Al₂O₃ (0.9-3.6 wt%, mean 1.9 wt% depletion), CaO (mean 0.4 wt%) and Na_2O (mean 0.13 wt%). The FeO_t (13.8–17.8 wt%) and TiO_2 (2.5-4.2 wt%) contents of most matrices are among the highest of Deccan samples. The difference between whole-rock and matrix compositions can be used to calculate by mass balance the amount of plagioclase megacrysts, which ranges from 6 to 26 wt% (mean 11 wt%) and is broadly consistent with petrographic observations.

The trace element contents of whole rocks are generally slightly depleted compared with matrix samples, except for Sr, which is enriched in whole-rock samples. Trace element ratios vary relatively little between matrix and whole rocks, except for those ratios involving elements that are compatible (Sr, crystal/melt partition coefficient = D > 1.0) or moderately incompatible in plagioclase (Ba, Eu, partition coefficient D = 0.1-1.0; see Table 2 for plagioclase/melt partition coefficients used).

The trace element contents and ratios display a relatively large variation among the studied samples (Figs 4 and 5) For example, La/Yb varies from 4.4 (GUJ19-4) to 11.3 (GUJ19-2), Zr/Nb from 6.5 (GUJ19-4) to 17.3 (KAS19-1), Zr/Y from 2.8 (GUJ19-4) to 6.8 (GUJ19-2), and Nb concentration from 10 (GUJ19-4) to 31 ppm (GUJ19-6). Several of the studied rocks and matrix samples yield higher Nb contents than those of previously analyzed Deccan basalts (Fig. 4f). On the primitive-mantle normalized multielement diagram, all samples display broadly similar patterns and are enriched in very incompatible elements, compared with moderately incompatible ones. The most depleted sample for almost all elements is GUJ19-4, which shows marked negative anomalies for Rb, K, Ta, Pb, Zr and Hf, and the lowest Nb, FeOt/MgO and Zr/Y of all GPBs (Figs 4e,f and 5). Its trace element pattern is relatively little enriched in very to moderately incompatible trace elements. This is confirmed also by the Rare Earth Element (REE) pattern (chondrite-normalized values; Fig. 5e), which for GUJ19-4 is moderately enriched in light/middle REE (La/Sm_{CN} 2.3) and nearly flat from middle to heavy REE (Sm/Yb_{CN} 1.3) and shows a positive Eu anomaly $(Eu_{CN}/(Sm_{CN} \times Gd_{CN})^{0.5} = Eu/Eu* = 1.18$ for the whole-rock sample and 1.08 for the matrix sample). On the other hand, the sample that is most enriched in highly incompatible elements is GUJ19-2 (La/Yb_{CN} = 7.7; Ba/Y = 11.7), whose trace element pattern is characterized by marked negative anomalies for Ba, Nb-Ta, Sr, while its Pb shows a slightly positive anomaly. The REE pattern of GUJ19-2 is characterized by high La/Sm_{CN} (3.1) combined with by Sm/Yb_{CN} (2.3) that is slightly lower than most other samples (2.3–3.0), and by a clear negative Eu anomaly (Eu/Eu*=0.83 for the GUJ19-2 whole-rock sample and 0.85 for

the matrix sample). All other samples show similar REE patterns, which are moderately enriched in light vs. middle and heavy REE. However, these samples are clearly different in their high field strength elements and large ion lithophile elements. For example, Nb/La_N and Ce/Pb_N vary from high values in GUJ19-6 (1.1 and 2.2, respectively), to intermediate values for NAS19-6, MAL19-3, MAL19-6, GUJ19-4 and 19M-4 (Nb/La_N 0.85–0.93, Ce/Pb_N 1.4–1.7) to low values for MAL19-4, GUJ19-1, GUJ19-2, GUJ19-5, KAS19-1 (Nb/La_N 0.46-0.65, Ce/Pb_N 0.7-1.5).

Sr-Nd-Pb isotopic data of matrix samples recalculated to an eruption age of 66 Ma show generally correlated variations for the seven analyzed samples (Fig. 6). GUJ19-6 shows the lowest 87 Sr/ 86 Sr_i (0.7048) and highest 143 Nd/ 144 Nd_i (0.51278, ε Nd +4.7). On the enriched end of the Sr-Nd isotopic spectrum lies GUJ19-2, which has very high Sr isotope ratio (0.7157) and low Nd isotopic compositions ($\varepsilon Nd_i - 13.9$). Samples 19M-4, MAL19-3, MAL19-6 plot at relatively low 87 Sr/86 Sr_i and high 143 Nd/144 Nd_i, while GUJ19-1 and KAS19-1 are high in 87 Sr/ 86 Sr_i and low in ε Nd_i. 206 Pb/ 204 Pb_i, $^{207}\mbox{Pb}/^{204}\mbox{Pb}_{\mbox{\scriptsize i}},~^{208}\mbox{Pb}/^{204}\mbox{Pb}_{\mbox{\scriptsize i}}$ isotopic compositions are correlated, with 19 M-4 plotting at the depleted end and GUJ19-2 being the most enriched sample. The correlation of Pb isotopic ratios with $^{87}\text{Sr/}^{86}\text{Sr}_{ ext{i}}$ or $arepsilon ext{Nd}_{ ext{i}}$ is in general poor. In particular, GUJ19-6, the most depleted sample in Sr-Nd isotopic space is slightly higher in ²⁰⁶Pb/²⁰⁴Pb_i than samples 19 M-4 and KAS19-1 and just slightly lower than GUJ19-1. Sr-Nd isotopic compositions are generally well correlated with incompatible element ratios such as Nb/La or Ce/Pb (not shown), while these correlations are very scattered for Pb isotopic compositions.

Mineral compositions

Plagioclase

Plagioclase megacrysts from 14 samples were analyzed by EMP. Among these, a total of 33 megacrysts from 11 samples were analyzed for detailed core-rim crystal traverses (Fig. 8; Electronic Appendix 2, Table S2, S3). The EMP traverses are 1.9–0.25 mm long, with a pacing between analysis spots of around 10 μ m in most crystals and c. 20 μ m in a few. Plagioclase major element compositions are reported in the Electronic Appendix 2, Supplementary Table S3.

Figure 7 shows the measured compositional ranges for all samples analyzed including traverses and spot analyses of cores (samples GUJ19-1, GUJ19-2, GUJ19-5, MAL19-4, KAS15-3, KHK15-1, 19M4, and 19P5) and the traverses. All samples except GUJ19-4 overlap the averaged core compositions of megacrysts from six GPBs in the Kalsubai subgroup (Hooper et al., 1988). Anorthite contents (An) range from 53 to 82 (mol%); most plagioclase crystals are labradorite (An₆₀₋₇₀), while bytownite is also present in six samples. In five samples (GUJ19-2, GUJ19-4, GUJ19-5, MAL19-4, 19M-4) the plagioclase crystals are nearly unzoned, i.e. with less than 5 mol% An variations for crystals showing

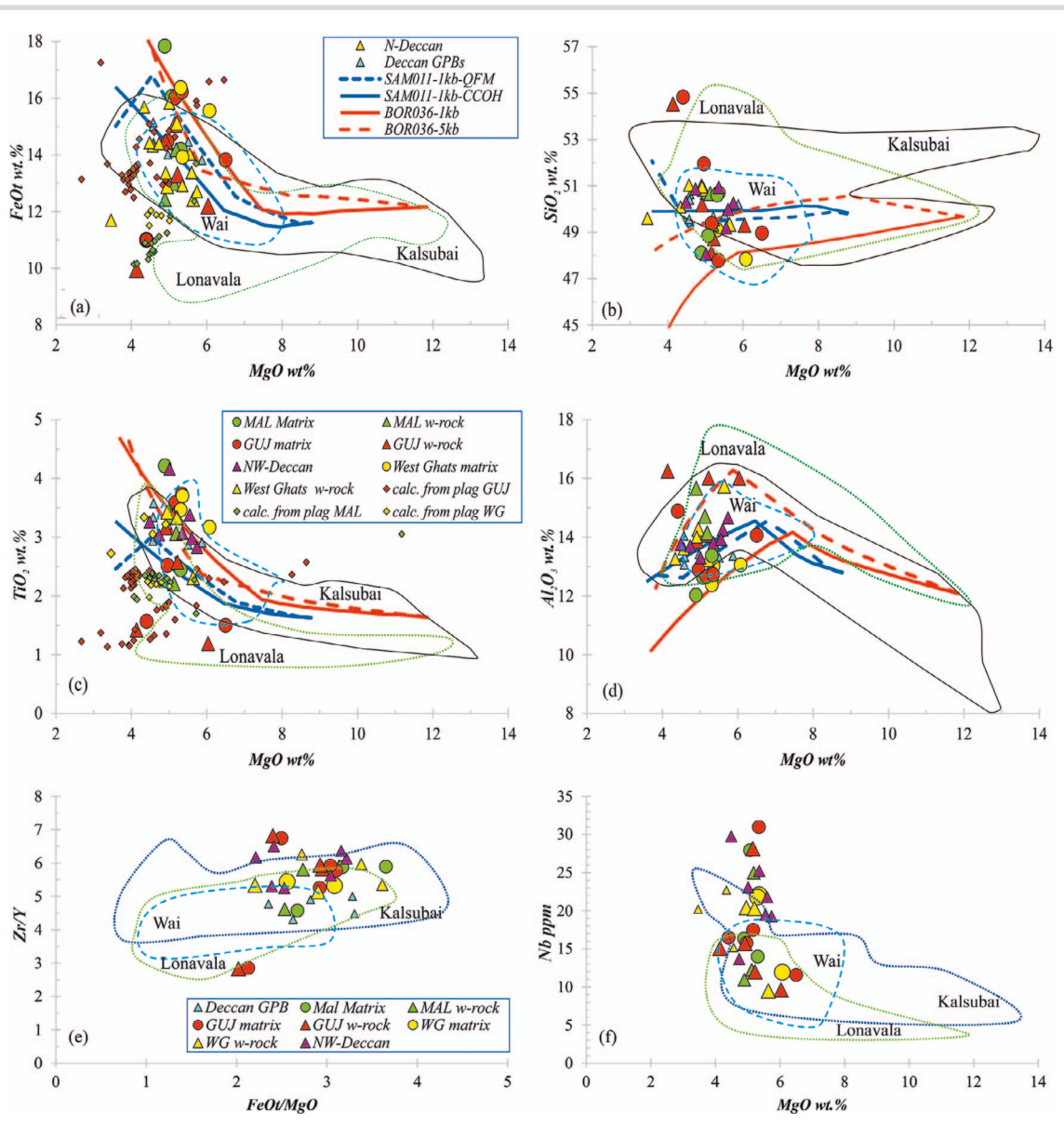


Fig. 4. Major and trace element variations of the studied Deccan samples and of previously analyzed basalts (GEOROC database) of the Kalsubai (lower Fms., black dotted contour), Lonavala (middle Fms., green dotted contour), and Wai subgroup (upper Fms., blue dashed contour). Presently studied samples include whole rocks (large triangles) and matrix (large circles) from Gujarat-Saurashtra (GUJ samples, red symbols), the Malwa Plateau (MAL samples, green symbols), the WG (KAS19-1, 19 M-4 and other samples listed in Table 1; yellow symbols), and the north-western Deccan (purple triangles). Also plotted are previously analyzed GPB samples (blue triangles) from Beane et al. (1986). Rhyolite-MELTS liquid lines of descent calculated starting from SAM011 and BOR036 (from Beane et al., 1986) at 0.1 and 0.5 GPa (SAM011 only at 0.1GPa), fO2 at QFM or COH buffer (SAM011) or unbuffered (BOR036), all run anhydrous. Also reported are compositions calculated to be in equilibrium with plagioclase megacrysts (LA-ICP-MS Mg, Fe, Ti data; Table 3; Ds are reported in Table 2).

optical evidence of oscillatory zoning (e.g. crystals from 19 M-4, Fig. 2e). However, in six samples (GUJ19-1, GUJ19-2, GU19-6, MAL19-3, MAL19-6, KAS19-1; Fig. 8) all analyzed crystals show a significant zoning in terms of An. This zoning is generally normal (i.e. rimward decrease of An; e.g. GUJ19-1, GUJ19-6, MAL19-6, KAS19-1; Fig. 8a, I, m, q) and occasionally reverse (e.g. GUJ19-2; Fig. 8e). An decreases of 5-10 mol% near the rim are seen in about half of the analyzed crystals, whereas An remains near-constant in the others. In a few samples, the An contents vary either near the core (MAL19-6, Plag-3) or near the rim (GUJ19-1, plag-1) or throughout the crystal (GUJ19-4, Plag-1; Electronic Appendix 2, Table S2). In five samples, at least one plagioclase crystal shows a resorbed inner core with >5 mol% An higher than the adjacent regions.

Minor element (K, Mg, Fe; Fig. 8) variations tend to be consistent with An variations. K2O displays core-rim variations that are roughly anticorrelated to those of An, e.g. low K2O corresponds to high An. High-An resorbed cores tend to be depleted in K2O compared with the rest of the crystal. Plagioclase crystals of some samples (GUJ19-4, MAL19-3, 19M-4, and NAS19-6; Electronic Appendix 2, Table S2) are depleted in K2O compared with crystals with similar An in other samples. In contrast, sample GUJ19-2 shows the highest K2O in plagioclase for a given An. The MgO contents in plagioclase range between about 0.05 and 0.25 wt% and are not correlated with An. Within crystal variations are generally negligible, i.e. the MgO profiles are nearly flat. Although the MgO contents are low and thus close to detection limit (c. 0.05 for EMP analysis), we could expect a detectable change at

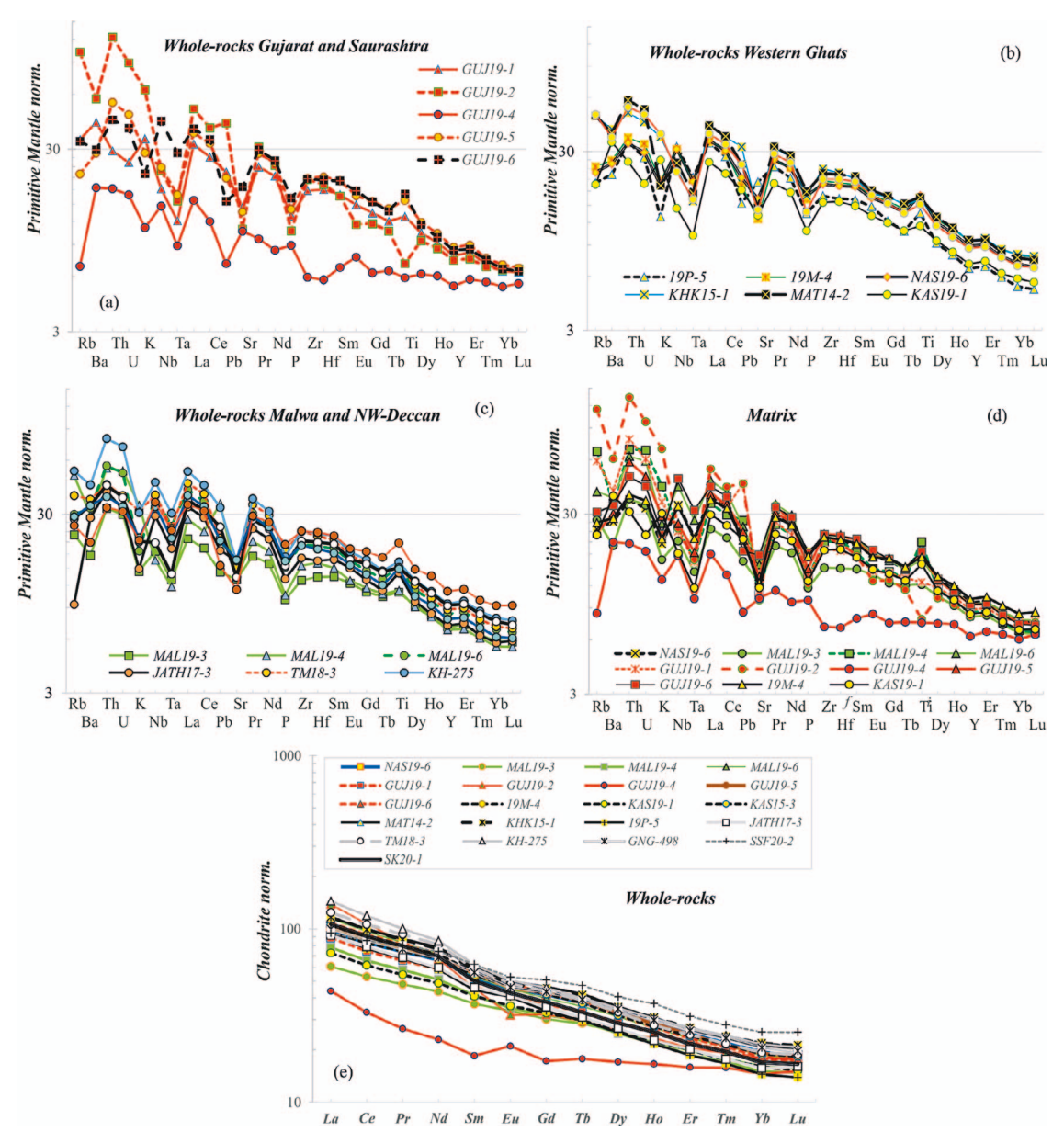


Fig. 5. (a-d) Primitive mantle-normalized (McDonough & Sun, 1995) trace element contents of analyzed whole rocks (a-c) and matrix samples (d). (e) Chondrite-normalized (McDonough & Sun, 1995) REE pattern of analyzed whole rocks. Matrix compositions are not plotted for REE as they are quite similar to those of whole rocks, except for Eu, which is on average c. 5% depleted in matrix vs whole-rock composition.

least when An varies by more than 10 mol%. FeOt contents range from about 0.40 to 0.90 wt% for all crystals and are generally not correlated with An. However, FeO_t contents increase significantly (by 0.10-0.30 wt%, i.e. by about 30-100% relative) in the last 50-100 μ m near the crystal rims in 13/33 of the analyzed crystals from most of the samples analyzed in detail (8/11).

Trace elements were collected in five samples and nine plagioclase crystals by LA-ICP-MS (Fig. 9; Electronic Appendix 2, Supplementary Table S4) along core-rim traverses close to those analyzed by EMP. Images of analyzed crystals with laser spots are shown in Fig. 3c,d and in the Electronic Appendix 1, Supplementary Figs S2, S3. Due to the c. $40-\mu$ m-diameter analytical spot size, we could not analyze the outermost rims as in EMP analyses. The spacing between consecutive spots is not constant as we tried to avoid altered or fractured areas. In two sieved-textured plagioclase crystals, a few analysis spots involved parts of the melt or matrix replacing the dissolved plagioclas, and were discarded. In general, trace elements that yielded values close to detection limit were also discarded. We focused on the concentrations of Sr, Ba, Ce, La, Eu, Li, Y, and Rb (the latter three elements not shown in Fig. 9). Minor elements like K, Mg, Fe, and Ti were also analyzed by LA-ICP-MS and yielded results that are generally consistent with those obtained by EMP.

The trace element contents in plagioclase megacrysts are broadly correlated with their whole-rock and matrix compositions. However, the plagioclase crystals of GUJ19-1 are relatively poor in Ba and Sr even though the matrix and whole rock of this sample are relatively rich in these elements.

The trace element contents generally show small core-rim variations and small differences between crystals from the same rock. However, sample GU19-1 again shows an anomalous behavior; its plagioclase crystals have cores with Ti close to 250-300 ppm and K c. 1200 ppm, while Ti increases to c. 380 ppm and K to c. 1700 ppm in one crystal's outer half. The Mg content of GUJ19-

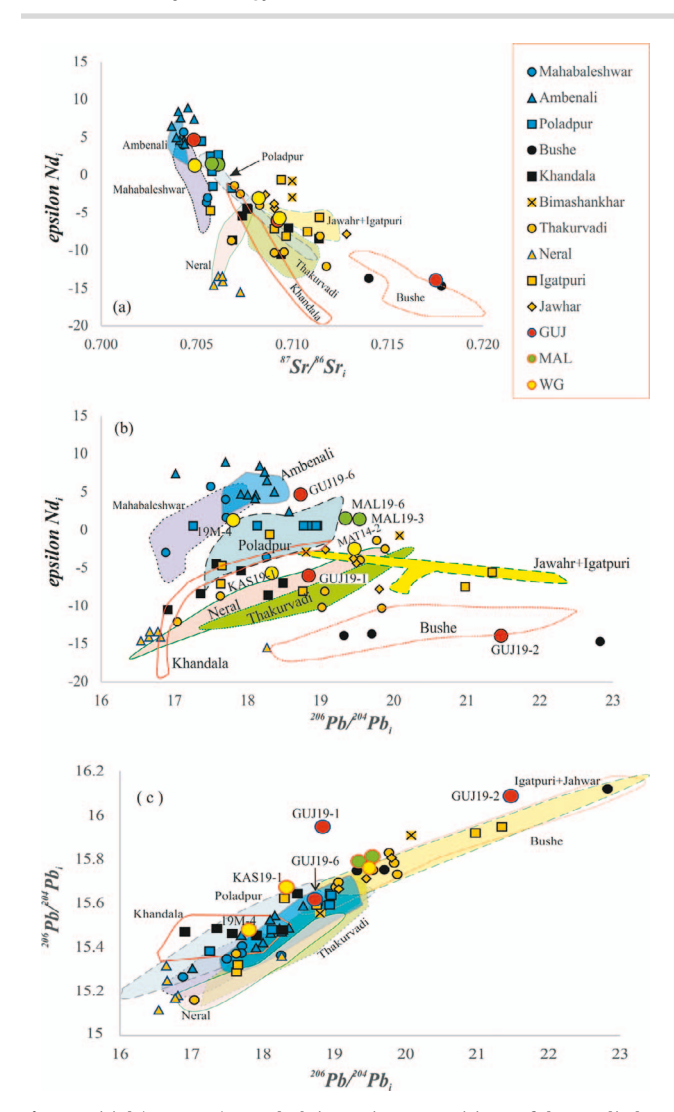


Fig. 6. Initial (at 66 Ma) Sr-Nd-Pb isotopic compositions of the studied rocks (larger symbols with label) and of Deccan basalts from the WG (smaller symbols, data from Basu et al., 2020a). GUJ samples are GUJ19-1, GUJ19-2 (most radiogenic Sr-Pb isotopic values), and GUJ19-6 (less radiogenic values); MAL samples are MAL19-3 and MAL19-6; WG samples are KAS19-1 (higher Sr-Pb) and 19 M-4 (lower Sr-Pb). Fields plotted in diagrams are from Peng et al. (1994, 2014), Vanderkluysen et al. (2011), and Basu et al. (2020a).

1 Plag-A shows a marked decrease from core to rim, which is paralleled by a drop in An from c. 76 to 65. Plagioclase data for this same sample show significant differences in terms of Ba, La, Ce, Eu, and Mg between the two analyzed crystals.

⁸⁷Sr/⁸⁶Sr isotopic compositions in plagioclase were analyzed for five rock samples on a total of nine plagioclase crystals (Fig. 10; Table 3). Each of the 51 analyzed spots has a diameter of 154 μ m; therefore, two analyses of a sieve-textured core (in GUJ19-1) are a mixture of the plagioclase with its dissolved, glassy parts. Due to the relatively large spot size, the outermost rim could not be analyzed (Fig. 3c,d; Electronic Appendix 1, Supplementary Figs S2 and S3).

In general, the initial isotopic compositions (recalculated to an age of 66 Ma) of the five samples are correlated with the isotopic composition of the matrix samples (Fig. 10f), i.e. the ⁸⁷Sr/⁸⁶Sr_i of plagioclase from GUJ19-6 and 19 M-4 are relatively low (c. 0.7043-0.7050), those from MAL19-6 are intermediate (c. 0.7056) and those from KAS19-1 and GUJ19-1 are high (0.7092-0.7107).

In detail, however, all analyzed plagioclase spots from GUJ19-6 are significantly lower than the matrix composition (considering 2 sigma uncertainty on the LA-ICP-MS and matrix analyses). Likewise, most plagioclase spots of MAL19-6 have ⁸⁷Sr/⁸⁶Sr_i lower than the respective matrix while most of GUJ19-1 have higher ⁸⁷Sr/⁸⁶Sr_i than the respective matrix. Core-rim or inter-crystal variations of ⁸⁷Sr/⁸⁶Sr_i are negligible in GUJ19-6 and in KAS19-1, but are significant in GUJ19-1, MAL19-6, and 19M-4. In particular, GUJ19-1 shows significantly different 87 Sr/86 Sr_i in the two analyzed crystals. In its Plag-B, the two apparently inner analysis spots have lower ⁸⁷Sr/⁸⁶Sr_i than the two outer spots. However, the portion of the crystal that yielded the highest 87 Sr/86 Sr_i seems to be part of a plagioclase core region, which was partially resorbed and then included in a plagioclase aggregate. Therefore, for this crystal the early crystallized parts have higher 87Sr/86Sr_i than the later crystallized ones. Sample 19 M-4 shows a significant core-rim increase of ⁸⁷Sr/⁸⁶Sr_i, while the opposite is apparent for Plag-A of GUJ19-1, which has a rim with relatively low $^{87}\text{Sr}/^{86}\text{Sr}_{i}$ indistinguishable from the matrix composition. Plag-A of MAL19-6 shows also a rimward decrease of 87 Sr/86 Sr; however, for this plagioclase crystal the rim isotopic composition is significantly lower than that of the matrix.

Clinopyroxene, olivine, and Fe-Ti oxides

Clinopyroxene and olivine were analyzed in a few samples as these crystals are rare and generally small ($<400 \mu m$). Clinopyroxene and olivine compositions are reported in the Electronic Appendix 2, Supplementary Table S5 and Table S6. Clinopyroxene was measured in 10 samples where it occurs as monocrysts (e.g. single crystals surrounded by the groundmass), glomerocrystic clots, or as inclusions in plagioclase megacrysts (cf., Figs 3a and 2f, respectively).

Clinopyroxenes are augite to pigeonite (Fig. 11). The low-Ca clinopyroxene is present in half of the samples and usually occurs as microcrysts or groundmass crystals. In some samples (e.g. GUJ19-1, KAS15-3) clinopyroxene inclusions in plagioclase megacrysts tend to be enriched in Fe compared with the other analyzed crystals, i.e. these two groups of clinopyroxenes are not in equilibrium.

The augitic crystals have quite variable compositions (Fig. 12) with Mg# varying from 82 to 40 (Mg# = 100 (Mg/(Mg + Fe $^{2+}$), where Fe²⁺ is calculated based on stoichiometry; Papike et al., 1974). The highest Mg# is observed in augites from samples GUJ19-2 (Mg# c. 80), while the lowest is those of augite inclusions in large plagioclase from MAL19-4 (Mg# c. 50) and in phenocrysts or microcrysts from GUJ19-5 (Mg# c. 40-50). The variable Mg# of the augites is not correlated with that of the host rocks, which all yield similar Mg# (41–45). In particular, GUJ19-2 augites are Mg-rich, even if this rock is fairly evolved. It should also be noted that some samples have relatively homogeneous clinopyroxene compositions (e.g. GUJ19-2; Fig. 12a, b), while others have strongly variable compositions (Fig. 12a-d). For example, samples 19 M-4, 19P-5, and GUJ19-1 have clinopyroxenes with significantly different TiO2 contents (e.g. in 19 M-4 TiO₂ varies from c. 1.0 to c. 2.5 wt%, at similar Mg#). A significant variability of augite compositions has been also observed between phenocrysts and augite included in plagioclase megacrysts in some samples (e.g. in 19P-5, MAL19-4, and GUJ19-1).

Most augite macro- or micro-crysts (maximum axis: >100 and <100 μ m, respectively) analyzed in detailed core-rim traverses (Fig. 12) show a clear drop of Mg# at the rim of the crystals in the contact with the groundmass (this is particularly strong in GUJ19-1). Only augites from GUJ19-2 are essentially unzoned in Mg#. In general, TiO2 is correlated with that of the matrix compositions,

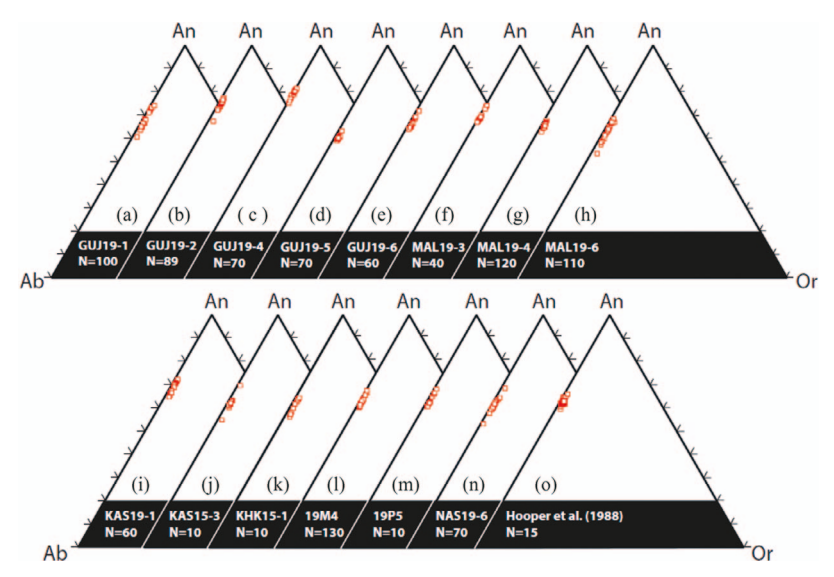


Fig. 7. Plagioclase triangular classification diagrams. An, anorthite; Ab, albite; Or, orthoclase. All components are in mol%. (o): giant plagioclase compositions from the WG (Hooper et al., 1988) are plotted for comparison.

being low in augites from GUJ19-2 (0.5 wt%) and in most of GUJ19-1 (c. 0.6-1.0 wt%), while it is high in GUJ19-6 (0.9-1.4 wt%) and MAL19-6 (0.9-1.9 wt%). One augite crystal from GUJ19-1 is zoned in TiO₂, with the central portion showing relatively high TiO₂ (c. 1.1 wt%). Similarly, a few microcrysts from GUJ19-1, included in plagioclase aggregates show high TiO₂ up to 1.4 wt% (Fig. 12e). The two MAL19-4 augites included in plagioclase megacrysts show markedly different compositions, for example in terms of Mg# (c. 50 vs c. 70) and TiO_2 (c. 0.8 vs c. 1.2 wt% for the two crystals).

Olivine crystals or their pseudomorphs larger than 100 μ m are present in about half the samples. Fresh olivine was detected and analyzed in four samples (MAL19-4, MAL19-6, KAS19-1, GUJ19-1; Fig. 12f). In general, the forsterite content (Fo, mol%) varies from 74 to 51 in all analyzed samples, except in MAL19-4 where it can be as low as 25. Of the analyzed olivine compositions, only the phenocryst core of KAS19-1 is in equilibrium with its host-rock assuming a mineral/melt K_D for (Fe/Mg) of 0.30 ± 0.03 (Roeder & Emslie, 1970). The relatively large olivine from KAS19-1 shows a constant core composition (c. Fo_{74}) and then a clear decrease to Fo₅₈ in the outermost c. 50 μ m. Olivine phenocrysts from MAL19-6 and MAL19-4 show Fo compositions of c. 61-51 and 71-59 and are significantly depleted in Mg/Fe compared with their whole rocks (Fig. 12; Table S6). On the contrary, the olivine included in large plagioclase crystals from MAL19-4 are slightly enriched in Mg/Fe compared with equilibrium conditions with the

Most analyzed Fe-Ti oxides are magnetite (Tables S7). Rare ilmenite has been found both as inclusions in plagioclase megacrysts and as microphenocrysts in MAL19-4, MAL19-5, and GUJ19-3.

EBSD data

EBSD data were obtained to determine if the optical deformation microstructures observed under the petrographic microscope are are due to crystal plasticity, as suggested by lobate boundaries separating parts with different optical extinction. A plagioclase clot from sample KAS19-1 (Plag-4) was selected as it shows clear undulatory extinction (Fig. 2h). Chemical traverses across the plagioclase grains constituting this aggregate show near-constant major element compositions, with An contents (c. 60-65 mol%)

comparable to those of other plagioclase crystals from this same rock (Fig. 8q).

The EBSD 'Texture Components' (TC) maps of Fig. 13 highlight the existence of internal microstructures within the plagioclase clot. Growth twins, with mostly straight boundaries and disorientations between neighbor grains >170° (Fig. 13 d), coexist along with lobate grain boundaries. This is consistent with deformation and recrystallization microstructures, traced by high angle grain boundaries (disorientation between neighbor grains >30°; see Fig. 13d) and by sub-grain boundaries (disorientation <10°), as well as by deformation twins, whose twin boundaries terminate with a cuspate along twin-, grain-, and sub-grain boundaries (definition of subgrain boundaries and grain boundaries as in Passchier & Trouw, 2005).

A chemical map (Fig. 14) was acquired by EDS-SEM analysis of the portion of deformed plagioclase of KAS19-1 where the abovementioned fracture evolved. The map shows that the fractures between plagioclase grains are filled by Mg-Fe-rich and Na-Alpoor material, which most likely is infiltrated basaltic magma.

DISCUSSION

Comparison with the WG lava flow compositions

The basalt compositions reported here are compared with those from the WG based on their geochemical composition. The comparison is mainly based on the isotopic compositions (Fig. 6), on trace element ratios, and on the discriminant functions (Fig. 15a, b) as defined by Mahoney et al. (2000). The latter have been widely used to assign Deccan basalt samples to WG lava flow formations, which show only subtle geochemical differences (e.g. Vanderkluysen et al., 2011 and references therein).

Several samples including KAS19-1, MAT14-2, and 19M-4 were obtained from the WG, i.e. their stratigraphic position is well known. KAS19-1 was sampled on top of the Jawhar formation (corresponding to the so-called Thalghat GPB; Beane et al., 1986). Its trace element ratios and contents as well as its Sr-Nd isotopic composition are consistent with lower Kalsubai affinity, but in particular its Pb isotopic composition overlaps Igatpuri rather than Jawhar basalt compositions (age-corrected data from Basu et al., 2020a). Interestingly, the Sr-Nd-Pb isotopic data of KAS19-1 are

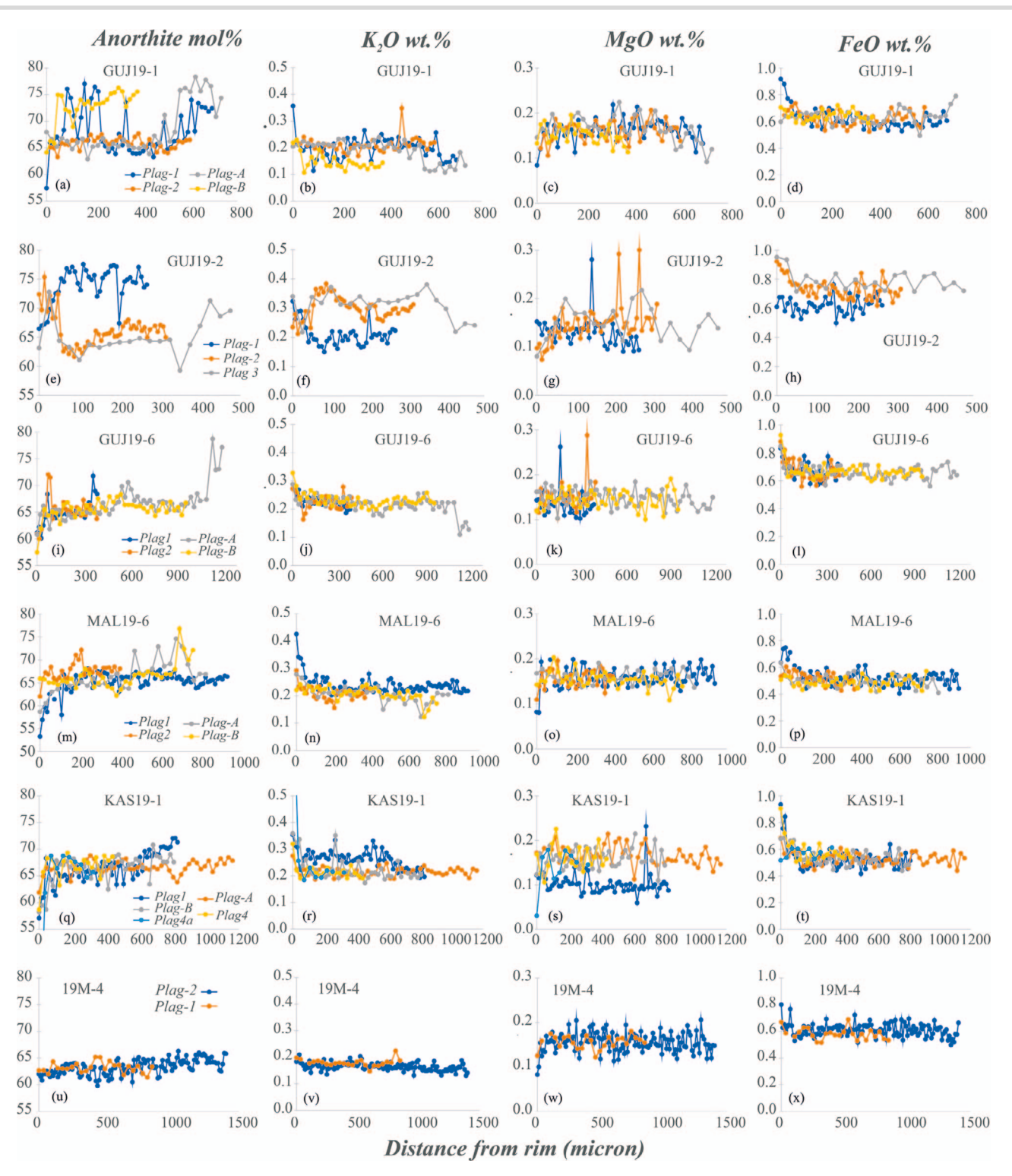


Fig. 8. Major and minor element core-rim variations of analyzed plagioclase, EMP data. Each point on the traverses represents an analysis point. Distance is in microns, Anorthite is defined as mol%. Occasionally, single analysis points may have been deleted when these were affected by altered zones or by micro-inclusions of other mineral species. For each sample 2–4 crystals were analyzed (shown by different symbols). Plag 4 and 4a from KAS19-1 were also analyzed by EBSD. The complete data set is reported in the Electronic Appendix 2, Tables S3.

significantly different (generally less enriched) than the isotopic data published in Peng et al. (1994) and Borges et al. (2014) for the same Thalghat GPB, implying that this GPB flow was formed from slightly distinct and not completely mixed magma batches. The Tunnel-5 sample MAT14-2 (GPB flow between the Neral and Thakurvadi fms.) has isotopic and trace element ratios similar to

those published by Beane et al. (1986) and Peng et al. (1994) for the same GPB. Its isotopic compositions overlap those of Thakurvadi (isotopic data from Basu et al., 2020a), but not of Neral basalts. Sample 19M-4 comes from high in the WG near the base of the Mahabaleshwar formation (Rajgad GPB; Shandilya et al., 2021) and has trace element and isotopic composition similar to those of

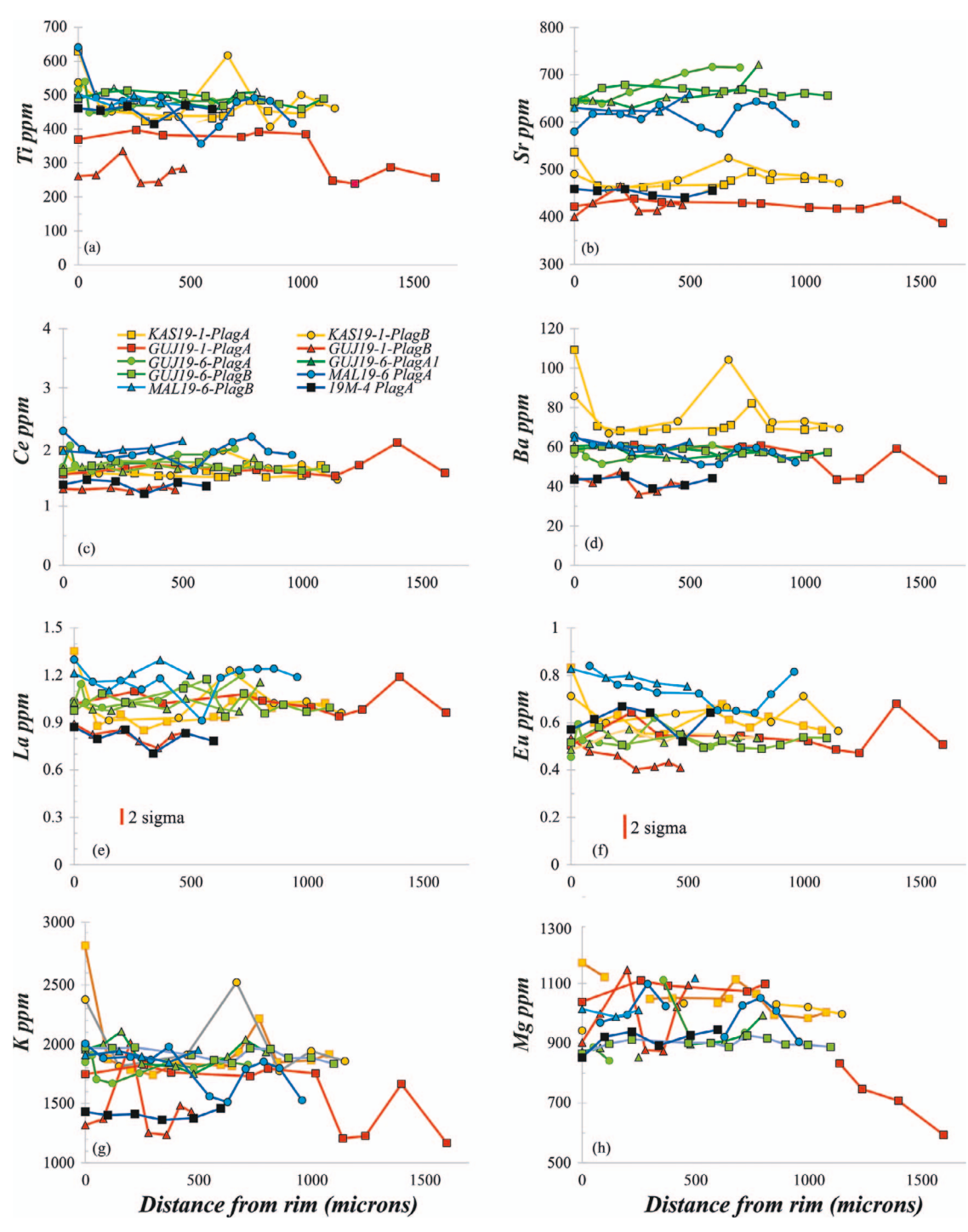


Fig. 9. Core-rim minor and trace element variations of plagioclase megacrysts, LA-ICP-MS data. Analytical uncertainties (2 sigma) are shown for La and Eu; for the other elements the uncertainty is smaller than the data symbol. Data are reported in the Electronic Appendix 2, Table S4. The Electronic Appendix 1, Supplementary Figures S2 and S3 show the analyzed plagioclase crystals and analysis spots.

Mahabaleshwar basalts, partially overlapping the Ambenali field (Figs 6 and 15). Notably, the composition of 19M-4 is quite different in terms of trace element ratios from that of sample 19P-5, which has been assigned to the same GPB flow field sampled at another locality (Shandilya et al., 2021).

Sample GUJ19-2 shows clear similarities with the Bushe chemical-type in terms of major and trace element compositions (Figs. 4, 5, 15). However, compared to the WG Bushe flows, GUJ19-2 shows slight differences, for example in Sr-Nd-Pb isotopic composition (Fig. 6) and slightly more enriched trace element ratios (e.g. Ba/Y; Fig. 15) as in other Saurashtra Bushe-like basalts (Melluso et al., 1995; Cucciniello et al., 2020).

Sample GUJ19-6 has major and trace element composition (Fig. 4, 5, 15) and Sr-Nd-Pb isotopic composition (Fig. 6), which overlap with the Ambenali and Mahabaleshwar basalts (Basu et al., 2020a) and the northern Deccan basalts (Peng & Mahoney, 1995; Peng et al., 1998). However, GUJ19-6 is enriched in U and Th $(U/La_N = 1.0)$ and depleted in Zr/Nb (6.5) compared with most WG Ambenali and Mahabaleshwar basalts (U/La_N < 1.0; Zr/Nb > 8), while its Ba/Y is similar to those of Mahabaleshwar

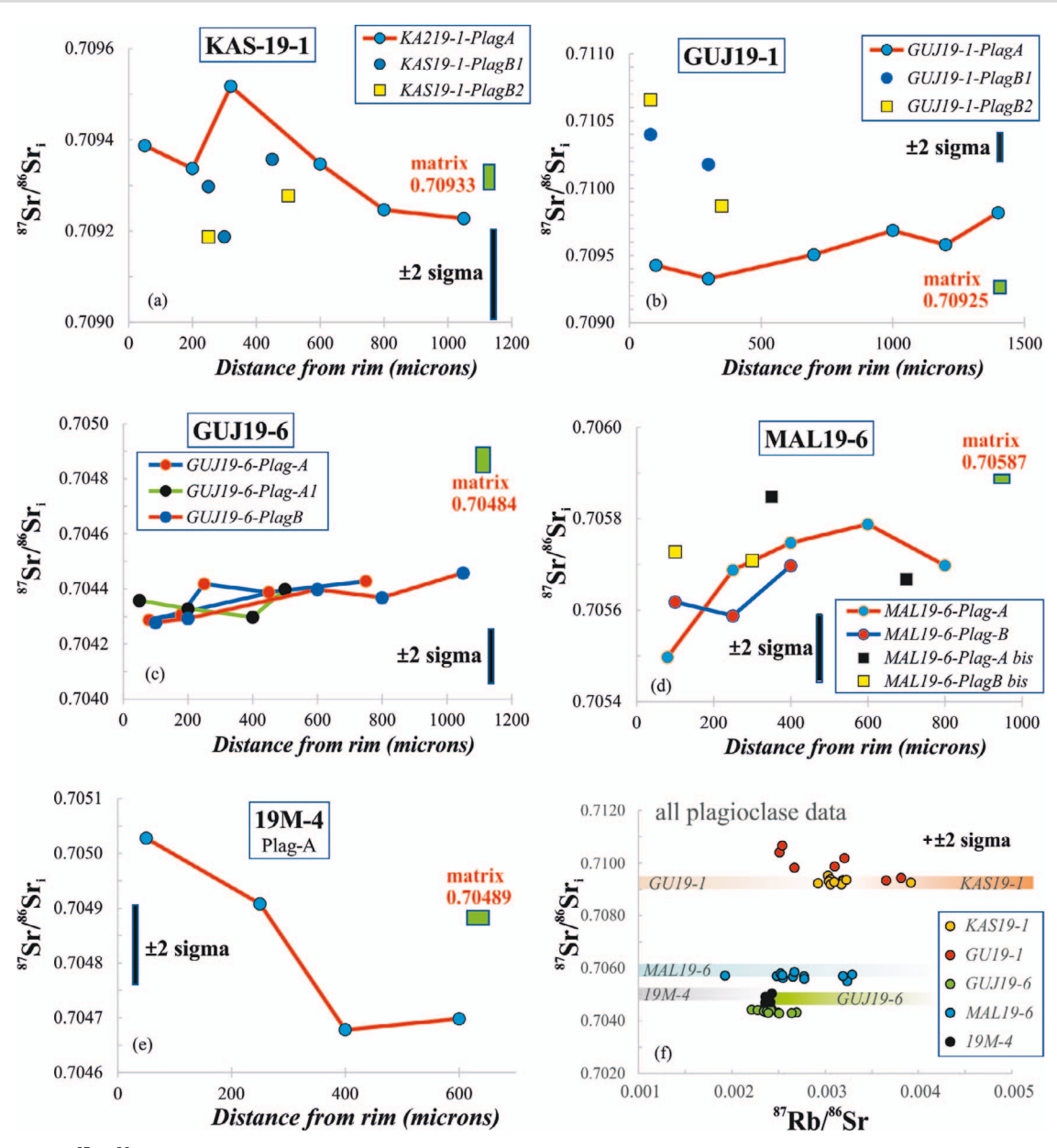


Fig. 10. (a-e) Initial 87 Sr/86 Sr isotopic copositions, recalculated to 66 Ma, of the plagioclase crystals analyzed by LA-ICP-MS (Table 4). Lines indicate successive analysis points obtained along a core-rim traverse. Other points are from other crystals of the same sample. The 2-sigma bars are average uncertainty values for each sample, but are quite consistent for all analyses (c. 0.0015-0.0020). Green box shows composition of matrix samples (bulk analysis), for which errors are less than 0.00002 (i.e. c. 10 times smaller than for laser spot data). Laser analysis spots have a diameter of 154 microns. The Electronic Appendix Fig.s S2 and S3 show the analyzed plagioclase crystals and analysis spots. (f) 87 Sr/86 Sr₁ vs 87 Rb/86 Sr of all analyzed plagioclase samples; bars indicate 87 Sr/86 Sr; of matrix (however, consider that 87 Rb/86 Sr of matrices is out of scale, being in the range 0.16-0.22).

but higher than for Ambenali basalts (Fig. 15). While it does not perfectly match with either Mahabaleshwar or Ambenali basalts, we can confidently compare the composition of GUJ19-6 to those of the basalts from the upper parts of the Wai subroup in general. A similar conclusion can be reached for GUJ19-4 and NAS19-6, despite lacking isotopic compositions for these samples, which hinders a precise comparison with WG formations. GUJ19-4 is characterized by a whole-rock and matrix REE pattern resembling that of an enriched MORB, with nearly flat intermediate to heavy REE chondrite-normalized values (Fig. 5). Such a pattern is not common in WG Deccan basalts. In the case of NAS19-6, sampled at the southeastern margin of the central Deccan plateau, an attribution to the Wai subgroup and probably the Mahabaleshwar

Fm. is consistent with its composition and with previous geochemical studies for this area (Jay & Widdowson, 2008; Wilson Mantilla et al., 2022). However, the 40 Ar/39 Ar age recently obtained for NAS19-6 (65.976 \pm 0.065 Ma; Wilson Mantilla et al., 2022) is substantially older than those of $^{40}\mathrm{Ar}/^{39}\mathrm{Ar}$ dated Mahabaleshwar basalts from the WG (65.521 \pm 0.065 to 65.422 \pm 0.103 Ma; Renne et al., 2015; Sprain et al., 2019).

GUJ19-1 and GUJ19-5 are similar to basalts from the Kalsubai subgroup in terms of trace element ratios (e.g. Zr/Nb, Nb/La), discriminant functions and isotopic compositions (available for GUJ19-1 only; Fig. 4, 5, 15). The best fit for GUJ19-1 is obtained with basalts from the Thakurvadi Fm., as it does not overlap the Jawhar-Igatpuri field nor the Neral basalt field, e.g. in Fig. 6 (isotopic compositions) and in Fig. 15.

Table 3: Rb-Sr isotopic compositions of the analyzed plagioclase megacrysts from samples KAS19-1, GUI19-1, GUI19-6, MAI,19-6, 19M-4

Sample	⁸⁷ Rb/ ⁸⁶ Sr	$\pm~{f 2}\sigma$	⁸⁷ Sr/ ⁸⁶ Sr	$\pm~{f 2}\sigma$	$^{87} \mathrm{Sr} / ^{86} \mathrm{Sr_i}$
KAS19-1					
KAS19-1-plgA-1	0.002924	3.60E-05	0.70923	0.00020	0.709227
KAS19-1-plgA-2	0.003918	8.30E-05	0.70925	0.00020	0.709246
KAS19-1-plgA-3	0.003187	3.70E-05	0.70935	0.00019	0.709347
KAS19-1-plgA-4	0.003030	3.70E-05	0.70952	0.00020	0.709517
KAS19-1-plgA-5	0.003200	4.30E-05	0.70934	0.00022	0.709337
KAS19-1-plgA-6	0.003055	3.70E-05	0.70939	0.00018	0.709387
KAS19-1-plgB-1	0.003173	9.40E-05	0.70919	0.00020	0.709187
KAS19-1-plgB-2	0.003226	5.30E-05	0.70936	0.00020	0.709357
KAS19-1-plgB-3	0.003040	1.30E-04	0.70930	0.00016	0.709297
KAS19-1-plgB-4	0.003057	4.00E-05	0.70919	0.00023	0.709187
KAS19-1-plgB-5	0.003096	4.20E-05	0.70928	0.00017	0.709277
GUJ19-1					
GUJ19-1-plAgA-1	0.002670	1.10E-04	0.70982	0.00021	0.709817
GUJ19-1-plAgA-2	0.043400	6.70E-03	0.70962	0.00022	0.709579
GUJ19-1-plAgA-3	0.015540	7.10E-04	0.70970	0.00020	0.709685
GUJ19-1-plAgA-4	0.005311	7.00E-05	0.70951	0.00019	0.709505
GUJ19-1-plAgA-5	0.003652	3.80E-05	0.70933	0.00020	0.709327
GUJ19-1-plAgA-6	0.003811	3.70E-05	0.70943	0.00017	0.709426
GUJ19-1-plg-B-1	0.003205	6.80E-05	0.71018	0.00022	0.710177
GUJ19-1-plg-B-2	0.003100	1.80E-04	0.70987	0.00020	0.709867
GUJ19-1-plg-B-3	0.002511	4.80E-05	0.71040	0.00021	0.710398
GUJ19-1-plg-B-4	0.002540	2.10E-04	0.71066	0.00020	0.710658
GUJ19-6	0.002310	2.102 01	0.7 1000	0.00020	0.7 10030
GUJ19-6-plg-A-2	0.002333	2.80E-05	0.70443	0.00014	0.704428
GUJ19-6-plg-A-3	0.002420	2.30E-05	0.70439	0.00014	0.704388
GUJ19-6-plg-A-4	0.002120	2.60E-05	0.70442	0.00011	0.704418
GUJ19-6-plg-A-5	0.002694	2.60E-05	0.70431	0.00013	0.704307
GUJ19-6-plg-A-6	0.002640	2.40E-05	0.70429	0.00013	0.704288
GUJ19-6-plg-A-1	0.002275	2.90E-05	0.70440	0.00016	0.704398
GUJ19-6-plg-A-7	0.002497	2.90E-05	0.70430	0.00010	0.704298
GUJ19-6-plg-A-8	0.002365	2.20E-05	0.70433	0.00012	0.704328
GUJ19-6-plg-A-9	0.002341	2.80E-05	0.70436	0.00011	0.704358
GUJ19-6-plg-R-1	0.002341	7.50E-05	0.70446	0.00012	0.704338
GUJ19-6-plg-B-2	0.002374	2.40E-05	0.70437	0.00011	0.704368
GUJ19-6-plg-B-3	0.002374	2.70E-05	0.70440	0.00013	0.704398
GUJ19-6-plg-B-4	0.002391	2.30E-05	0.70430	0.00011	0.704293
GUJ19-6-plg-B-5	0.002505	2.10E-05	0.70428	0.00010	0.704278
MAL19-6	0.002303	2.101 05	0.70120	0.00012	0.701270
MAL19-6-plg-A-1	0.002480	2.70E-05	0.70570	0.00016	0.705698
MAL19-6-plg-A-2	0.002522	2.80E-05	0.70579	0.00014	0.705788
MAL19-6-plg-A-3	0.002322	6.30E-05	0.70575	0.00014	0.705747
MAL19-6-plg-A-4	0.003288	2.20E-05	0.70569	0.00014	0.705687
MAL19-6-plg-A-5	0.002773	3.50E-05	0.70550	0.00013	0.705497
MAL19-6-plg-A-6	0.003233	3.30E-05	0.70567	0.00014	0.705437
MAL19-6-plg-A-7	0.002671	3.50E-05	0.70585	0.00012	0.705847
MAL19-6-plg-A-7	0.002671		0.70570		
MAL19-6-plag-B-2	0.003190	3.00E-04		0.00014	0.705697
MAL19-6-plag-B-2 MAL19-6-plag-B-3		2.20E-05 2.20E-05	0.70559	0.00015 0.00014	0.705587 0.705618
1 0	0.002548		0.70562		
MAL19-6-plag-B-1	0.001927	3.00E-05	0.70571	0.00015	0.705708
MAL19-6-plag-B-2	0.002541	2.40E-05	0.70573	0.00014	0.705728
19M-4	0.000410	E 60P 0F	0.70470	0.00019	0.704600
19M-4-plAg-A-1	0.002412	5.60E-05	0.70470	0.00018	0.704698
19M-4-plAg-A-2	0.002359	4.10E-05	0.70468	0.00015	0.704678
19M-4-plAg-A-3	0.002360	3.90E-05	0.70491	0.00016	0.704908
19M-4-plAg-A-4	0.002429	3.80E-05	0.70503	0.00017	0.705028

2-sigma analytical uncertainties are reported. Initial isotopic data $(^{87}Sr/^{86}Sr_i)$ are recalculated to 66 Ma.

The composition of samples from the Malwa Plateau MAL19-3, MA19-4, and MAL19-6 are difficult to assign to a specific WG chemical type. While Sr-Nd isotopic compositions of MAL19-3 and MAL19-6 are similar to those of the Poladpur formation, their Pb isotopic ratios are slightly higher than those of Wai basalts. Trace element compositions of these Malwa samples resemble those of Wai (for MAL19-3 and MAL19-6) or Lonavala (Khandala) basalts (for MAL19-4). In detail, MAL19-6 has low Zr/Nb and Ba/Y, which is compatible with Ambenali basalts (Fig. 15a) and it overlaps that formation also on the discriminant function diagram (Fig. 15b). Nonetheless, the isotopic compositions of MAL19-6 are significantly more enriched than those of Ambenali basalts.

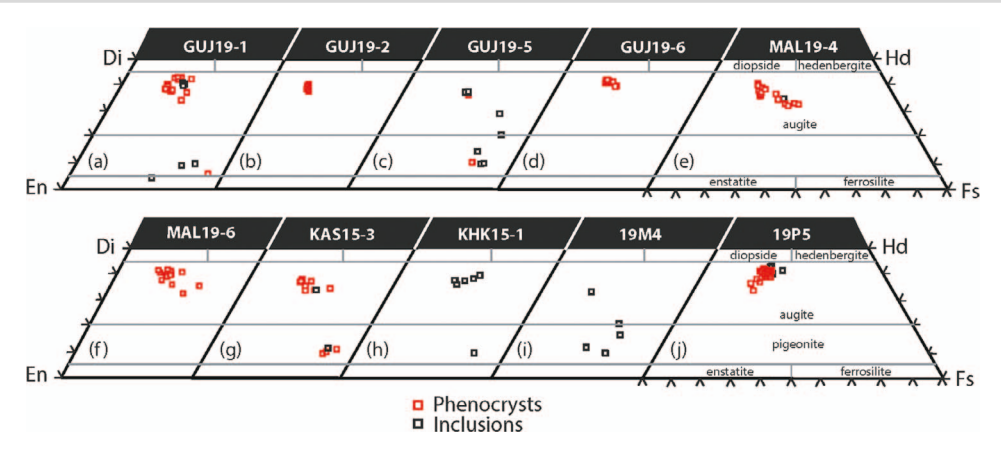


Fig. 11. Clinopyroxene triangular classification diagrams. En, enstatite; Di, diopside; Hd, hedembergite; Fs, ferrosilite. All components are in mol%.

A general conclusion that arises is that the compositions of the lava samples from the northern Deccan (Malwa, Saurashtra) studied herein only partially overlap those of WG lava flow formations. Subtle differences between northern vs. southern (e.g. WG) Deccan suggest a slight North-South change in mantle and crustal components. We also note that geochemical similarity does not necessarily imply a synchronous emplacement, which needs to be confirmed by geochronological data. For example, sample NAS19-6 shares geochemical characteristics of the Mahabaleshwar Fm., but has been shown (Wilson Mantilla et al., 2022) to be significantly older than this formation where it is defined in the WG (e.g. Sprain et al., 2019).

Magma differentiation

A general observation is that our samples are quite evolved, i.e. low in MgO (5.6-4.1 wt%) with only GUJ19-4 having MgO higher than 6.0 wt%. Such evolved compositions are not rare in the Deccan, and several formations are dominated by basalts with MgO in the range 6-4 wt%. Most of our samples are also rich in FeOt (12-15 wt%; except GUJ19-2), FeOt/MgO (2.0-5.9), and TiO₂ (2.2-3.5 wt%, except GUJ19-2 and GUJ19-4), as other evolved Deccan basalts (Beane et al., 1986; Basu et al., 2020a). However, our basalt whole-rock and, in particular, matrix compositions plot among the most Ti- and Fe-rich Deccan basalts. The Ti-enriched composition is further highlighted by multi-element diagrams (Fig. 5) in which both whole-rock and matrix (not shown) samples show a positive Ti anomaly for most samples (except GUJ19-2 and GUJ19-4), which is not common among most other Deccan basalts.

fO₂-T–P conditions and mineralogical constraints

Ilmenite-magnetite pairs were found only in MAL19-4 and MAL19-6. In the former sample, the oxides were re-equilibrated at subsolidus conditions as confirmed by reflected-light microscope observation, while in MAL19-6 they seem to be in mutual equilibrium (considering the Mg/Mn ratio of magnetite and ilmenite; Table S7, Electronic Appendix 2; Bacon & Hirschmann, 1988) and yield a temperature of 1030–1050°C and log fO_2 of -10.8 to -10.9corresponding to about 0.4 log units below the QFM buffer (using Sauerzapf et al., 2008).

The oxidation state can be further constrained by the minor and trace element content of the plagioclase crystals. Dygert et al. (2020) and Laubier et al. (2014) investigated the control of fO2 on the Eu and Fe plagioclase/basalt partition coefficients,

while Lundgaard & Tegner (2004) highlighted the importance of melt SiO₂ in controlling the D of Fe³⁺ and Fe²⁺. In order to be in equilibrium with the matrix, the relatively low Fe of the plagioclase cores would require Fe to be quite incompatible, a condition that is attained at low fO_2 (Fe³⁺ is less incompatible than Fe²⁺; Laubier et al., 2014). On the contrary, at moderate fO2 close to the QFM buffer, the melt in equilibrium with the plagioclase cores would be depleted in Fe compared with the matrix samples, but would still be similar to typical evolved Deccan basalts. The increasing Fe at the plagioclase rims would either suggest crystallization at progressively more oxidizing conditions (>QFM) or crystallization from a progressively more Ferich magma (e.g. Ruprecht & Wörner, 2007). On the other hand, the Eu partition coefficient increases at decreasing fO2 (Eu2+ is more compatible than Eu3+; Dygert et al., 2020). Therefore, Eu contents of the analyzed plagioclase would be in equilibrium with most Deccan magmas for a D calculated for QFM or QFM-1 conditions, while for QFM-2 or QFM+1 the calculated equilibrium melt would be different (lower and higher in Eu, respectively) from any Deccan basalt in terms of its Eu concentration (Electronic Appendix 1, Supplementary Fig. S4). In summary, the most likely interpretation of Fe and Eu contents, combined with the available oxide mineral compositions suggest that the analyzed plagioclase crystallized from a melt at QFM or QFM-1.

Clinopyroxene and olivine compositions can be used to calculate crystallization pressure and temperature (Neave & Putirka, 2017). The clinopyroxene-equilibrium melt geo-thermobarometer yields uncertainties of about 0.14 GPa and about 50°C (Neave & Putirka, 2017). For clinopyroxene phenocrysts, i.e. those crystals being in contact and in textural and chemical equilibrium with the matrix composition, calculated pressures are lower than 0.4 GPa (Fig. 16). The highest values, c. 0.3 GPa, are yielded by GUJ19-6, while GUJ19-1, GUJ19-2, and MAL19-6 yield pressures generally lower than 0.2 GPa. Clinopyroxene included in large plagioclase crystals gives <0.3 GPa in sample MAL19-4, and <0.2 GPa for sample MAL19-6 (calculated from clinopyroxene composition only, i.e. not considering an equilibrium magma). Calculated temperatures are about 1160-1130 °C in sample for GUJ19-6, about 1120-1100°C in GUJ19-2 and about 1140-1120°C for the other samples. Olivine temperatures (Putirka, 2008, equation 22) are about 1160°C in sample KAS19-1, while for the other samples olivine and matrix are not in equilibrium hindering application of the geothermometer. In conclusion, the analyzed samples dominantly evolved at low pressure (01–0.3 GPa) and moderate temperature (1170-1100°C).

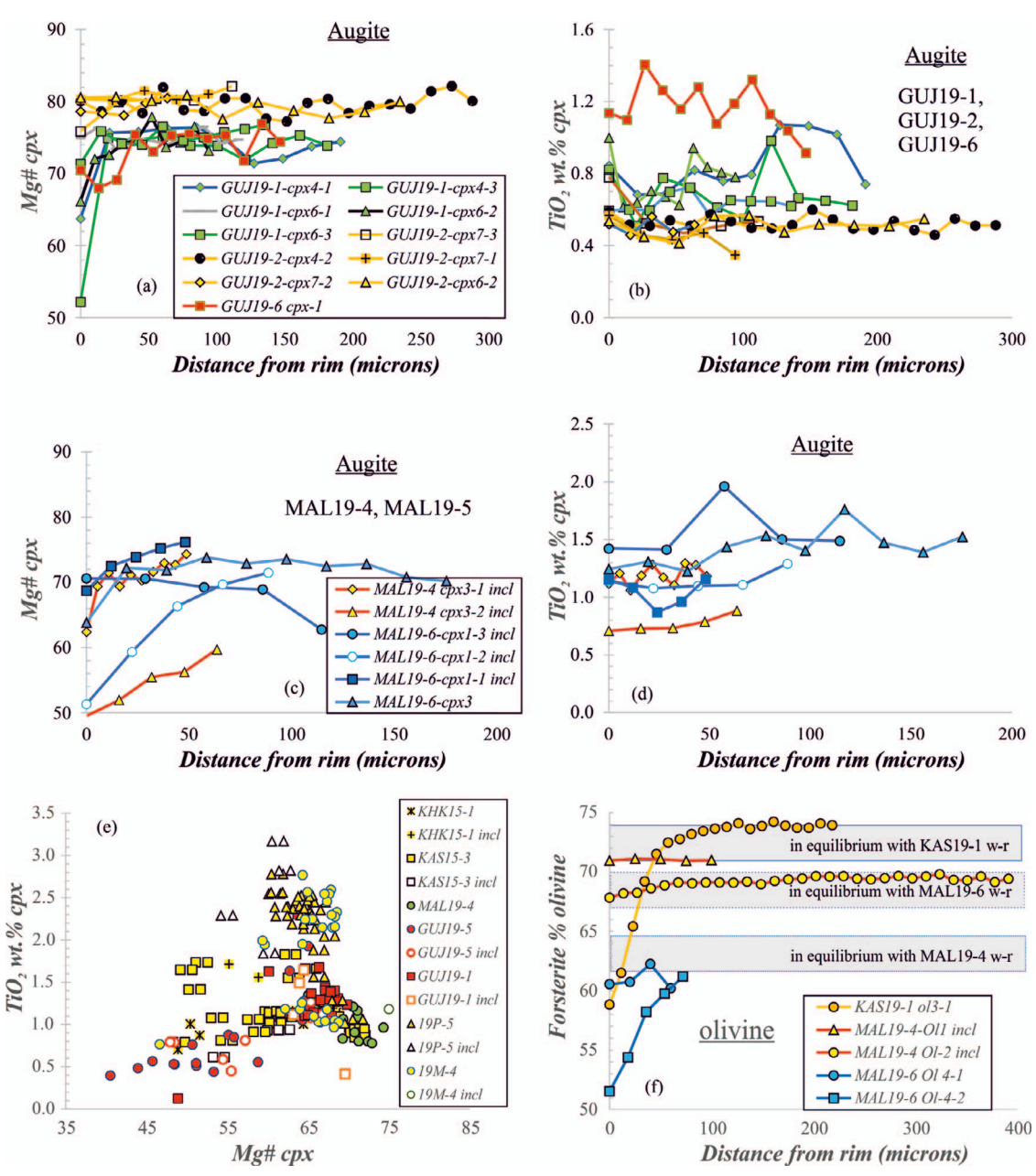


Fig. 12. Clinopyroxene and olivine compositions of the analyzed samples. (a-d) $Mg\# (= 100 (Mg/(Mg + Fe^{2+}), where Fe^{2+}) is calculated according to$ Papike et al. (1974) and TiO2 wt% core-rim traverses of augites from samples GUJ19-1, GUJ19-2, GUJ19-6 (a, b) and MAL19-4, MAL19-6 (c, d). All analyzed GUJ and MAL19-6 cpx3 clinopyroxenes are phenocrysts, while the remaining MAL clinopyroxenes are inclusions in plagioclase megacrysts. Augite data plotted in (a-d) and olivine data were obtained at the University of Milano. (e) Mg# vs TiO2 wt% for core and rim of augitic clinopyroxenes analyzed at the USGS. Incl = augite inclusion in plagioclase megacrysts. (f) Olivine core-rim traverses, forsterite contents (Fo = mol% Mg/(Mg + Fe); Milano University analyses). Olivine from KAS19-1 is part of a plagioclase-dominated crystal aggregate, but the olivine rim is at contact with the groundmass; olivine from MAL19-4 are inclusions in plagioclase megacrysts, while those from MAL19-6 are small phenocrysts. The rectangles show compositions in equilibrium with the whole rocks of KAS19-1, MAL19-6, and MAL19-4 assuming a mineral/melt KD for (Fe/Mg) of 0.30 ± 0.03 (Roeder & Emslie, 1970).

Closed-system differentiation and MELTS modeling

We tested the possible evolution of magma compositions with Rhyolite-MELTS (Gualda et al., 2012) considering equilibrium crystallization, low to intermediate pressure (0.1 and 0.5 GPa), dry or moderately hydrous conditions ($H_2O=0.5$ wt%), and low to moderate oxygen fugacity (fO₂ close to the COH and QFM buffers). These parameters were chosen based on the experimental and mineralogical studies on Deccan basalts (Sano et al., 2001; Gangpèhadayay et al., 2003; Melluso & Sethna, 2011) and on results discussed in the previous sections.

Starting from the whole-rock compositions, Rhyolite-MELTS equilibrium crystallization modeling indicates that for hydrous magmas and pressure higher than 0.1 GPa clinopyroxene or olivine crystallize along with plagioclase in about equal amounts, i.e. the calculated compositions fail to reproduce the observed mineralogy of the rocks. For low-pressure (0.1 GPa) and anhydrous conditions, the match between calculated and observed compositions improves. This is shown in Fig. 17 for the whole-rock composition of GUJ19-4. Rhyolite-MELTS modeling has been done starting from little evolved Deccan basalts with

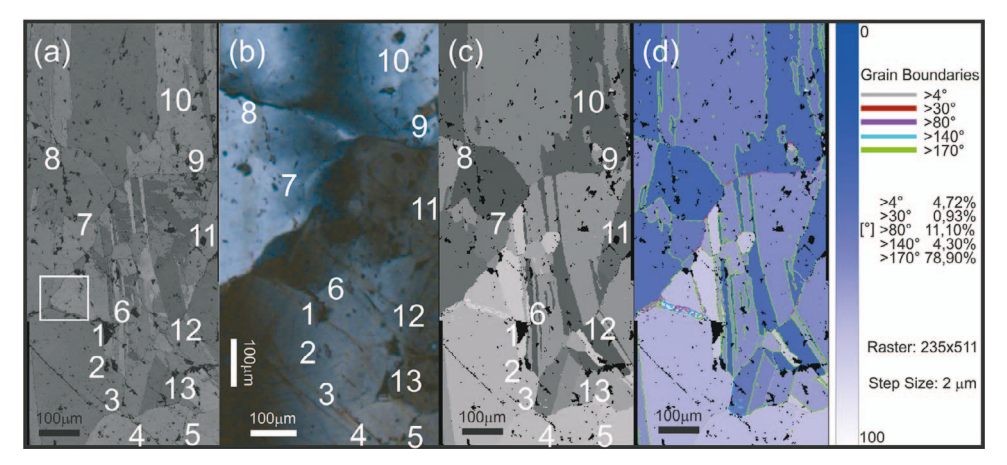


Fig. 13. EBSD maps and cross-polarized light image for sample KAS19-1. The white rectangle in Fig. 2h is the area $(470 \times 1022 \ \mu\text{m})$ mapped with EBSD (2 μm step size). (a) EBSD 'Band Contrast' map (BC-map). (b) Cross-polarized light (XPL) image. (c) EBSD 'Texture Components' map (TC-map) highlighting the microstructures of the plagioclase clots shown in Fig. 2h. (d) EBSD 'Texture Components' map defined by blue to white color shades reflecting the crystallographic disorientation of each pixel of the map within a 0° to 100° range from a chosen reference orientation (expressed in Euler angles). In (a), (b), and (c), numbered marker points are shown for a better comparison between the images, since a one-to-one comparison of XPL images and EBSD maps is not straightforward. XPL images are indeed influenced by the interference of light crossing a 30-µm-thick polished thin section, whereas EBSD maps gain their information just from the uppermost few nanometers of the same rockslide. An important impingement microstructure is preserved in the central part of the analyzed area (from No. 7) and in the lower part (from points 3 to 13), where twinned plagioclase crystals impinge with an un-twinned one and subgrain boundaries radiate (Fig. 13d). A noteworthy microstructure occurs in the lower left, where an about 16-µm-large bright zone extends from No. 1 toward the left border in the TC map (Fig. 13c). This area is characterized by a complex configuration of tangled boundaries (Fig. 13d).

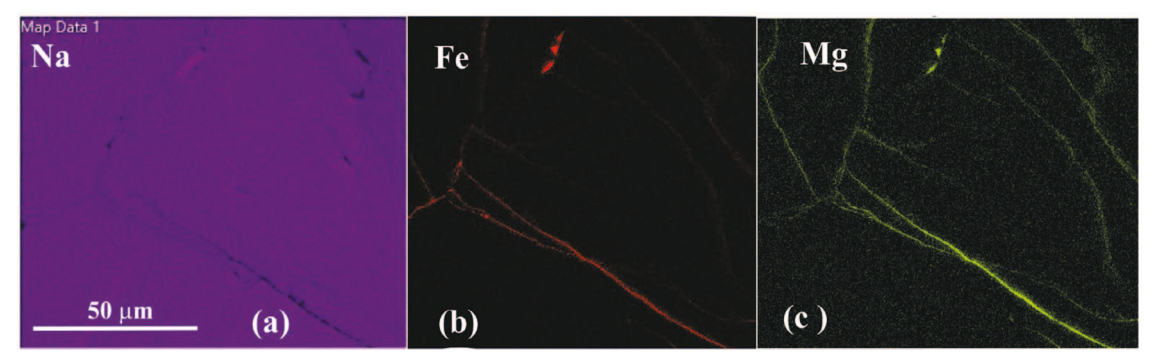


Fig. 14. Na, Fe, Mg chemical maps of a c. 100 × 100 micron area from the deformed plagioclase grains in KAS19-1 (see Fig. 13 for location of the map). The dark colors in (a), bright red in (b) and bright green-yellow in (c) mark low Na and high Fe-Mg areas along fractures, which are probably filled by matrix of basaltic composition.

about 8 and 12 wt% MgO in order to check if these would represent suitable parental magmas for the observed whole-rock and matrix compositions. The considered parental magmas are samples SAM011 and BOR036 from Beane et al. (1986), which respectively belong to the Igatpuri and Thakurvadi Formations (Kalsubai subgroup). The modeling was run at 0.1 and 0.5 GPa, 0, 0.5, 1.0 wt% H₂O, and with QFM- or COH-buffered or unbuffered fO₂. Starting from SAM011 the best fit with the observed matrix compositions (except for GUJ19-2 and GUJ19-4) is obtained for low P, QFM and anhydrous conditions. High-pressure (0.5 GPa) conditions yielded less satisfactory results. Starting from BOR036 (c. 12 wt% MgO), matrix compositions are reached both for low pressure (0.1 and 0.5 GPa), at QFM or unbuffered fO_2 , and anhydrous conditions. Starting from the BOR036 magma composition, after about 58% fractionation the evolved magmas reach up to 16-18 wt% FeOt, similar to the matrix compositions. Such calculated evolved melts would be in equilibrium with plagioclase (An₆₁) similar to most observed rim compositions. Fractionated minerals are olivine (8 wt%), clinopyroxene (30 wt%) and plagioclase (19 wt%, average An_{68}).

An important conclusion that can be drawn from MELTS modeling is that only dry and low-pressure conditions are compatible with the observed compositions (Fig. 18). Hydrous conditions and high pressure would delay plagioclase saturation, favoring instead mafic minerals, and would slightly reduce the density of the calculated melts. Considering SAM011 and BOR036 as starting melt compositions, at 0.1 GPa the density of evolved melts similar to the matrix compositions ranges between 2.64 and 2.61 g/cm³ for hydrous conditions, while it would range from 2.76 to 2.79 g/cm³ for dry conditions (density values calculated with Rhyolite-MELTS). At the same low pressure, the density of a plagioclase with An₇₅₋₆₀ composition ranges from 2.67 to 2.64 g/cm³. It should be considered that melt densities calculated with Rhyolite-MELTS are about 2% higher than those obtained in a recent experimental study (Krättli & Schmidt, 2021). Accounting for this correction, plagioclase is clearly buoyant in dry, low pressure, Fe-rich (FeO > 15 wt%) melts (melt minus plagioclase densities are >0.10 g/cm³). Considering that the melt density is largely controlled by the melt Fe content, it is interesting to notice that very Fe-rich samples (e.g. MAL19-4, KAS19-1) are also very rich

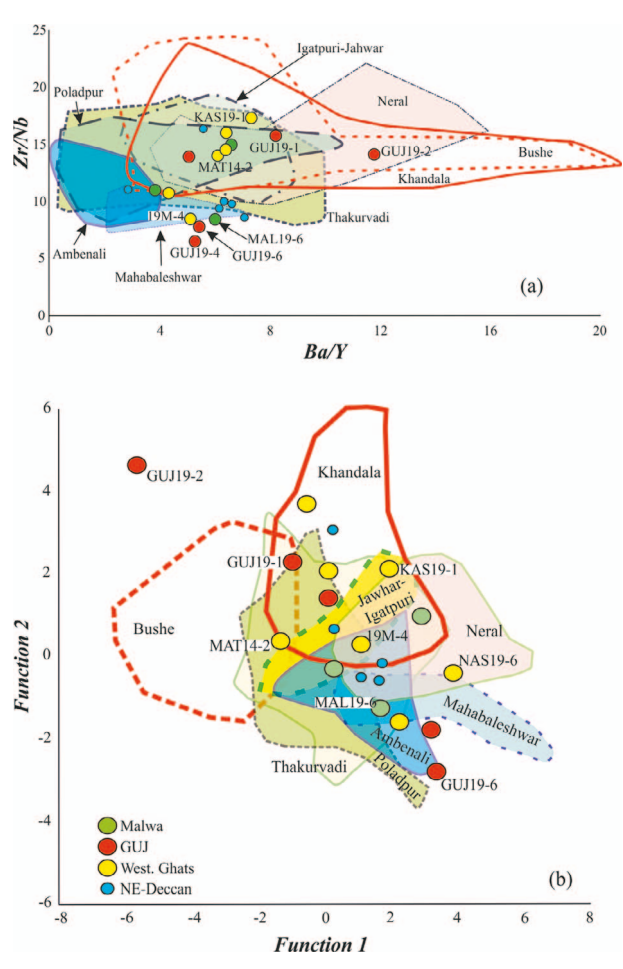


Fig. 15. Ba/Y vs Zr/Nb (b) and discriminant function diagram of the analyzed basaltic whole rocks. The fields for WG Deccan formations are from Vanderkluysen et al. (2011) and references therein. Discriminant functions are defined as in Mahoney et al. (2000): Function 1 = -0.48 $SiO_2 - 0.155Al_2O_3 + 1.289 \ TiO_2 + 0.157 \ CaO + 0.097 \ K_2O + 1.397$ $P_2O_5 - 0.048 \text{ Ni} + 0.462 \text{ Ba} + 0.301 \text{Sr} - 1.707 \text{ Zr} - 0.744 \text{ Y} - 0.002 \text{ Nb};$ Function $2 = 0.145 \text{ SiO}_2 + 0.135 \text{ Al}_2\text{O}_3 - 0.141 \text{ TiO}_2 - 0.251 \text{ CaO} - 0.286$ $K_2O + 0.439 P_2O_5 + 0.058 Ni + 0.953 Ba - 0.247 Sr + 0.815 Zr + 0.039$ Y - 1.215 Nb.

in plagioclase megacrysts (up to c. 15-20%). On the other hand, the quite evolved and relatively low-Fe sample GUJ19-2 yields a relatively low calculated density (c. 2.69 g/cm³ with Rhyolite-MELTS, or c. 2.64 g/cm³ considering Krättli & Schmidt, 2021) close to that of plagioclase. Although this sample is rich in plagioclase crystals (c. 9 vol%), all its plagioclase crystals are relatively small (<1 mm).

Deformed plagioclase megacrysts from crystal

Plagioclase deformation

Plagioclase deformation features include high angle lobate grain boundaries (Fig. 13) that point to impingement of different plagioclase crystals into one another. The microstructures shown in Fig. 13 suggest that impingement was accommodated not only by crystal plasticity (formation of subgrain and high angle grain boundaries), but also by fracture formation. Such fracturing must have been localized along pre-existing twin boundaries and became progressively dissected into fragments, rotating up to disorientations of 80–90° (red boundaries). Fractures are probably filled by basaltic melt as suggested by the chemical map (Fig. 14).

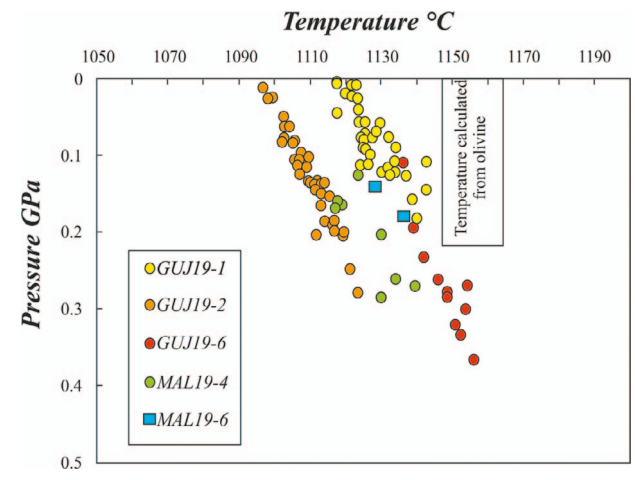


Fig. 16. Clinopyroxene crystallization pressure (GPa) and temperature (°C) calculated after Neave & Putirka (2017). Plotted data refer to clinopyroxene composition in chemical equilibrium with the matrix composition considered as representative of the equilibrium melt (Neave & Putirka, 2017). Note that uncertainties in temperature (±28°C) and pressure (c. ±0.1 GPa; Neave & Putirka, 2017) are quite large. Plotted data refer to clinopyroxene composition in chemical equilibrium with the matrix composition considered as representative of the equilibrium melt (criteria for equilibrium as defined in Neave & Putirka, 2017). The vertical rectangle shows the temperature calculated from the olivine composition of KAS19-1 (Figs 3b and 11f), which is close to chemical equilibrium with its whole rock and matrix (temperature calculated after Putirka, 2008, equation 22).

The disorientation angle distribution between neighbor pairs (Fig. 19) calculated for the EBSD map shows that the data are clustered and depart from a random distribution. The largest cluster forms disorientation angles between 170° and 180° and is related to twin boundaries of Albite-, Carlsbad-, and Albite-Carlsbad twins in the analyzed plagioclase clot (see also Electronic Appendix 1, Figs S5, S6, S7). A second cluster with low disorientation angles (<30°) relates to a deformation process characterized by recovery and recrystallization during impingement (Passchier & Trouw, 2005). The cluster defined by disorientations between 80° and 90° probably refers to the opening and sealing of the above-mentioned fracture (Fig. 13), which also happened during plagioclase impingement.

A major implication of the EBSD data (Figs 13 and 19) is that impingement occurred at high temperature causing slip along the <100> (001) system with simultaneous fracturing. Fracture formation during ductile deformation has also been shown in high strain rate torsion experiments by Rybacki et al. (2008, 2010), who deformed anorthite aggregates at 1100°C and 400 MPa. Cavities nucleate mostly at grain triple junctions and along grain boundaries and coalesce to micro-fissures, micro-fractures and shear bands under such deformation conditions (e.g. Spiess et al., 2012). These dynamically evolving microstructural sites are associated with pressure drops that cause melt infiltration from the surroundings. This would explain healing of the fracture in the impinged plagioclase agglomerate and the presence of basaltic matrix between the deformed plagioclase grains (Fig. 14). Notably, other samples contain plagioclase clots, which show textures similar to the analyzed Plag-4 clot from KAS19-1, for example, Plag-2 from GUJ19-6 (Fig. 2d) as well as crystal from GUJ19-1 and GUJ19-4 (not shown). The plagioclase clot from GUJ91-2 (Fig. 2i) also shows evidence of recrystallization during deformation.

High-temperature deformation in the presence of melt suggests that the plagioclase clots from several samples probably

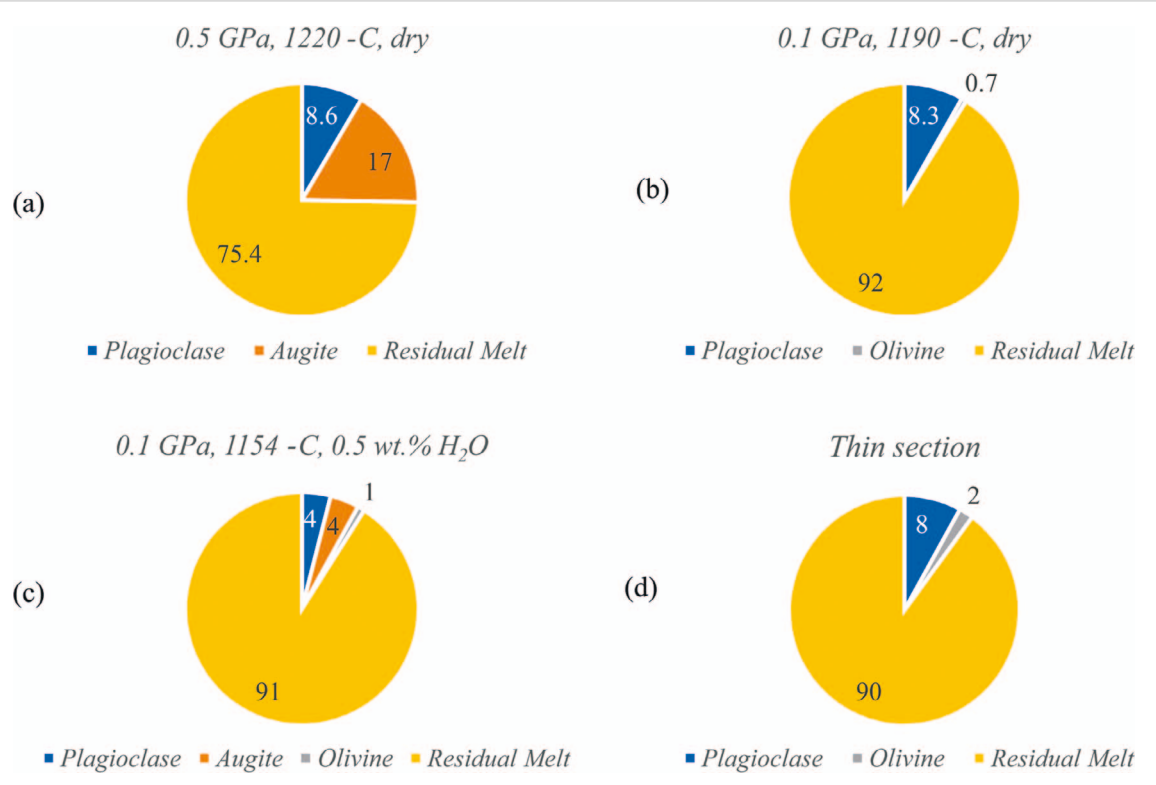


Fig. 17. (a-c) Crystallized mineral phases and residual melt wt% obtained from of Rhyolite-MELTS modeling (Gualda et al., 2012) starting from the whole-rock composition of GUJ19-4 and considering crystallization at equilibrium. Reported are the results for 0.5 and 0.1 GPa pressure, for dry or slightly hydrated conditions. All models done for QFM-buffered fO2. (d) Modal analysis of the thin section of GU19-4.

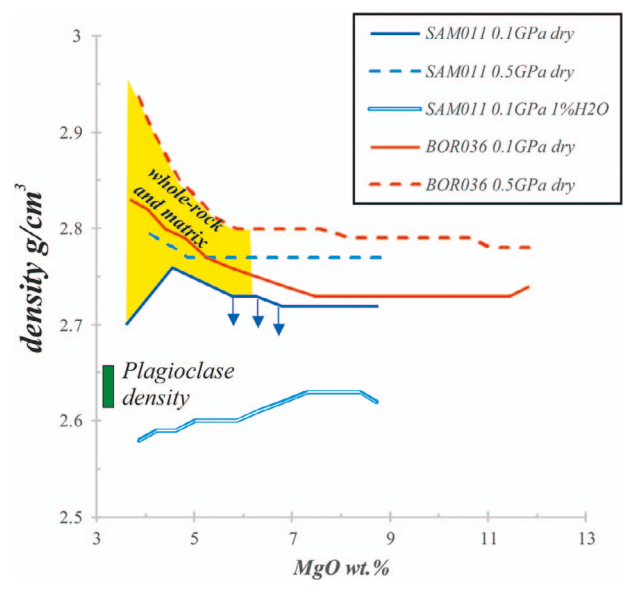


Fig. 18. MgO vs. melt density (g/cm³) as calculated with Rhyolite-MELTS (Gualda et al., 2012) starting from the same magmas as in Fig. 4, at 0.1 and 0.5 GPa, dry and hydrous conditions. The green rectangle shows the density of plagioclase, which ranges from c. 2.65 to 2.62 g/cm3 for An₇₀₋₆₀. The yellow field shows MgO and density calculated for whole rocks and matrices. Note that following Krättli & Schmidt (2021) melt densities would be 2% lower than calculated by Rhyolite-MELTS, cf. blue arrows.

originated in a crystal mush. Melt-assisted dislocation creep is the most likely process and is compatible with a viscous crystalline mush, with some interstitial melt between the plagioclase crystals (Sparks et al., 2019). Dislocation creep has been documented in

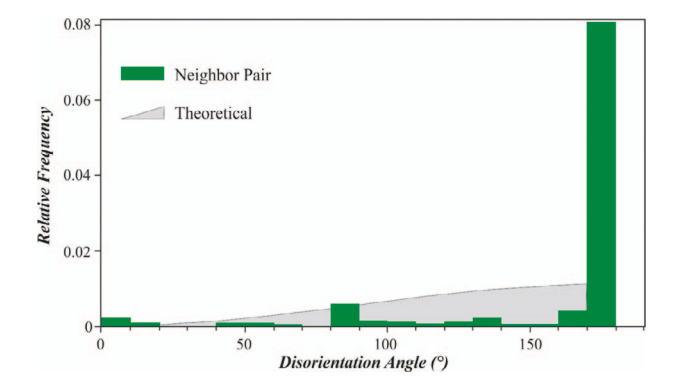


Fig. 19. The disorientation angle distribution between neighbor pairs calculated for the EBSD map of the plagioclase from KAS19-1. The histogram shows that data are clustered and depart from a random orientation (gray line). The largest cluster between 170° and 180° is related to twin boundaries; the cluster between 80° and 90° refers to the data next to the fracture to the left of point #1 (Fig. 2). Low disorientation angles (<30°) and disorientation angles 120-130° relate to deformation, recovery and recrystallization processes during impingement.

large mafic intrusions like the Bushveld or Skaergaard (Holness et al., 2017, 2022), but never, to our knowledge, in volcanic rocks from LIPs. The differential stress necessary to deform plagioclase crystals from a crystal mush is lower than that required to deform plagioclase in gabbros (which is c. 10-20 MPa) and could be provided by arrival of new hot magma rising from the deeper crust and fluxing the crystalline mush (Spiess et al., 2017). The fracture recognized in the plagioclase clot analyzed here could suggest high rates of deformation related to rapid magma ascent through a pre-existing crystal mush (Sparks et al., 2019). If this latter hypothesis is correct, it suggests that deformation of the analyzed plagioclase occurred during rise of new magma into the shallow-crust crystal mush, either during a replenishing event of the shallow plumbing system, and/or shortly before eruption of the magma.

(Dis-)equilibrium between plagioclase and magmas

Plagioclase crystallized in equilibrium with anhydrous or H2Opoor magmas should have the An content close to the Ca# (= Ca/(Ca + Na)) of the equilibrium melt since the $K_D(Ca/Na)$ is about 1.0 (Kohut & Nielsen, 2003; Feig et al., 2006). We found that the Ca# of whole rock and matrix are similar to the An of most plagioclase crystals zones. The range of An contents never exceeds 20 mol% in all analyzed plagioclase crystals, suggesting that the plumbing system of the analyzed lava flows was formed by relatively uniform, similarly evolved magmas. This is in accord with the data from augite and olivine, which are typically low in Mg/Fe, and with the rather uniform major element composition of Deccan basalts, in particular the low-MgO samples studied here. Such homogeneous compositions point to an efficient homogenization of the magmas in large magma chambers (Ernst et al., 2019). However, a detailed look at minor and trace element contents and Sr isotopic compositions of the plagioclase megacrysts of many samples suggests a more dynamic and complex scenario, which we will discuss below.

Four samples (MAL19-6, GUJ19-1, GUJ19-2, GUJ19-6) show rounded, partially resorbed high-An cores (c. An₇₅), which are quite different from their rim compositions, which are in equilibrium with the matrix. Such high-An cores may reflect crystallization from significantly more primitive (with higher Ca/Na) or more hydrous melt (as An increases with H2O; Feig et al., 2006) compared with the melt in equilibrium with the low-An

The plagioclase Mg, Sr, Ba, and REE (La, Ce, Eu) concentrations (EMP and ICP-MS data) are at or close to equilibrium with wholerock and matrix compositions for most samples. The only exceptions are one plagioclase of KAS19-1 significantly depleted in MgO, the high-An plagioclase of GUJ19-1, which is significantly depleted in Ba and REE, and the high-An plagioclase core of GUJ19-6, which is enriched in Sr and depleted in REE compared with equilibrium compositions.

The K and Fe equilibrium between plagioclase (EMP and ICP-MS data) and matrix or whole rock is observed only for about half the analyzed samples (NAS19-6, MAL19-3, GUJ19-4, GUJ19-5, 19M-4). In contrast, the equilibrium melts for the analyzed plagioclase crystals of GUJ19-6 and MAL19-6 and for one (of 4) crystals of KAS19-1 are enriched in K compared to the matrix. High-An plagioclase cores of GUJ19-1 and GUJ19-2 are significantly depleted in K. Such differences are only partially explained by a major element dependence of the partition coefficients for K in plagioclase (see next section). For Fe, equilibrium melts calculated from the plagioclase cores of GUJ19-1, MAL19-6, and KAS19-1 are depleted in Fe compared with the matrix and whole rock. Notably, the high-Fe contents observed in many plagioclase crystal rims from most samples would require an equilibrium melt slightly more Fe enriched than whole rock and matrix, at least considering the D_{Fe} of 0.045 that we used. However, as the Fe partitioning depends also on the plagioclase and melt composition (cf. Lundgaard & Tegner, 2004) the D_{Fe} may be lower for evolved melts and An-poor plagioclase, pointing to a possible equilibrium between the matrix and the crystal rims.

While EMP data for Ti in plagioclase are scattered, ICP-MS Ti data are much less so and indicate significant disequilibrium for

the samples GUJ19-6, MAL19-6, 19M-4 and for the high-An plagioclase of GUJ19-1. For all these plagioclase crystals, the matrix and whole-rock contain almost double the Ti compared with the equilibrium melts calculated from plagioclase core compositions for D = 0.04 (Fig. 4c). This discrepancy is probably not related to the considered Ti partition coefficient, as this value is consistent with several experimental studies (Bindeman et al., 1998; Bédard, 2006; Aigner-Torres et al., 2007; Tepley et al., 2010; Laubier et al., 2014; Sun et al., 2017). On the contrary, it suggests that several plagioclase crystals were in equilibrium with relatively low-Ti melts compared with the whole rock and in particular to the generally Ti-rich matrix.

 $^{87}\text{Sr}/^{86}\text{Sr}_{i}$ of most plagioclase crystals is generally similar to that of the respective matrix compositions (Fig. 10f). Nonetheless, the high-An plagioclase of GUJ19-1 has significantly higher ⁸⁷Sr/⁸⁶Sr_i than its matrix, while the plagioclase crystals of GUJ19-6 and most plagioclase analyses of MAL19-6 are significantly depleted in ⁸⁷Sr/⁸⁶Sr_i compared with their matrix (Fig. 10). Three of the five analyzed samples show 87 Sr/86 Sr_i variations from core to rim or among distinct crystals, which significantly exceed the analytical uncertainty and indicate a hybrid origin for at least some of the studied GPB basalts.

In summary, chemical disequilibrium between plagioclase and matrix or whole-rock compositions is observed for about half the investigated samples. Those showing the strongest disequilibrium for most elements and for 87 Sr/86 Sr; are the three samples containing high-An cores, i.e. GUJ19-1, GUJ19-6, and MAL19-6.

Some constraints on melt compositions and residence times

The range of Sr isotopic composition and trace element zoning of the plagioclase megacrysts reflects a combination of crystal growth and diffusive equilibration with a range of melt compositions. It is not straightforward to separate the two effects, because trace element partitioning depends on An content and temperature (e.g. Bindeman et al., 1998), and the diffusive reequilibration of several elements can occur on timescales of years to centuries (e.g. Costa et al., 2003; Zellmer et al., 2003; Costa, 2021). Thus, the trace element zoning of the plagioclase that we report is a combination of crystallization and diffusion that it is hard to deconvolve with the types of analytical data that we have collected. Nonetheless, we have assessed the likely range of compositions of the melt and degrees of equilibration for some elements with different diffusivities and partitioning relations, and used the Sr isotope zoning to provide maximum residence times at a given temperature.

The variation of An with minor and trace elements in our crystals is complex, but K and Mg show a distinct behavior. Mg is poorly zoned in most crystals, including for example the lowand high-An plagioclase from GUJ19-1, GUJ19-2, GUJ19-6, and MAL19-6 perhaps pointing to an almost complete re-equilibration of this element. The only exception is Plag-1 in KAS19-1 (Fig. 8s). On the contrary, K shows a significant correlation with the An content, which may in part be due to the dependence on An of the K partition coefficient (e.g. Bindeman et al., 1998). In GUJ19-1, GUJ19-6, and MAL19-6 the differences in K content from highand low-An plagioclase may be almost entirely due to a significant increase in the partition coefficient from An₇₅ to An₆₀ plagioclase (Bindeman et al., 1998). For example, in GUJ19-1 (Fig. 8a, b), lowand high-An crystals may all be in equilibrium with a magma having c. 1.5–2.0 wt% K₂O. On the contrary, low- and high-An crystals of GUJ19-2 yield strongly different K₂O (Fig. 8e, f), which may be only partially explained by a change in the partition coefficient. We found that the low- and high-An plagioclase cores of GUJ19-2 would be in equilibrium with a magma having c. 3 and c. 2 wt% K2O, respectively. Using the partition coefficient parametrization of Sun et al. (2017), the difference would be even larger (1.0 vs 2.5 wt% K₂O in the equilibrium magma, respectively). Therefore, in this case we expect that high- and low-K plagioclase crystals from GUJ19-2 were entrained by the same magma a short time before the eruption (see below). In KAS19-1, the An contents of all analyzed crystals are similar (except for a high-An core). Nonetheless, one crystal shows significantly higher K and lower Mg than the others (Fig. 8r, s) and neither K nor Mg seem equilibrated, pointing to very short residence times.

Constraints on timescales

Diffusion modeling of plagioclase megacrysts from Deccan GPBs (Borges et al., 2014) suggests that significant Sr isotopic corerim zoning are compatible with residence times of a few centuries (200-700 years). Here, we did not attempt detailed diffusion modeling since our LA-ICP-MS isotopic and trace element data are not detailed enough. Moreover, the presence of deformation features of the plagioclase implies that re-equilibration would not only occur simply by volume diffusion, but also via grain boundary diffusion (Dohmen & Milke, 2010), a process that is much more difficult to model. Thus, we have instead calculated the time that it would take to equilibrate a plagioclase crystal in three dimensions and obtained the maximum time of residence at a given temperature and plagioclase composition (Fig. 20). The observation of the zoning in trace elements and Sr isotopes would thus indicate that the residence times should be less than those required to reach a high percentage of equilibration (e.g. 90%). We find that the ⁸⁷Sr/⁸⁶Sr zoning observed in several of the plagioclase crystals analyzed here would suggest maximum residence times of about 1-8 centuries, depending on the temperature (1100°C-1000°C). For Mg and K complete equilibration could occur much earlier, in a few years to a few decades. It is worth emphasizing that these calculations are maximum residence times at the calculated temperatures and that models are for a fixed composition at the boundary. This means that if for example Mg and K concentration of the liquid changed over time faster than that of the Sr isotopes, it is possible that some processes recorded by Mg and K occurred a few years before eruption. This is consistent with the zoned olivine profile of sample KAS19-1 (Fig. 12f). This was modeled for Fe-Mg diffusion and yielded maximum residence times of about 5 years (Electronic Appendix 1, Fig. S8).

Thus, these estimations of timescales indicate that mixing of distinct magma batches occurred a few years to a few centuries before eruption, attesting to quite rapidly evolving magmatic systems. This is consistent with Deccan and LIP lava flow fields in general erupting as relatively short-lived pulses, each lasting a few centuries (Knight et al., 2004; Chenet et al., 2008).

A CONCEPTUAL MODEL FOR THE ORIGIN OF PLAGIOCLASE-RICH MAGMA

Textural and EBSD analyses indicate that at least part of the plagioclase megacrysts we studied were formed in crystal mushes (Fig. 21). The strong oscillatory zoning of several large plagioclase crystals (e.g. in 19 M-4) may reflect degassing pulses and consequent undercooling in a dynamic system being at least partially surrounded by magma (cf. Higgins & Chandrasekharam, 2007). However, several plagioclase crystals lack oscillatory zoning and some others show petrographic or EBSD evidence of deformation that point to residence in a relatively melt-poor, highly viscous

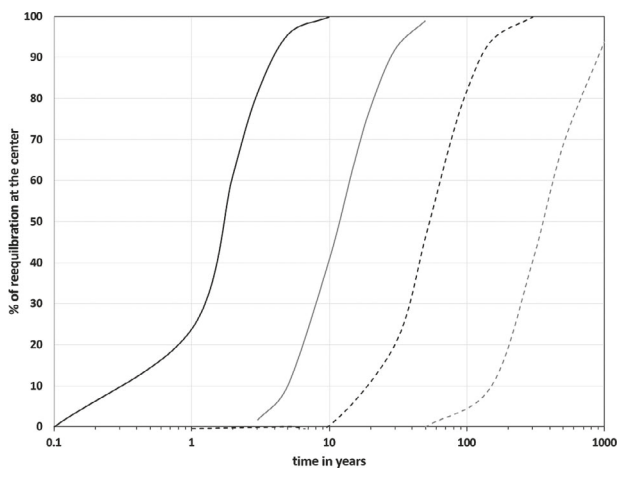
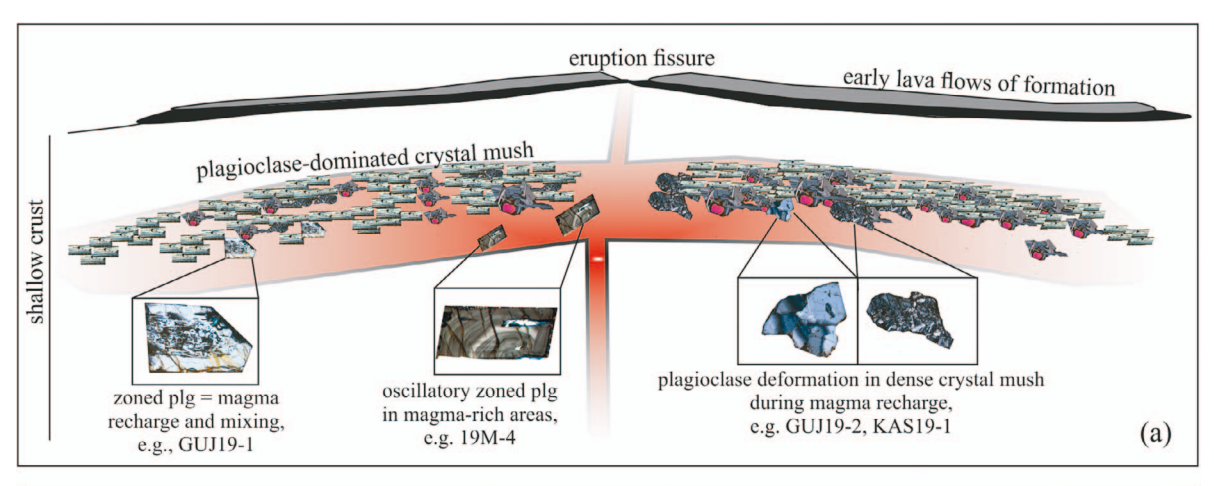


Fig. 20. Model of the degree of equilibration of Mg and Sr concentration (C) in plagioclase An₇₅ at 1000°C and 1100°C as a function of time. Equilibration $\% = 100 - 100 \times [(C - C_{Equilibrium}/C_{initial} - C_{equilibrium})].$ Curves show diffusion calculations for the equilibration of the concentration at the center of the plagioclase crystal using the 3D analytical solution for a parallelepiped (Crank, 1975) of a size $1 \times 0.25 \times 0.25$ mm. Diffusion coefficient of Mg from Van Orman et al. (2014) and that of Sr from Giletti & Casserly (1994).

environment such as expected in a crystal mush. Chemical data on plagioclase megacrysts, Rhyolite-MELTS modeling, pressuretemperature estimates on clinopyroxene and olivine, and literature data for GPBs from other LIPs (e.g. Krans et al., 2018; Moore et al., 2018) suggest that the plagioclase formed in the shallow crust from largely degassed, evolved basaltic magmas. In general, c. 1-cm-large plagioclase crystals as those investigated here would require several centuries to grow from a basaltic magma (Higgins & Chandrasekharam, 2007). However, shallow pressure conditions, volatile degassing, and significant undercooling may significantly enhance plagioclase crystallization rates (McCarthy et al., 2020). Such conditions are consistent with a shallow-depth crystal mush, which was occasionally flushed by hot, Fe-rich basaltic magma.

Considering the multiple lines of evidence for chemical zoning and disequilibrium between the plagioclase and matrix compositions, particularly for Sr isotopic compositions, it seems likely that plagioclase crystals from some samples were in contact with and crystallized from chemically distinct basaltic melts. In a crystal-mush scenario, we can envision continuous growth of the plagioclase over decades or centuries and several pulses of magmas flushing through the crystal mush. In other cases, plagioclase crystals show a much more homogeneous, unzoned composition pointing to a m0agmatic system with relatively constant composition. It should also be noted that single GPBs sometimes show significantly heterogeneous compositions, as highlighted for example by Thalghat (Borges et al., 2014 and this study) and by Tunnel-5 GPB samples (Beane et al., 1986; Basu et al., 2020a; this

Assuming that plagioclase megacrysts formed primarily in crystal mushes, the question arises as to how these highly viscous systems were remobilized during Deccan eruptions. The disruption of the crystal mush can occur by arrival of magmas rising from the deep crust and these magmas would be quite dense if they were as Fe-rich as the matrix of the samples analyzed herein. In such Fe-rich magmas, the buoyancy of plagioclase would be significant (>0.1 g/cm³; Fig. 18) enough to contribute to an effective fluxing of the crystal mush and uptake of large



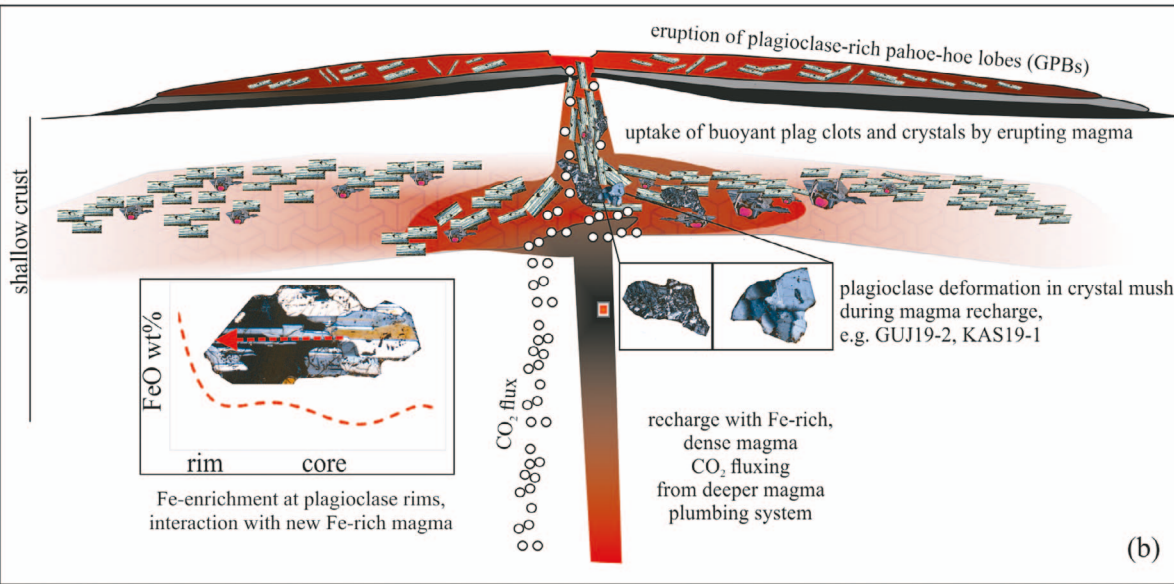


Fig. 21. Schematic representation of the proposed scenario for (a) the formation of plagioclase-rich crystal mushes in the shallow crust and (b) their eruption due to arrival of new Fe-rich magma rising from the deeper crust. In (a), the plagioclase-dominated crystal mush forms from a homogeneous melt (as shown by, e.e.g., samples GUJ19-4 or NAS19-6) or from a hybrid magma (as shown by the zoned plagioclase crystal from, e.g. GUJ19-1). Oscillatory zoning may develop in magma-rich regions. Deformation of plagioclase crystals by dislocation creep can occur in the crystal mush, when this mush is fluxed by rapidly rising magma (Spiess et al., 2017). (b) Shows the arrival of Fe-rich magma, which is suggested by the Fe-rich plagioclase rims. Further plagioclase deformation may occur in this phase, shortly prior to the eruption. Erupted GPB flows are highly heterogeneous as they may be constituted by magmas with different composition (i.e. the magma residing within the crystal mush and the magma rising from the deeper crust), as well as by variable amounts of plagioclase megacrysts from the pre-existing crystal mush or plagioclase phenocrysts. Furthermore, mafic minerals may be part of the crystal mush (e.g. clinopyroxene and olivine inclusions in plagioclase megacrysts) or phenocrysts crystallized from the rising magma. Possible fluxing by CO2 is shown in (b) and may enhance flushing of the magma plumbing system and eruption of GPB flows.

plagioclase crystals and aggregates in a rapidly rising magma plume (Bergantz et al., 2015). The heterogenous distribution of extremely coarsely crystalline zones within GPB suggests that the rheological threshold for eruptibility (e.g. Marsh, 1981) was lowered by the flux of Fe-rich mobilizing melts. Evidence for a late arrival of Fe-rich melts comes from matrix and plagioclase rim compositions, which are significantly enriched in Fe compared with the plagioclase cores, even considering a major element control on the Fe partition coefficient (Bindeman et al., 1998). The matrix samples are among the most Fe-rich samples of the Deccan and are in (or close to) equilibrium with plagioclase rims. The late magma in equilibrium with plagioclase rims was most likely an evolved basalt with relatively high Fe and Na/Ca (and high K for a few samples, e.g., MAL19-6), but it generally was slightly different from magma in equilibrium with plagioclase cores, for example in terms of Sr isotopic composition.

Such Fe-rich basaltic magmas probably differentiate from common Deccan basalts. Considering the Rhyolite-MELTS modeling starting from a Kalsubai MgO-rich basalt (e.g. SAM011, BOR036, MgO c. 8 and 12 wt%, respectively; Beane et al., 1986), FeOt enrichment up to 17 wt% can be reached at low pressure (0.1 GPa) in particular for dry conditions (Fig. 4a). Even higher FeOt (up to 20 wt%, for c. 4 wt% MgO) can be attained at 0.5 GPa, dry and unbuffered fO2 conditions (Rhyolite-MELTS modeling). Therefore, the most likely interpretation for the late Fe-rich melt is that it derived from mid- or deep-crustal depths and was essentially anhydrous. However, such melt would have a high density (c. 2.9 at 0.5 GPa) and thus a low buoyancy relative to the middleshallow crust, i.e. it would normally not rise up to the shallow crust, despite its low viscosity (c. 2.0 poise). Such high-density magma would also encounter difficulties in crossing the lowdensity, plagioclase-rich shallow-crust crystal mush. A possible scenario, which could explain the mobilization of the Fe-rich melt and its ascent through the plagioclase-rich mush in the shallow crust would be a fluxing of the plumbing system by volatiles, CO₂ in particular, rising from the deep plumbing system. Notably, recent melt inclusion analyses have shown that at least some Deccan basalts are quite rich in CO₂ (Hernandez Nava et al., 2021). Moreover, several of the samples analyzed here yield high Nb, up to 50% higher than all other previously analyzed Deccan basalts at similar MgO (Fig. 4f). Hernandez Nava et al. (2021) and Boscaini et al. (2022) use Nb as a proxy for CO2 contents in basalts with MgO >7 wt%. Even considering that the studied samples are quite evolved and that the CO2/Nb ratios may be partially modified during fractional crystallization, it may be suggested that the studied samples were derived from Nb and thus CO2-rich parental

It is noteworthy that GPB flows tend to occur at the transition between successive basalt formations of the WG lava pile. A similar situation is described for GPBs from the Ethiopian LIP, which erupted after a period of volcanic rest (Krans et al., 2018). Therefore, we may speculate that volatile fluxes were enhanced by arrival of new magma in the plumbing system, during transition from the waning extrusion of one basalt formation to the inception of extrusion of the next one. In this scenario, CO2 exsolved from the deep plumbing system, possibly at depths in excess of 15-20 km (Black & Manga, 2017; Caricchi et al., 2018; Capriolo et al., 2020; Black et al., 2021) could have significantly decreased the water fugacity of the system and promoted plagioclase crystallization (e.g. Caricchi et al., 2018). Incorporation of low-density plagioclase from the crystal mush significantly increased the buoyancy and eruptibility of magmas of the upper part of the magmatic plumbing system (Cashman et al., 2017).

CONCLUSIONS AND GENERAL IMPLICATIONS ON DECCAN MAGMA **PLUMBING SYSTEMS**

Most of the samples show some evidence for textural and/or chemical disequilibrium. The chemical zoning of plagioclase crystals indicates residence times, which range from a few years to a few centuries (as also found by Borges et al., 2014). The presence of deformed plagioclase crystals suggests that their megacrysts formed in crystal mushes in a shallow magmatic system and dislocation creep could have occurred when the crystal mush was fluxed by new magma intrusions. The presence of shallow crystal mushes also suggests that the magma plumbing system of at least part of the Deccan, and thus of LIPs in general, may not be fundamentally different from that of subduction-related and of some ocean island magmatic systems (Neave et al., 2017; Sparks et al., 2019; Black et al., 2021). Our data on plagioclase megacrysts shed light only on the shallowest differentiation of Deccan magmas, and the general picture that emerges is that of a dynamic, rapidly changing magmatic plumbing system, with a complex evolution in a transcrustal system. Fluxing of CO₂ fluids from the deep to the shallow parts of the magmatic plumbing system could have played a major role in decreasing the water content of the shallow magmas, promoting crystallization of plagioclase and the creation of crystal-rich mushes. The interaction of evolved but Fe-rich magmas with the plagioclase mushes allowed to reach density and viscosity values that facilitated the eruption of GPB. This proposition is consistent with recent interpretation of Deccan magmatism as resulting from a complex network of magma chambers (Mittal et al., 2021), rather than from a simple large

magma chamber (Ernst et al., 2019) with a homogenous magma composition.

Funding

We acknowledge financial support from PRIN (20178LPCP to A.M.), NSF grants 1736737 and 1615203, the Esper S. Larsen Fund of the University of California at Berkeley, and the Ann and Gordon Getty Foundation (to P.R.R.).

Acknowledgments

Andrea Risplendente (Università di Milano) and Davide Gabrielli (Università di Padova) provided help with EMP analyses. Steve Self, Courtney Sprain, Loyc Vanderkluysen, Tushar Mittal, Mark Richards and Vivek Kale are thanked for assistance with field work and fruitful discussions. Dhananjay Mohabey, Bandana Samant and Anup Dhobale provided samples KH-275 and GNG-498. Seth Burgess and Micheal A. Clynne (USGS, Menlo Park) are thanked for detailed reviews of the manuscript. Reviews by Ciro Cucciniello, Tushar Mittal and an anonymous reviewer as well as editorial handling by Barbara John were very constructive and significantly helped us to clarify several aspects of this study. Any use of trade, firm, or product names is for descriptive purposes only and does not imply endorsement by the U.S. Government.

References

Aigner-Torres, M., Blundy, J., Ulmer, P. & Pettke, T. (2007). Laser ablation ICPMS study of trace element partitioning between plagioclase and basaltic melts: an experimental approach. Contributions to Mineralogy and Petrology 153, 647-667. https://doi.org/10.1007/ s00410-006-0168-2.

Alexander, P. O. & Purohit, M. K. (2019). Giant Plagioclase Basalt from the Deccan Volcanic Province (DVP), Sagar District, Madhya Pradesh, India: first report and implications. Journal of the Geological Society of India 94, 139-141. https://doi.org/10.1007/ s12594-019-1282-x.

Bacon, C. & Hirschmann, M. (1988). Mg/Mn partitioning as a test for equilibrium between coexisting Fe-Ti oxides. American Mineralogist 73, 57-61.

Basu, A. R., Saha-Yannopoulos, A. & Chakrabarty, P. (2020a). A precise geochemical volcano-stratigraphy of the Deccan Traps. Lithos 376-377, 1-25. https://doi.org/10.1016/j.lithos.2020.105754.

Basu, A. R., Renne, P. R., Dasgupta, D. K., Teichmann, F. & Poreda, R. J. (1993). Early and late alkali igneous pulses and a high-3He plume origin for the Deccan flood basalts. Science 261, 902-906. https:// doi.org/10.1126/science.261.5123.902.

Basu, A. R., Chakraborty, P., Szymanowski, D., Ibanez-Mejia, M., Schoene, B., Ghosh, N. & Georg, R. B. (2020b). Widespread silicic and alkaline magmatism synchronous with the Deccan Traps flood basalts, India. Earth and Planetary Science Letters 552, 116616. https://doi.org/10.1016/j.epsl.2020.116616.

Beane, J., Turner, C., Hooper, P., Subbarao, K. & Walsh, J. (1986). Stratigraphy, composition and form of the Deccan basalts, Western Ghats, India. Bulletin of Volcanology 48(1), 61-83. https://doi. org/10.1007/BF01073513.

Bédard, J. H. (2006). Trace element partitioning in plagioclase feldspar. Geochimica et Cosmochimica Acta 70, 3717–3742. https:// doi.org/10.1016/j.gca.2006.05.003.

Béguelin, P., Chiaradia, M., Beate, B. & Spikings, R. (2015). The Yanaurcu volcano (Western Cordillera, Ecuador): a field, petrographic,

- geochemical, isotopic and geochronological study. Lithos 218-219, 37-53. https://doi.org/10.1016/j.lithos.2015.01.014.
- Bergantz, G. W., Schleicher, J. M. & Burgisser, A. (2015). Open-system dynamics and mixing in magma mushes. Nature Geoscience 8,
- Bindeman, I. N., Davis, A. M. & Drake, M. J. (1998). Ion microprobe study of plagioclase-basalt partition experiments at natural concentration levels of trace elements. Geochimica et Cosmochimica Acta 62, 1175-1193. https://doi.org/10.1016/S0016-7037 (98)00047-7.
- Black, B. A. & Manga, M. (2017). Volatiles and the tempo of flood basalt magmatism. Earth and Planetary Science Letters 458, 130-140. https://doi.org/10.1016/j.epsl.2016.09.035.
- Black, B. A., Karlstrom, L. & Mather, T. A. (2021). The life cycle of large igneous provinces. Nature Reviews Earth and Environment 2, 840-857. https://doi.org/10.1038/s43017-021-00221-4.
- Bond, D. P. G. & Grasby, S. E. (2017). On the causes of mass extinctions. Palaeogeography, Palaeoclimatology and Palaeoecology 478, 3-29. https://doi.org/10.1016/j.palaeo.2016.11.005.
- Borges, M. R., Sen, Gautam, Hart, Garret, L., Wolff, J. A. & Chandrasekharam, D. (2014). Plagioclase as recorder of magma chamber processes in the Deccan Traps: Sr isotope zoning and implications for Deccan eruptive event. Journal of Asian Earth Sciences 84, 95-101. https://doi.org/10.1016/j.jseaes.2013.10.034.
- Boscaini, A., Callegaro, S., Sun, Y. & Marzoli, A. (2022). Late Permian to late Triassic large igneous provinces: timing, eruptive style and paleoenvironmental perturbations. Frontiers in Earth Science 10, 1-8. https://doi.org/10.3389/feart.2022.887632.
- Callegaro, S., Baker, D. R., De Min, A., Marzoli, A., Geraki, K., Bertrand, H., Viti, C. & Nestola. (2014). Microanalyses link sulfur from large igneous provinces and Mesozoic mass extinctions. Geology 42, 895-898. https://doi.org/10.1130/G35983.1.
- Capriolo, M., Marzoli, A., Callegaro, S., Dal Corso, J., Newton, R. J., Mills, B. J. W., Wignall, P. B., Bartoli, O., Baker, D. R., Youbi, N., Remusat, L., Spiess, R. & Szabó, C. (2020). Deep CO2 in the end-Triassic Central Atlantic Magmatic Province. Nature Communications 11, 1670. https://doi.org/10.1038/s41467-020-1532.
- Caricchi, L., Sheldrake, T. E. & Blundy, J. (2018). Modulation of magmatic processes by CO₂ flushing. Earth and Planetary Science Letters 491, 160-171. https://doi.org/10.1016/j.epsl.2018.03.042.
- Cashman, K. V., Sparks, R. S. & Blundy, J. D. (2017). Vertically extensive and unstable magmatic systems: a unified view of igneous processes. https://doi.org/10.1126/science.aag3055.
- Chenet, A.-L., Fluteau, F., Courtillot, V., Gerard, M. & Subbarao, K. (2008). Determination of rapid Deccan eruptions across the Cretaceous-Tertiary boundary using paleomagnetic secular variation: results from a 1200 m thick section in the Mahabaleshwar escarpment. Journal of Geophysical Research: Solid Earth **113**(B4), 1–27.
- Chiaradia, M., Műntener, O. & Beate, B. (2011). Enriched basaltic andesites from mid-crustal fractional crystallization, recharge, and assimilation (Pilavo volcano, western Cordillera of Ecuador). Journal of Petrology 52, 1107-1141. https://doi.org/10.1093/ petrology/egr020.
- Clapham, M. E. & Renne, P. R. (2019). Flood basalts and mass extinctions. Annual Review of Earth and Planetary Sciences 47, 275-303. https://doi.org/10.1146/annurev-earth-053018-060136.
- Costa, F. (2021). Clocks in magmatic rocks. Annual Review of Earth and Planetary Sciences 49, 231-252. https://doi.org/10.1146/annurevearth-080320-060708.
- Costa, F., Chakraborty, S. & Dohmen, R. (2003). Diffusion coupling between trace and major elements and a model for calculation of magma residence times using plagioclase. Geochimica et

- Cosmochimica Acta 67, 2189–2200. https://doi.org/10.1016/ S0016-7037(02)01345-5.
- Cox, K. (1980). A model for flood basalt vulcanism. Journal of Petrology 21, 629-650. https://doi.org/10.1093/petrology/21.4.629.
- Cox, K. & Hawkesworth, C. (1985). Geochemical stratigraphy of the Deccan Traps at Mahabaleshwar, Western Ghats, India, with implications for open system magmatic processes. Journal of Petrology 26, 355–377. https://doi.org/10.1093/petrology/26.2.355.
- Crank, J. (1975) The Mathematics of Diffusion. Oxford: Oxford Science Publications.
- Cucciniello, C., Demonterova, E. I., Sheth, H., Pande, K. & Vijayan, A. (2015). 40 Ar/39 Ar geochronology and geochemistry of the Central Saurashtra mafic dyke swarm: insights into magmatic evolution, magma transport, and dyke-flow relationships in the northwestern Deccan Traps. Bulletin of Volcanology 77(45), 1096. https://doi. org/10.1007/s00445-015-0932-0.
- Cucciniello, C., Choudhary, A. K., Pande, K. & Sheth, H. (2019). Mineralogy, geochemistry and 40 Ar/39 Ar geochronology of the Barda and Alech complexes, Saurashtra, northwestern Deccan Traps: early silicic magmas derived by flood basalt fractionation. Geological Magazine 156, 1668-1690. https://doi. org/10.1017/S0016756818000924.
- Cucciniello, C., Sheth, H., Duraiswami, R. A., Wegner, W., Koeberl, C., Das, T. & Ghule, V. (2020). The Southeastern Saurashtra dyke swarm, Deccan Traps: magmatic evolution of a tholeiitic basaltbasaltic andesite-andesite-rhyolite suite. Lithos 376-377, 105759. https://doi.org/10.1016/j.lithos.2020.105759.
- Dohmen, R. & Milke, R. (2010). Diffusion in polycrystalline materials: grain boundaries, mathematical models, and experimental data. Reviews in Mineralogy and Geochemistry 72, 921-970. https://doi. org/10.2138/rmg.2010.72.21.
- Dygert, N., Draper, D. S., Rapp, J. F., Lapen, T. J., Fagan, A. L. & Neal, C. R. (2020). Experimental determinations of trace element partitioning between plagioclase, pigeonite, olivine, and lunar basaltic melts and an fO2 dependent model for plagioclase-melt Eu partitioning. Geochimica et Cosmochimica Acta 279, 258-280. https://doi.org/10.1016/j.gca.2020.03.037.
- Eddy, M. P., Schoene, B., Samperton, K. M., Keller, G., Adatte, T. & Khadri, S. F. (2020). U-Pb zircon age constraints on the earliest eruptions of the Deccan Large Igneous Province, Malwa Plateau, India. Earth and Planetary Science Letters 540, 116249. https://doi. org/10.1016/j.epsl.2020.116249.
- Edmonds, M. (2008). New geochemical insights into volcanic degassing. Philosophical Transactions of the Royal Society A 366, 4559-4579. https://doi.org/10.1098/rsta.2008.0185.
- Ernst, R. E. & Youbi, N. (2017). How Large Igneous Provinces affect global climate, sometimes cause mass extinctions, and represent natural markers in the geological record. Palaeogeography Palaeoclimatology Palaeoecology 478, 30–52.
- Ernst, R. E., Liikane, D. A., Jowitt, S. M., Buchan, K. & Blanchard, J. (2019). A new plumbing system framework for mantle plume-related continental Large Igneous Provinces and their mafic-ultramafic intrusions. Journal of Volcanology and Geothermal Research 384, 75-84. https://doi.org/10.1016/j. jvolgeores.2019.07.007.
- Feig, S. T., Koepke, J. & Snow, J. E. (2006). Effect of water on tholeiitic basalt phase equilibria: an experimental study under oxidizing conditions. Contributions to Mineralogy and Petrology 152, 611-638. https://doi.org/10.1007/s00410-006-0123-2.
- Gangpèhadayay, A., Sen, G. & Keshav, S. (2003). Experimental crystallization of Deccan basalts at low pressure: effect of contamination on phase equilibrium. Indian Journal of Geology **75**, 54.

- Giletti, B. J. & Casserly, J. E. D. (1994). Strontium diffusion kinetics in plagioclase feldspars. Geochimica et Cosmochimica Acta 58, 3785-3793. https://doi.org/10.1016/0016-7037(94)90363-8.
- Giordano, G. & Caricchi, L. (2022). Determining the state of activity of transcrustal magmatic systems and their volcanoes. Annual Review of Earth and Planetary Sciences 50, 231-259. https://doi. org/10.1146/annurev-earth-032320-084733.
- Glišović, P. & Forte, A. M. (2017). On the deep-mantle origin of the Deccan Traps. Science 355, 613-616. https://doi.org/10.1126/ science.aah4390.
- Gualda, G. A. R., Ghiorso, M. S., Lemons, R. V. & Carley, T. L. (2012). Rhyolite-MELTS: a modified calibration of MELTS optimized for silica-rich, fluid-bearing magmatic systems. Journal of Petrology 53, 875-890. https://doi.org/10.1093/petrology/egr080.
- Haase, K., Regelous, M., Schöbel, S., Gunther, T. & de Wall, H. (2019). Variation of melting processes and magma sources of the early Deccan flood basalts, Malwa plateau, India. Earth and Planetary Science Letters 524, 115711. https://doi.org/10.1016/ j.epsl.2019.115711.
- Hagen-Peter, G., Tegner, C. & Lesher, C. E. (2019). Strontium isotope systematics for plagioclase of the Skaergaard intrusion (East Greenland): a window to crustal assimilation, differentiation, and magma dynamics. Geology 47, 313-316. https://doi.org/10.1130/ G45639.1.
- Hernandez Nava, A., Black, B. A., Gibson, S. A., Bodnar, R. J., Renne, P. R. & Vanderkluysen, L. (2021). Reconciling early Deccan Traps CO2 outgassing and pre-KPB global climate. Proceedings of the National Academy of Sciences 117, 118, 1-9. https://doi.org/10.1073/ pnas.2007797118.
- Higgins, M. D. & Chandrasekharam, D. (2007). Nature of sub-volcanic magma chambers, Deccan Province, India: evidence from quantitative textural analysis of plagioclase megacrysts in the Giant Plagioclase Basalts. Journal of Petrology 48, 885-900. https://doi. org/10.1093/petrology/egm005.
- Holness, M. B., Cawthorn, R. G. & Roberts, J. (2017). The thickness of the crystal mush on the floor of the Bushveld magma chamber. Contributions to Mineralogy and Petrology 172, 102. https://doi. org/10.1007/s00410-017-1423-4.
- Holness, M. B., Humphreys, M. C. S., Namur, O., Andersen, J. C. Ø., Tegner, C. & Nielsen, T. F. D. (2022). Crystal mush growth and collapse on a steep wall: the marginal border series of the Skaergaard Intrusion, East Greenland. Journal of Petrology 63, egab100. https:// doi.org/10.1093/petrology/egab100.
- Hooper, P. R., Subbarao, K. V. & Beane, J. E. (1988). The giant plagioclase basalts (GPB) of the Western Ghats, Deccan Traps. Geological Society of India Memoir 10, 135-144.
- Jay, A. E. & Widdowson, M. (2008). Stratigraphy, structure and volcanology of the SE-Deccan continental flood basalt province: implications for eruptive extent and volumes. Journal of the Geological Society 165, 177–188. https://doi. org/10.1144/0016-76492006-062.
- Johnson, D., Hooper, P. & Conrey, R. (1999). XRF method XRF analysis of rocks and minerals for major and trace elements on a single low dilution Li-Tetraborate fused bead. Advances in X-ray Analyses 41,843-867.
- Kale, V. S., Dole, G., Shandilya, P. & Pande, K. (2020). Stratigraphy and correlations in Deccan Volcanic Province, India: quo vadis? Geological Society of America Bulletin 132, 588-607. https://doi. org/10.1130/B35018.1.
- Karlstrom, L. & Richards, M. A. (2011). On the evolution of large ultramafic magma chambers and timescales for flood basalt eruptions. Journal of Geophysical Research: Solid Earth 116(B8), 1-13. https://doi.org/10.1029/2010JB008159.

- Karmarkar, B. M., Kulkarni, S. R., Marethe, S. S., Sowane, P. V. & Peshwa, V. V. (1971). Giant phenocryst basalts in the Deccan Trap. Bulletin of Volcanology 35, 965-974. https://doi.org/10.1007/BF02596858.
- Knaack, C., Cornelius, S. & Hooper, P. (1994) Trace element analyses of rocks and minerals by ICPMS. Washington State University, Open-File Report.
- Knight, K. B., Nomade, S., Renne, P. R., Marzoli, A., Bertrand, H. & Youbi, N. (2004). The Central Atlantic Magmatic Province at the Triassic–Jurassic boundary: Paleomagnetic and 40 Ar/39 Ar evidence from Morocco for brief, episodic volcanism. Earth and Planetary Science Letters 228, 143-160. https://doi.org/10.1016/j. epsl.2004.09.022.
- Kohut, E. J. & Nielsen, R. L. (2003). Low-pressure phase equilibria of anhydrous anorthite bearing mafic magmas. Geochemistry, Geophysics, Geosystems 4, 1057. https://doi.org/10.1029/2002
- Krans, S. R., Rooney, T. O., Kappelman, G., Yirgu, J., & Ayalew, D. (2018). From initiation to termination: a petrostratigraphic tour of the Ethiopian low-Ti Flood Basalt Province. Contributions to Mineralogy and Petrology 173, 37. https://doi.org/10.1007/s00410-018-1460-7.
- Krättli, G. & Schmidt, M. (2021). Experimental settling, floatation and compaction of plagioclase in basaltic melt and a revision of melt density. Contributions to Mineralogy and Petrology 176, 30. https:// doi.org/10.1007/s00410-021-01785-6.
- Krishnamurthy, P. (2020). The Deccan Volcanic Province (DVP), India: a review. Journal of the Geological Society of India 96, 111–147. https:// doi.org/10.1007/s12594-020-1521-1.
- Laubier, M., Grove, T. L. & Langmuir, C. H. (2014). Trace element mineral/melt partitioning for basaltic and basaltic andesitic melts: an experimental and laser ICP-MS study with application to the oxidation state of mantle source regions. Earth and Planetary Science Letters 392, 265-278. https://doi.org/10.1016/ j.epsl.2014.01.053.
- Le Bas, M. J., Le Maitre, R. W., Streckeisen, A. & Zanettin, B. (1986). A chemical classification of volcanic rocks based on the total alkali-silica diagram. Journal of Petrology 27, 745-750. https://doi. org/10.1093/petrology/27.3.745.
- Lundgaard, K. L. & Tegner, C. (2004). Partitioning of ferric and ferrous iron between plagioclase and silicate melt. Contributions to Mineralogy and Petrology 147, 470–483.
- Mahoney, J. J. (1988). Deccan Traps. In Macdougall, J. D. (ed) Continental Flood Basalts. Dordrecht: Kluwer Academic, pp. 151-194, https:// doi.org/10.1007/978-94-015-7805-9_5.
- Mahoney, J. J., Sheth, H., Chandrasekharam, D. & Peng, Z. (2000). Geochemistry of flood basalts of the Toranmal section, northern Deccan Traps, India: implications for regional Deccan stratigraphy. Journal of Petrology 41, 1099-1120. https://doi.org/10.1093/ petrology/41.7.1099.
- Marsh, B. D. (1981). On the crystallinity, probability of occurrence, and rheology of lava and magma. Contributions to Mineralogy and Petrology 78, 85-98. https://doi.org/10.1007/BF00371146.
- Marsh, B. D. (2004). A magmatic mush column Rosetta Stone: the McMurdo Dry Valleys of Antarctica. Eos, Transactions, American Geophysical Union 85, 497-508. https://doi.org/10.1029/2004
- Marzoli, A., Bertrand, H., Youbi, N., Callegaro, S., Merle, R., Reisberg, L., Chiaradia, M., Brownlee, S. I., Jourdan, F., Zanetti, A., Davies, J. H. F. L., Cuppone, T., Mahmoudi, A., Medina, F., Renne, P. R., Bellieni, G., Crivellari, S., El Hachimi, H., Bensalah, M. K., Meyzen, C. M. & Tegner, C. (2019). The Central Atlantic Magmatic Province (CAMP) in Morocco. Journal of Petrology 60, 945-996. https://doi. org/10.1093/petrology/egz021.

- McCarthy, A., Chelle-Michou, C., Blundy, J. D., Vonlanthen, P., Meibom, A., & Escrig, S. (2020). Taking the pulse of volcanic eruptions using plagioclase glomerocrysts. Earth and Planetary Science Letters, 552, 116596, https://doi.org/10.1016/j.epsl.2020.116596.
- McDonough, W. F. & Sun, S. S. (1995). The composition of the Earth. Chemical Geology 120, 223-253. https://doi.org/10.1016/0009-2541 (94)00140-4.
- Melluso, L., & Sethna, S. (2011). Mineral compositions in the Deccan igneous rocks of India: an overview. In: Jyotisankar, R., Sen, G., & Ghosh, B (eds) Topics in Igneous Petrology: a Tribute to Prof. Mihir K. Bose, 135–159. Heidelberg: Springer, https://dx.doi. org/10.1007/978-90-481-9600-5_7.
- Melluso, L., Sethna, S. & Srivastava, R. K. (2021). First occurrence of melilite, potassic richterite and tetraferriphlogopite in deccan trap-related alkaline rocks, and its petrogenetic significance: the Rajpuri ijolite-nephelinite intrusion, Murud, Mumbai area, India. Neues Jahrbuch für Mineralogiesche Abhandlungen 197, 49-64. https://doi.org/10.1127/njma/2020/0236.
- Melluso, L., Beccaluva, L., Brotzu, P., Gregnanin, A., Gupta, A., Morbidelli, L. & Traversa, G. (1995). Constraints on the mantle sources of the Deccan Traps from the petrology and geochemistry of the basalts of Gujarat state (western India). Journal of Petrology 36, 1393-1432. https://doi.org/10.1093/petrology/36.5.1393.
- Melluso, L., Mahoney, J. J. & Dallai, L. (2006). Mantle sources and crustal input as recorded in high-mg Deccan Traps basalts of Gujarat (India). Lithos 89, 259-274. https://doi.org/10.1016/j. lithos.2005.12.007.
- Mittal, T., Richards, M. A. & Fendley, I. M. (2021). The magmatic architecture of continental flood basalts I: observations from the Deccan Traps. Journal of Geophysical Research: Solid Earth 126, e2021JB021808. https://doi.org/10.1029/2021JB021808
- Mittal, T., Sprain, C. S., Renne, P. R., & Richards, M. A. (2022). Deccan volcanism at K-Pg time. In Koeberl, C., Claeys, P., and Montanari, A. (eds), From the Guajira Desert to the Apennines, and from Mediterranean Microplates to the Mexican Killer Asteroid: Honoring the Career of Walter Alvarez: Geological Society of America Special Paper, 557, 471-49, https://doi.org/10.1130/2022.2557(22).
- Moore, N. E., Grunder, A. L. & Bohrson, W. A. (2018). The threestage petrochemical evolution of the Steens basalt (Southeast Oregon, USA) compared to large igneous provinces and layered mafic intrusions. Geosphere 14, 2505-2532. https://doi. org/10.1130/GES01665.1.
- Neave, D. & Putirka, K. (2017). A new clinopyroxene-liquid barometer, and implications for magma storage pressures under Icelandic rift zones. American Mineralogist 102, 777-794. https://doi. org/10.2138/am-2017-5968.
- Neave, D. A., Buisman, I. & Maclennan, J. (2017). Continuous mush disaggregation during the long-lasting Laki fissure eruption, Iceland. American Mineralogist 102, 2007–2021. https://doi. org/10.2138/am-2017-6015CCBY.
- Papike, J. J., Cameron, K. L. & Baldwin, K. (1974). Amphiboles and pyroxenes: characterization of other than quadrilateral components and estimates of ferric iron from microprobe data. Geological Society of America, Abstracts with Programs 6, 1053-1054.
- Parisio, L., Jourdan, F., Marzoli, A., Melluso, L., Sethna, S. F. & Bellieni, G. (2016). 40 Ar/39 Ar ages of alkaline and tholeitic rocks from the northern Deccan Traps: implications for magmatic processes and the K-Pg boundary. Journal of the Geological Society 173, 679-688. https://doi.org/10.1144/jgs2015-133.
- Passchier, C. & Trouw, R. A. J. (2005). Microtectonics. Springer, Berlin, Heidelberg, p. XVI, 366. https://doi.org/10.1007/3-540-29359-0.
- Peng, Z. X. & Mahoney, J. J. (1995). Drillhole lavas from the northwestern Deccan Traps, and the evolution of Reunion hotspot

- mantle. Earth and Planetary Science Letters 134, 169–185. https://doi. org/10.1016/0012-821X(95)00110-X.
- Peng, Z. X., Mahoney, J. J., Hooper, P., Harris, C. & Beane, J. (1994). A role for lower continental crust in flood basalt genesis? Isotopic and incompatible element study of the lower six formations of the western Deccan Traps. Geochimica et Cosmochimica Acta 58, 267-288. https://doi.org/10.1016/0016-7037(94)90464-2.
- Peng, Z. X., Mahoney, J. J., Hooper, P. R., Macdougall, J. D. & Krishnamurthy, P. (1998). Basalts of the northeastern Deccan Traps, India: isotopic and elemental geochemistry and relation to southwestern Deccan stratigraphy. Journal of Geophysical Research 103, 29843-29865. https://doi.org/10.1029/98JB01514
- Peng, Z. X., Mahoney, J. J., Vanderkluysen, L. & Hooper, P. R. (2014). Sr, Nd and Pb iso-topic and chemical compositions of central Deccan Traps lavas and relation to southwestern Deccan stratigraphy. Journal of Asian Earth Sciences 84, 83-94. https://doi.org/10.1016/ i.iseaes.2013.10.025.
- Putirka, K. (2008). Thermometers and barometers for volcanic systems. In: Putirka, K. & Tepley, F. J. (eds.), Minerals, Inclusions and Volcanic Processes. Mineralogical Society of America, Reviews in Mineralogy and Geochemistry 69, 61-120, https://doi. org/10.1515/9781501508486-004.
- Renne, P. R., Sprain, C. J., Richards, M. A., Self, S., Vanderkluysen, L. & Pande, K. (2015). State shift in Deccan volcanism at the Cretaceous-Paleogene boundary, possibly induced by impact. Science 350, 76-78. https://doi.org/10.1126/science.aac7549.
- Roeder, P. L. & Emslie, R. F. (1970). Olivine-liquid equilibrium. Contributions to Mineralogy and Petrology 29, 275-289. https://doi. org/10.1007/BF00371276.
- Ruprecht, P. & Wörner, G. (2007). Variable regimes in magma systems documented in plagioclase zoning patterns: El Misti stratovolcano and Andahua monogenetic cones. Journal of Volcanology and Geothermal Research 165, 142-162. https://doi.org/10.1016/j. jvolgeores.2007.06.002.
- Rybacki, E., Wirth, R. & Dresen, G. (2008). High-strain creep of feldspar rocks: implications for cavitation and ductile failure in the lower crust. Geophysical Research Letters 35, L04304. https://doi. org/10.1029/2007GL032478.
- Rybacki, E., Wirth, R. & Dresen, G. (2010). Superplasticity and ductile fracture of synthetic feldspar deformed to large strain. Journal of Geophysical Research 115, B08209. https://doi.org/10.1029/2009 JB007203.
- Sano, T., Fujii, T., Deshmukh, S., Fukuoka, T. & Aramaki, S. (2001). Differentiation processes of Deccan Trap basalts: contribution from geochemistry and experimental petrology. Journal of Petrology 42, 2175-2195. https://doi.org/10.1093/petrology/42.12.2175.
- Sauerzapf, U., Lattard, D., Burchard, M. & Engelmann, R. (2008). The Titanomagnetite-Ilmenite equilibrium: new experimental data and thermo-oxybarometric application to the crystallization of basic to intermediate rocks. Journal of Petrology 49, 1161-1185. https://doi.org/10.1093/petrology/egn021.
- Schöbel, S., de Wall, H., Ganerød, M., Pandit, M. K. & Rolf, C. (2014). Magnetostratigraphy and 40 Ar/39 Ar geochronology of the Malwa plateau region (Northern Deccan Traps), central western India: significance and correlation with the main Deccan large igneous province sequences. Journal of Asian Earth Sciences 89, 28-45. https://doi.org/10.1016/j.jseaes.2014.03.022.
- Schoene, B., Samperton, K. M., Eddy, M. P., Keller, G., Adatte, T., Bowring, S. A. & Gertsch, B. (2015). U-Pb geochronology of the Deccan Traps and relation to the end-Cretaceous mass extinction. Science 347, 182-184. https://doi.org/10.1126/science.aaa0118.
- Schoene, B., Eddy, M. P., Samperton, K. M., Keller, C. B., Keller, G., Adatte, T. & Khadri, S. F. (2019). U-Pb constraints on pulsed

- eruption of the Deccan Traps across the end-Cretaceous mass extinction. Science 363, 862-866. https://doi.org/10.1126/science. aau2422.
- Self, S., Blake, S., Sharma, K., Widdowson, M. & Sephton, S. (2008). Sulfur and chlorine in late Cretaceous Deccan magmas and eruptive gas release. Science 319, 1654-1657. https://doi.org/10.1126/ science.1152830.
- Self, S., Mittal, T. & Jay, A. E. (2021). Thickness characteristics of pāhoehoe lavas in the Deccan Province, Western Ghats, India, and in continental flood basalt provinces elsewhere. Frontiers in Earth Sciences 8, 1-22. https://doi.org/10.3389/feart.2020.630604.
- Self, S., Mittal, T., Dole, G. & Vanderkluysen, L. (2022). Toward understanding Deccan volcanism. Annual Review of Earth and Planetary Sciences 50, 477-506. https://doi.org/10.1146/annurevearth-012721-051416.
- Sen, G., Borges, M. & Marsh, B. D. (2006). A case for short duration of Deccan Trap eruption. Eos, Transactions, American Geophysical Union 87, 197. https://doi.org/10.1029/2006EO200001.
- Shandilya, P., Chatterjee, P., Pattabhirma, K., Bodas, M., Pande, K. & Kale, V. (2021). Rajgad GPB: a megaporphyritic cow beld, Western Deccan Volcanic Province, India. Journal of Earth Systems 129, art. 113. https://doi.org/10.1007/s12040-020-1375-3.
- Sheth, H. (2005). From Deccan to Rèunion: no trace of a mantle plume. Special Paper of the Geological Society of America 388, 477–501.
- Sheth, H. (2016). Giant plagioclase basalts: continental flood basaltinduced remobilization of anorthositic mushes in deep crustal sill complex. Geological Society of America Bulletin 128, 916-925.
- Sheth, H. C., Zellmer, G. F., Kshirsagar, P. V. & Cucciniello, C. (2013). Geochemistry of the Palitana flood basalt sequence and the eastern Saurashtra dykes, Deccan Traps: clues to petrogenesis, dyke-flow relationships, and regional lava stratigraphy. Bulletin of Volcanology 75, 1–23. https://doi.org/10.1007/s00445-013-0701-x.
- Sparks, R. S. J., Annen, C., Blundy, J. D., Cashman, K. V., Rust, A. C. & Jackson, M. D. (2019). Formation and dynamics of magma reservoirs. Philosophical Transactions of the Royal Society 377, 20180019. https://doi.org/10.1098/rsta.2018.0019.
- Spiess, R., Dibona, R., Rybacki, E., Wirth, R. & Dresen, G. (2012). Depressurized cavities within high-strain shear zones: their role in the segregation and flow of SiO2-rich melt in feldspardominated rocks. Journal of Petrology 53, 1767-1776. https://doi. org/10.1093/petrology/egs032.

- Spiess, R., Dibona, R., Faccenda, M., Mattioli, M. & Renzulli, A. (2017). Mylonitic gabbro nodules of Stromboli (southern of microstructural evidence high-temperature deformation of cumulates during the evolution of the magmatic crustal roots of an active volcano. Special Paper of the Geological Society of America 526, 89-105. https://doi.org/10.1130/2017.2526(05).
- Sprain, C. J., Renne, P. R., Vanderkluysen, L., Pande, K. & Self., S., & Mittal, T. (2019). The eruptive tempo of Deccan volcanism in relation to the Cretaceous-Paleogene boundary. Science 363, 866-870. https://doi.org/10.1126/science.aav1446.
- Sun, C., Graff, M. & Liang, Y. (2017). Trace element partitioning between plagioclase and silicate melt: the importance of temperature and plagioclase composition, with implications for terrestrial and lunar magmatism. Geochimica et Cosmochimica Acta 206, 273-295. https://doi.org/10.1016/j.gca.2017.03.003.
- Tepley, F. J., Lundstrom, C. C., McDonough, W. F. & Thompson, A. (2010). Trace element partitioning between high-An plagioclase and basaltic to basaltic andesite melt at 1 atmosphere pressure. Lithos 118, 82-94. https://doi.org/10.1016/j.lithos.2010.04.001.
- Van Orman, J. A., Cherniak, D. J. & Kita, N. T. (2014). Magnesium diffusion in plagioclase: dependence on composition, and implications for thermal resetting of the 26 Al/26 Mg early solar system chronometer. Earth and Planetary Science Letters 385, 79–88. https:// doi.org/10.1016/j.epsl.2013.10.026.
- Vanderkluysen, L., Mahoney, J. J., Hooper, P. R., Sheth, H. C. & Ray, R. (2011). The feeder system of the Deccan Traps (India): insights from dike geochemistry. Journal of Petrology 52, 315-343. https:// doi.org/10.1093/petrology/egq082.
- Wilson Mantilla, G. P., Renne, P. R., Samant, B., Mohabey, D. M., Dhopale, A., Tholt, A. J., Tobin, T. S., Widdowson, M., Anantharaman, S., Chandra Dassarma, D. & Wilson Mantilla, J. S. (2022). New mammals from the Naskal intertrappean site and the age of the type locality of India's first Cretaceous mammal. Palaeogeography, Palaeoclimatology, Palaeoecology 591, 1-28. https://doi.org/10.1016/ j.palaeo.2022.110857.
- Zellmer, G. F., Sparks, R. S. J., Hawkesworth, C. J. & Wiedenbeck, M. (2003). Magma emplacement and remobilization timescales beneath Montserrat: insights from Sr and Ba zonation in plagioclase phenocrysts. Journal of Petrology 44, 1413-1431. https://doi. org/10.1093/petrology/44.8.1413.